DESIGN OF ACTIVE SUSPENSION CONTROL BASED UPON USE OF TUBULAR LINEAR MOTOR AND QUARTER-CAR MODEL

A Thesis

by

JUSTIN AARON ALLEN

Submitted to the Office of Graduate Studies of
Texas A&M University
in partial fulfillment of the requirements for the degree of

MASTER OF SCIENCE

August 2008

Major Subject: Mechanical Engineering

DESIGN OF ACTIVE SUSPENSION CONTROL BASED UPON USE OF TUBULAR LINEAR MOTOR AND QUARTER-CAR MODEL

A Thesis

by

JUSTIN AARON ALLEN

Submitted to the Office of Graduate Studies of
Texas A&M University
in partial fulfillment of the requirements for the degree of

MASTER OF SCIENCE

Approved by:

Chair of Committee,	Won-jong Kim
Committee Members,	Shankar Bhattacharyya
	Darbha Swaroop
Head of Department,	Dennis L. O'Neal

August 2008

Major Subject: Mechanical Engineering

ABSTRACT

Design of Active Suspension Control Based upon Use of Tubular Linear Motor and Quarter-Car Model. (August 2008)
Justin Aaron Allen, B.S., Texas A&M University
Chair of Advisory Committee: Dr. Won-jong Kim

The design, fabrication, and testing of a quarter-car facility coupled with various control algorithms are presented in this thesis. An experimental linear tubular motor, capable of producing a 52-N force, provides control actuation to the model. Controllers consisting of two designs were implemented: a classical controller employing lead and lag networks and a state-space feedback design. Each design was extensively simulated to screen for receptiveness to actuation force limitations and robustness regarding the inexact tire modeling. The goal of each controller was to minimize the acceleration of the sprung mass in the presence of simulated road disturbances, modeled by both sinusoidal and step input excitation wheels.

Different reference velocity inputs were applied to the control scheme. Responses to a zero reference were juxtaposed to those that resulted from tracking a reference built off a model that incorporated inertial-frame damping attached to the sprung mass. The outcome of this comparison was that low-frequency disturbances were attenuated better when tracking a zero reference, but the reference relaxation introduced by the inertial-frame damping model allowed for better-attenuated high frequency signals. Employing an inertial-frame damping value of 250 N-s/m, the rejected frequency component of the system response synchronous with the disturbance input excitation of 40 rad/s bettered by 33% and 28% when feeding control force from the classical controller and state-space controller, respectively.

The experimental analysis conducted on the classical and state-space controllers produced sinusoidal disturbance rejection of at worst 50% within their respective bandwidths. At 25 rad/s, the classical controller was able to remove 80% of the base

component synchronous with the disturbance excitation frequency, while the state-space controller filtered out nearly 60%.

Analysis on the system's ability to reject step disturbances was greatly confounded with the destructive lateral loading transferred during the excitation process. As a result, subjection to excitation could only occur up to 25 rad/s. At the 20 rad/s response synchronous to the disturbance excitation, the classical and state-space controllers removed 85% and 70% of the disturbance, respectively. Sharp spikes in time-based amplitude were present due to the binding that ensued during testing.

For my mother, Debbie, whose persistence
and steadfast support fueled my drive to the end.

TABLE OF CONTENTS

Page

Page

Page

LIST OF FIGURES

Page

Page

Page

Page

LIST OF TABLES

Page

I. INTRODUCTION

Automobiles contribute to the majority of personal travel in many parts of the world. New and better technology seems to improve many aspects of its abilities. For example, the conversion of air/fuel metering from the carburetor has evolved to the much more reliable and precise computer-controlled fuel injection system. Updates are often employed to save energy resources, save lives, and increase vehicle performance. One budding area of interest is the integration of controllable elements with the automotive suspension components. Active suspension, as it is appropriately termed, allows the automobile to sustain several advantages in comparison to its passive counterpart. Better ride quality as well as increasing the road holding capability [1] are but a few benefits this implementation brings. Other additions are dynamic ride height adjustment to reduce drag and power recovery when traversing irregularities in the pavement [2].

A. Varieties of Automotive Suspensions

Automotive suspensions appear in many shapes and sizes, each with their own intent. Heavy duty equipment generally employs solid axle type with leaf-springs providing large loading capabilities with excellent resistance to lateral motion under heavy loads. These suspensions are incredibly stiff by design and generally provide extremely poor ride qualities. Therefore, supplemental suspensions such as cab isolation on semi-tractor trailer units, such as that presented in [3], and seat damping on smaller units are added for addressing operator comfort.

Passenger cars nowadays generally opt for a lower control arm coupled with a MacPherson strut assembly, which employs a compact design and good variability for different goals (i.e. performance or comfort).

This thesis follows the *IEEE* journal style.

The limitation using standard elements is that generally the suspension can only be designed for narrow range of performance. For example, cars tuned for increased handling are very stiff and do not provide a plush ride quality, while a luxury passenger car designed for minimal force transmission sacrifices high-speed stability to attain this effect. To obtain wider ranges of performance, active suspension techniques can offer capabilities that are adept at supplying these results.

Semi-active suspension is an alternative, utilizing active damping as the control mechanism. These systems are termed semi-active because they cannot supply a force, only control the dissipation of energy from the system. From [4], the most common types are dampers that employ a magneto-rheological viscous fluid or control the orifice passages using a solenoid valve.

Active Suspension implements force producing elements that require external energy whereas passive suspension utilizes only energy dissipation and storage components [5]. These force elements are most commonly comprised of hydraulic or electromechanical actuators, each posing unique challenges regarding their controllability. Due to the large inertias present in the fluid, valves, and pistons, hydraulic actuators are dynamically slower than electromechanical systems. Also, because dry friction is present in significant magnitudes [6], they tend to be very nonlinear. Similarly, nonlinearity arises due to the output force being a function of the magnet temperature in permanent-magnet motors; however, the nonlinearity is generally a large magnitude less than that of hydraulic systems.

B. Prior Art

In preparation for development of a testing facility that employs suitable electromechanical actuation with robust control, an extensive study to investigate controllers both applied to generic linear motors and directed towards active suspension control.

1. Linear Motor Control

Gu and Nam [7] presented a control scheme for linear motors operating outside optimal ranges. This vector control is aimed at adapting to the change in the electrical dynamics when coils on the mover are not in the presence of a magnetic field, with their control supplying the proper current to a motor by modulating voltage output. Kim and Murphy [8] simplified this by utilizing internal control loops in pulse-width modulated (PWM) current amplifiers in their analysis of a linear brushless permanent-magnet motor (LBPMM). Through transforming the control force into equivalent three-phase current signals, the motor is effectively controlled. Also, foregoing the rigorous model for experimental validation, errors are kept to a minimum with data supplying motor constants instead of theoretical values. The control scheme was built off a similar application for multi-dimensional positioning of a platen, developed by Kim et al. [9].

Liu et al. [10] presented a control method to supply robust tracking with a highly responsive, low mass linear motor in the presence of large disturbances. Stability with errors in parameter estimation ability to track with zero overshoot overshoot limitations are their primary concerns. Their method is more a more straightforward state-space design compared with the methods of control demonstrated by Liu, Lee and Chang [11]. While the motor in their entry is not quite the same, a range of control schemes that adapt to changes in plant properties are presented. Specifically, two methods of interest are their backstepping adaptive design and a self-tuning adaptive design. The latter lumps all unknowns in a "bulk" variation variable, which differs from the self-tuning method that tries to identify values of specific estimated parameters. Success achieved was equal in their presentation of tracking various position references.

Adaptive control is also applied to a brushless DC servo motor by Ohishi et al. [12]. Their goal for robust position tracking if facilitated by both a model reference adaptive controller (similar to the self-tuning control from [11]) and a passive adaptive controller, which converges in a control scheme that parallels another traditional controller. Its inputs are added downstream of the other control, thus adjusting the control force output supplementally.

2. Experimental Model

There are many suspension models available ranging from incredibly complex to quite simple. For instance, Barak and Sachs [13] utilized a multi-degree-of-freedom model that incorporates a rigid car sprung mass coupled to 4 independent unsprung masses via springs, dampers, and actuators, which are in turn coupled to the ground profile through springs and dampers simulating the tires.

Malek and Hedrick [14] recognized the interconnections between the automotive systems and create a model consisting of the pitch, heave, roll, and warp of the road as well as the roll, heave, and pitch of the car body as the independent degrees of freedom. They suggested that this design method "improves body isolation and fore-aft tire load transfer". However, an increase in the effects of road disturbance on lateral load transfer was expected.

Hrovat [1] presented active suspension designs that introduce dynamic absorbers to the unsprung mass. His work suggested that proper design of the dynamic absorber reduces the two degree-of-freedom (DOF) quarter car model can be reduced to a one DOF system, thus eliminating modeling of the unsprung mass.

Levitt and Zorka [15] discussed the importance of including tire damping in the model, as "setting the tire damping ratio to 0.02 [from zero] reduces rms body acceleration by 30 percent." They also argued that maintaining a nonzero damping ratio the motions of the two masses in a quarter-car model remain coupled, contrary to the notion of becoming uncoupled at the wheelhop frequency.

3. Active Suspension Control

Controlling the actuator is another area in which there are seemingly endless supplies of algorithms that can be applied. The complexity spans from classical linear lead-lag and state-space controllers to an entangled array of artificial neural networks supplying intelligent feedback [16], as well as H_∞ controllers [17].

Common approaches deliver control optimization techniques to attempt and balance the road-gripping performance as well as sprung mass vibration isolation. Revisiting Fathy, et al. [5], they presented an optimization scheme that identifies the best combination of plant and controller simultaneously, citing that "sequentially optimizing a system's plant (i.e., passive components) and controller (i.e., active components) does not account for [the interaction between plant and controller] and hence fails to guarantee system optimality." Their suggestion was expanding the use of a linear quadratic minimization scheme to include "energies" of the spring and damper components. Barach and Sachs [13] employed similar techniques on their multi DOF system. Gobbi et al. [18] presented a combination of the optimization and robust design for control. Additionally, they expand on acceleration transmissibility and tire contact to include maximization of the distance between the sprung and unsprung masses as a performance index.

Adaptive control is another topic discussed in active suspension control design. Building off the adaptive position controllers mentioned in Section I.B.1, Sunwoo and Cheok [19] take the linear self-tuning control like that presented in [11], but use a third order polynomial to define a nonlinear model representing spring and dashpot characteristics. Rajamani and Hedrick [6] develop an adaptive controller using state-space techniques to act as an observer for the road-disturbance and (in their hydraulic actuation) the dry friction present in the actuation control valve.

C. Research Objectives and Proposed Approach

Given the motivation of the previous experimentation discussed earlier, the outcomes expected at thesis completion are:

1) Construction of a quarter-car model using the linear brushless permanent-magnet motor presented in [8]
2) Determination of control algorithms to suit certain performance requirements

3) Experimental validation of the control algorithms with the constructed quarter-car model

1. Proposed Approach

A portion of this Master's thesis will be the design and fabrication of a quarter-car model incorporating the LBPMM developed in [8]. The main contribution, however, will be the active-suspension algorithms to be devised to actively control the motion of the quarter-car model.

In order to complete these tasks, the parameters of the quarter car model must be chosen so that the motor has sufficient force to adequately produce the motion. Once these parameter values have been obtained, the test rig is to be designed and fabricated according to these specifications. The model parameters will then be experimentally established in order to construct a simulation model.

Once the simulation model is complete, control algorithms will be designed and implemented. Finally, the algorithms will be executed on the actual test rig, ensuring that the desired outputs are achieved.

2. Proposed Experimental Test Rig

Figure I-1 depicts the layout of the test rig to be used to experimentally validate the control algorithms to be developed. Accelerometers will be placed on the sprung and unsprung masses to monitor the acceleration of the two, and a linear variable differential transformer (LVDT) will be placed to record the change in distance between the sprung and unsprung masses. Both the unsprung and sprung masses are constrained to motion in only the vertical direction. The system will be excited by road profile simulations drawn under the wheel (not shown) in Figure I-1.

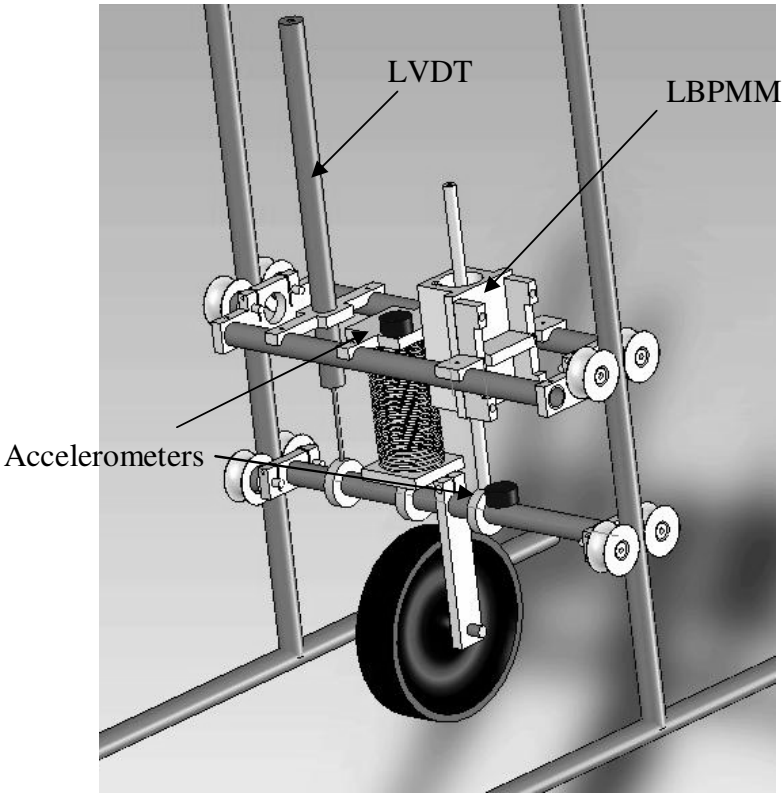

Figure I-1 Proposed experimental test rig

The system will be monitored and controlled using a personal computer fitted with a dSPACE® digital-signal-processing (DSP) board and dSPACE® software. Once the control algorithms have been designed in Simulink®, the file will be converted and loaded onto the dSPACE® platform. The control input, designated by the user, as well as the sensed output gathered by the DSP board is sent to dSPACE® which, in turn, produces control signals sent to each of three PWM amplifiers. These amplifiers emit a current corresponding to the dSPACE® control output, which powers the LBPMM. The accelerometers and LVDT sense the response of the system, which is sent to the DSP board. Finally, the system is monitored in dSPACE® window on the personal computer. Figure I-2 shows the signal flow described above.

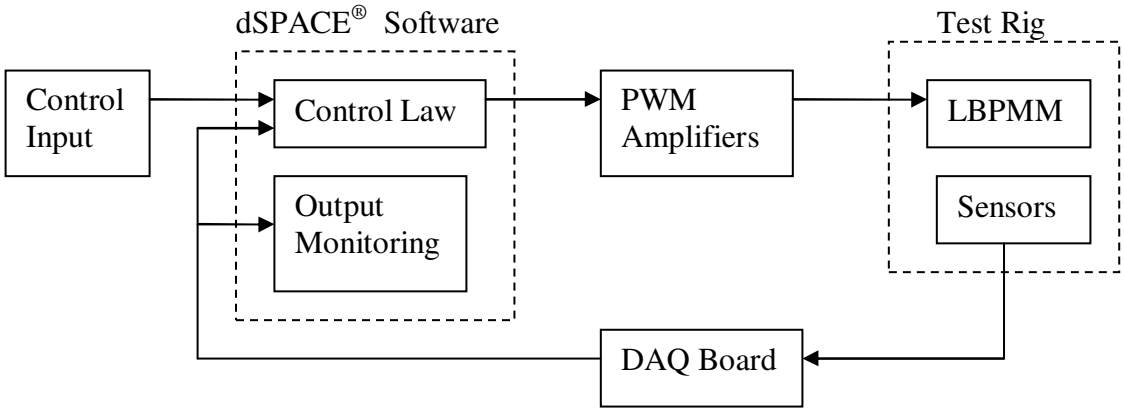

Figure I-2 Signal routing diagram

D. Thesis Overview

This thesis spans the work covering design, fabrication, implementation, and analysis to date. All important information that was gathered or contributed in any way to the formulation of the work presented is covered in great detail. Findings that were discovered after experimentation are not explicitly mentioned in the pages of the development and implementation, but explained in Chapter VIII, which includes suggestions for continuation that arose during analysis.

The layout of the thesis is chronological to the order it was conducted. Beginning, Chapter II covers the development of the test rig and introduction of all associated electromechanical elements utilized. Chapter III details all the work for experimental verification and calibration of equipment, as well as the discussion concerning three-phase decomposition of the motor. Controller design and development is covered in Chapter IV, immediately followed by a rigorous simulation in Chapter V. Sensor contributions to dynamic instabilities in the form of noise and chosen methods of attenuation headline Chapter VI. Also, preparation for dSPACE® implementation is included in that chapter. Results are discussed in Chapter VII, rounding out with the conclusions and future work presented in Chapter VIII.

E. Contribution of Thesis

The contribution of this thesis includes construction of a rig capable of experimentally determining the effectiveness of the novel LBPMM developed in [8]. Also, the design and execution of control algorithms play a large role. Finally, preparation for experimentation in the form of recommended future work is a useful outcome of this thesis.

II. ELECTROMECHANICAL DESIGN

A. Overview

In order to experimentally validate the active suspension control, three major components are required: a mechanical system simulating a quarter-car suspension model, an actuator providing forces to control the mechanical system, and a computer interface to implement the control output via real-time feedback and output. Through the combination of these three subsystems, the project is able to be accomplished and the control programs verified.

The diagram of a common independent suspension setup is shown in Figure II-1.

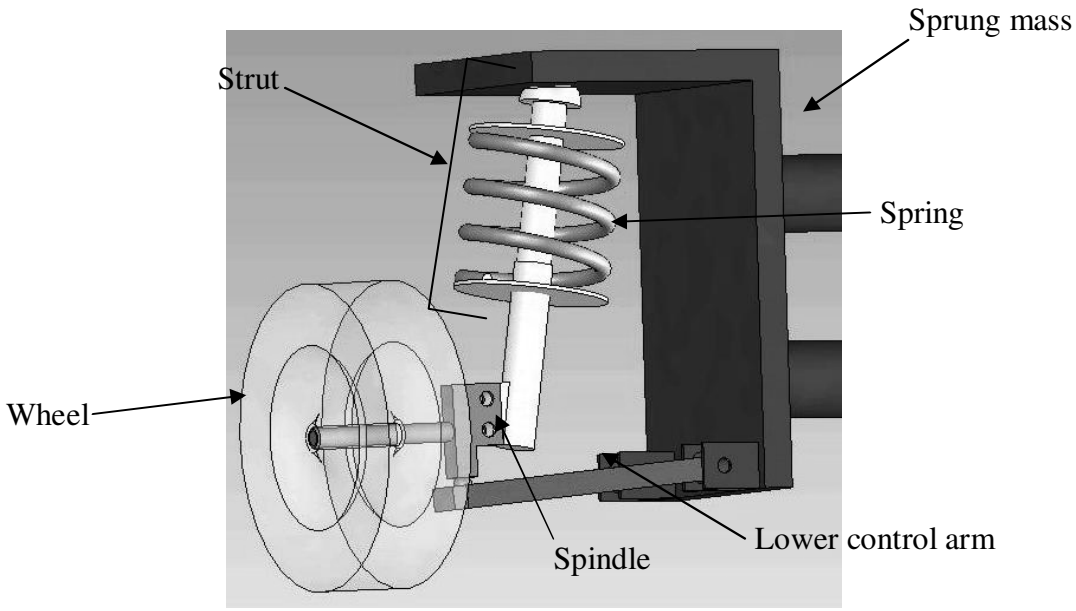

Figure II-1 Common independent suspension layout

This design features a lower control arm that pivots at the body (sprung mass) and is connected to the wheel spindle at a ball joint. All masses not supported by the spring (lower control arm, spindle, wheel, lower strut) constitute the unsprung mass. The wheel spindle rigidly connects with the lower strut mount, which houses the passive damping

element as and acts as the upper control arm of this style of suspension. The strut is free to pivot at the sprung mass and this, coupled with the rotating ability of the ball joint at the spindle, allows the wheel to translate vertically. The lower control arm constrains lateral or fore-aft translation of the wheel via the direct connection to the sprung mass.

The actuator must be situated in order to control the relative motion between the sprung and unsprung masses. Since an active force is available, both the spring and damper could be removed and replaced solely with the actuator; however the continuous force required to support the static load of the sprung mass would be unreasonable. Still, removing the damper would be acceptable, and in some cases beneficial, since the control force would include those resisting motion between the two masses when required. In addition, the actuation force would not be dissipated through the motion of the damper.

The ideal experimental setup would be one that combines all of these attributes of Figure II-1, but with less nonlinearity in its motion, making a more simplistic model for simulation and validation purposes

B. Electromechanical Actuation

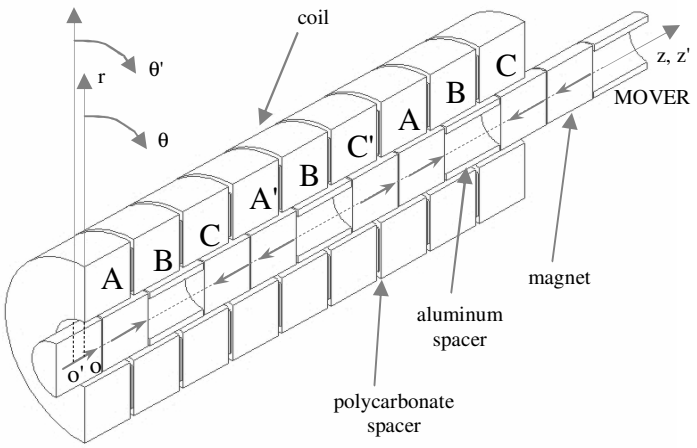

Figure II-2 Diagram of LBPMM showing coil phases and magnet orientation [8]

To actively control the system, a device must be chosen that is compact enough to fit in constrictive spaces limited by other components in the suspension. For this, the LBPMM developed by Kim and Murphy [8] is chosen. This motor is a tubular linear actuator, which allows for direct implementation into the suspension, i.e. no conversion from rotary motion or fluid pressure is needed to provide the force. A diagram of the internal components of the LBPMM is shown in Figure II-2.

The coils are represented by the cylinders marked ‘A’, ‘B’, and ‘C’ and are constrained to 120° of electrical pitch, producing balanced three-phase operation. The prime notation dictates the portion of electrical pitch that is 180° out of phase. The magnets are aligned with the arrow pointing to the ‘N’ pole. The pitch of these magnets is kept the same as that of the coils.

The LBPMM design in Figure II-2 eliminates dead coil windings and employs high energy product density neodymium-iron-boron (NdFeB) magnets, which increases the force-to-mass ratio, creating a viable and compact solution to providing the force necessary to control the experimental model. When given a maximum current of 3 A across each of the three sets of coils, the LBPMM has the ability to produce a 28.9 N force [20], while having a mass of 1.09 kg. An experimental analysis characterizing the LBPMM’s dynamics is accounted for in Chapter III. The values yielded are a force constant of 7.24 N/A, which will be necessary in modeling the system for controller design. The LBPMM is pictured in Figure II-3.

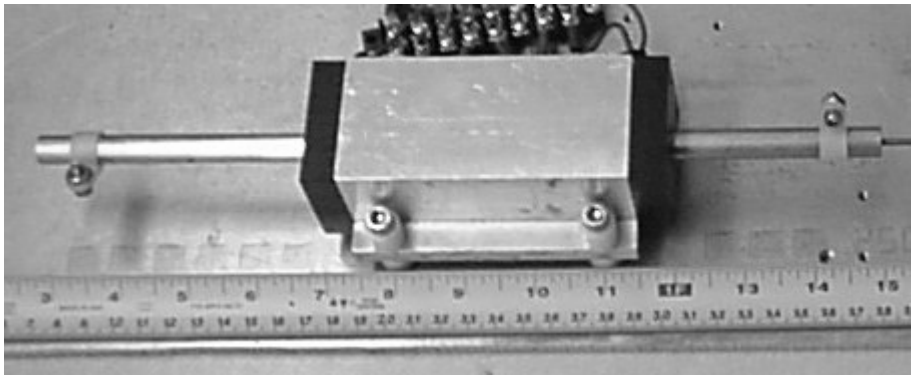

Figure II-3 Picure of LBPMM attached to a table

Three PWM amplifiers Model 12A8K made by Advanced Motion Controls[1] manage the current passing through the coils. Each amplifier has the capability of outputting ±6A continuously. To power these amplifiers, each is fed by a Lambda Electronics[2] Model LZS-250-3 regulated power supply, able to provide 262.5 W of power in a range of 18.0 – 29.4 V. Since the maximum current output is 6 A and each coil set has a resistance of 1.565 Ω, 18.0 V is set as the voltage output. Using the experimental methods discussed in Chapter III, the gains for the PWM amplifiers are 0.6584 A/V, 0.6934 A/V, and 0.6113 A/V for the amplifiers supplying coils A, B, and C, respectively.

C. Mechanical System Design

1. Theoretical Apparatus

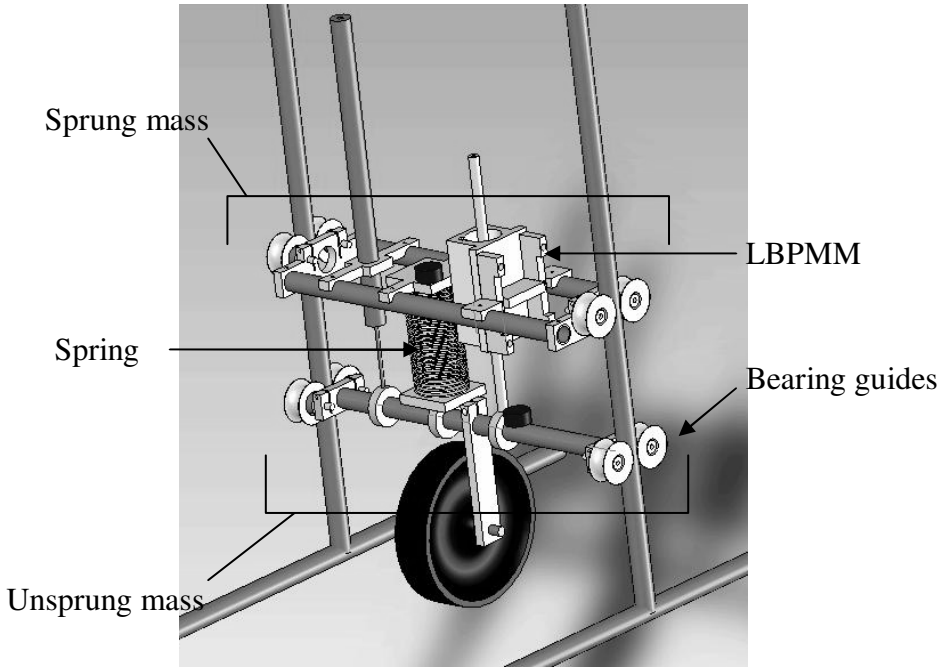

Figure II-4 Proposed active control quarter-car model

[1] Advanced Motion Controls, 3805 Calle Tecate, Camarillo, CA 93102
[2] Lambda Power, 3055 Del Sol Blvd, San Diego, CA 92154

An experimental rig is created which removes the aforementioned nonlinearities due to motion constraints of Figure II-1. Figure II-4 models the motion of the typical system without incorporating the rotational motion of the lower control arm and strut. The two masses are constrained to only vertical translation via bearing guides riding on the guide rails. Although the model presented is not a direct representation of an actual automotive suspension, the motion (and control) of such can be easily adapted for any situation. For these reasons, this suspension design is chosen as the foundation for experimental assessment.

2. Physical Design Constraints

Although the LBPMM is capable of a large force-to-mass ratio, the maximum force attainable with the given instrumentation is around 52 N. Thus the sprung mass must be light enough to be responsive to such a force. Estimating the largest disturbance acceleration to be controlled as two times the gravitational acceleration, the sprung mass must remain at around 2.5 kg. The controller design is constrained to a 10-Hz bandwidth, so the system components must be rigid enough in order to ensure structural deformation and corresponding to modes of vibration do not interfere with the measurement of the system dynamics. Also, most automobiles have suspensions tuned to a low natural frequency, allowing attenuation of large disturbance frequencies, so a spring must be chosen to allow for such a frequency, given the sprung mass properties. After an assortment of springs was studied on the assembled experimental setup (m_s = 3.299 kg), the spring chosen is part number 11813 from Century Spring[3]. Data from the manufacturer denotes the unsprung length as 0.110 m (4.340") and the nominal spring rate of 1385 N/m (7.900 lb_f/in). Theoretically, the natural frequency should be around 3.26 Hz, and experimental verification presented in Chapter III supports this, with the extracted natural frequency around 3.5 Hz. This experimental determination supports the validation of a more realistic spring rate of 1521 N/m, which will be used exclusively for controller design and simulation.

[3] Century Spring, 222 E. 16th Street Los Angeles, CA 90015

The wheel selected is constructed of ABS plastic and loaded with needle bearings. This lightweight construction keeps the mass at as nearly a proportional value to the sprung mass as possible. Instead of an inflated tire surface, a viscoelastic material lines the circumference, providing stiffness and damping comparable to its respective counterpart. Although these material characteristics were not known, for modeling purposes the stiffness and damping coefficients were chosen to be 10 kN/m and 10 N-s/m, respectively. During simulations, however, these values are adjusted to examine their effect in control.

One drawback is the LBPMM from [8] was not built to handle such large current loads. The components cannot operate at high temperatures. The bondable layer fusing the wire coils together has a melting point of 105°C and the magnets in the mover cannot be heated above 150°C, or else magnetic intensity is permanently lost. Thus, an analysis of the heat dissipation required to maintain these temperatures internally.

3. Cooling System Design

Examining a worst case scenario, the coils would be running continuously 5 A of current in each set, equating the heat flux into the system to 120 W, based on (2-1).

$$P = I^2 R \tag{2-1}$$

In the above equation P is power (W), I is current (A), and R is resistance (Ω). As a safety measure, the temperature of the coils is set at a maximum of 80°C, and so the conductance of this heat through the body of the LBPMM must begin with this value.

The conduction analysis is modeled as heat passing through two cylindrical bodies, one composed of the epoxy securing the coils to the housing, and other being the aluminum housing. To simplify calculation, the housing was modeled as a cylinder with a thickness calculated by averaging the radial thickness of the rectangular housing. Since the difference of radial distances to the surface are not of a large magnitude and given the

high conduction coefficient of aluminum (167 W/(m-K) [21]) the assumption is valid. The equivalent-resistance conduction equation of (2-2) is given in [21].

$$q_r = \frac{T_a - T_b}{R_{tot}} \tag{2-2}$$

The above equation relates the radial heat transfer to the temperature difference ($T_a - T_b$) multiplied by the inverse of the total thermal resistance (R_{tot}), which is given by (2-3).

$$R = \frac{\ln\left(r_2 / r_1\right)}{2\pi L k} \tag{2-3}$$

In (2-3), r_1 and r_2 are the inner and outer radii of the medium, while L is the length of the medium and k is its coefficient of thermal conductivity. The total thermal resistance of both the epoxy and the aluminum is the summation of each respective resistance, and given that L is 0.085 m and the thermal conductivities of EPO-TEK 930-4 epoxy[4] and aluminum are 1.1 W/(m-K) and 167 W/(m-K), respectively, the resulting external temperature that must be maintained is 63.7°C.

Originally, the addition of fins was the most desirable solution due to the apparent ease of addition and the least external hardware. However, the fins that were chosen would have needed an air supply traveling at around 50 m/s which is unattainable in the lab. Increasing the fin size was not an option as the large increase in mass would be detrimental to the dynamics of the sprung mass.

The next option is cooling with liquid traveling through passages connected to the LBPMM. This method is highly successful at removing heat, however implementation is somewhat difficult due to the addition of bulky components to the system. However, according to (2-4),

[4] Epoxy Technology, 14 Fortune Drive Billerca, MA 01821

$$q = \dot{m} C_P \Delta T \tag{2-4}$$

where $\dot{m}$ is the mass flow rate, C_P is the specific heat of the fluid, and ΔT is the temperature gradient between the fluid and the surface, the mass flow of water at 20°C required to remove the heat is 0.7 g/s.

To pump the fluid, a Rule[5] submersible bilge pump capable of providing 1890 L/hr is chosen. Although the calculated flow assumes perfect heat transfer to capacity of the fluid, the chosen pump can ideally provide 45000 times more water volume than needed. This allows more rigorous convective heat transfer calculations associated with a heat exchanger to be avoided.

The fluid is routed through 19.05 mm I.D. clear vinyl tubing which branches into two paths of 12.7 mm I.D. tubing. This is connected to flattened copper tubing fixed to the LBPMM as shown in Figure II-5.

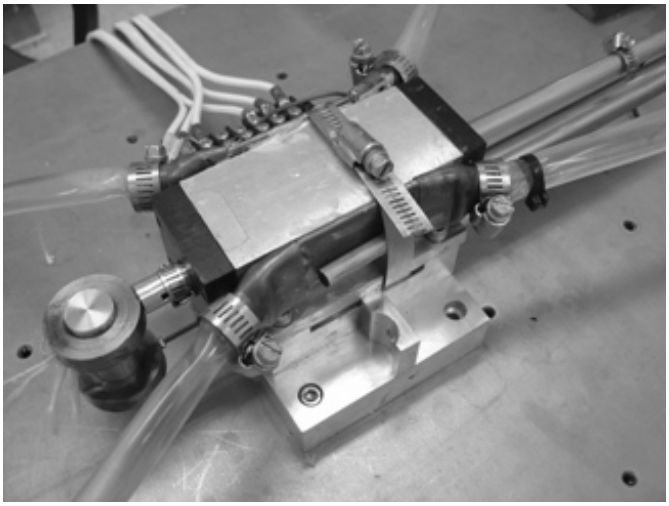

Figure II-5 Picture of LBPMM with coolant lines attached

The copper tubing is flattened from ¾" type M copper tubing to an external thickness of around 6 mm. Adapters are soldered to this tube to allow clamping surface for the hoses that supply and remove the coolant. To increase the heat transfer conduction between the copper tubing and the LBPMM, a layer of Dynex[6] Silver thermal

[5] Rule Industries, Cape Ann Industrial Park Gloucester, MA 01930
[6] Dynex, 7601 Penn South Richfield, MN 55243

compound is applied to increase the surface contact area, and boasts a thermal conductivity greater than 8.2 W/(m-K).

With the cooling system in place and each coil carrying a current of 5 A, the internal surface temperature of the coils requires 2 minutes 30 seconds to increase from room temperature (20°C) to the maximum temperature of 80°C. This validates the effectiveness of the cooling system, as before it only took seconds for the aforementioned increase to take place. And, because this condition would only occur in transients lasting much shorter periods, the cooling is more than adequate.

4. Disturbance Input

In order to excite the quarter-car model, the base is modified to allow for a motor-driven camshaft. Figure II-6 depicts the base design including the camshaft and lobe

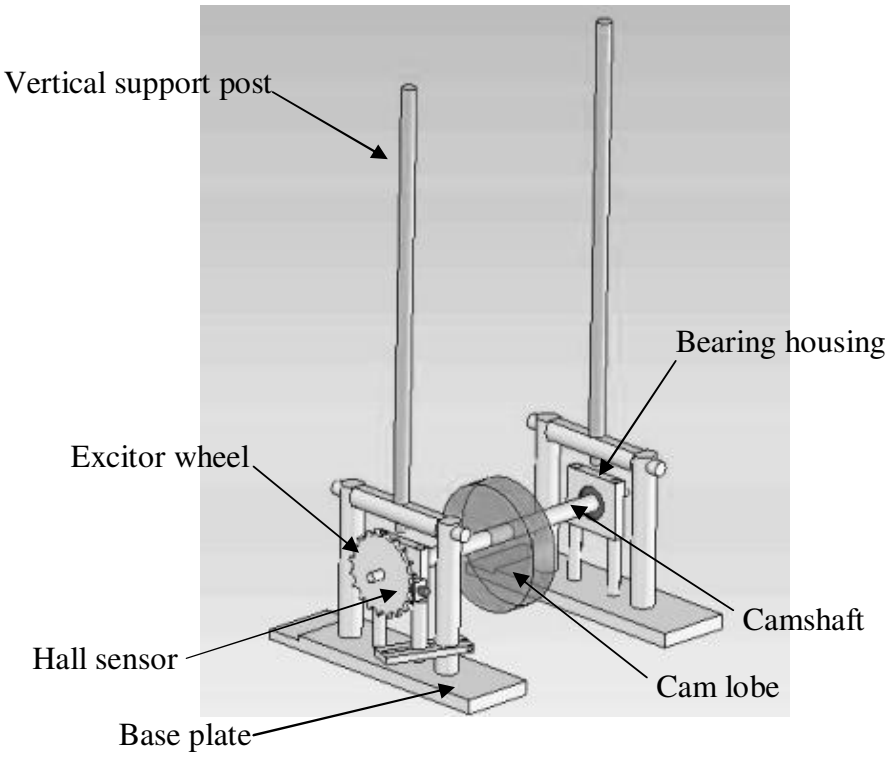

Figure II-6 Support base featuring disturbance input camshaft and lobe

This camshaft has replaceable lobes simulating different types of disturbances: sinusoidal and pulse. Each lobe contains one period per revolution, resulting in the ability to vary input disturbance frequencies by altering the angular velocity of the shaft.

With the sprung and unsprung mass bearing guides (Figure II-4) traveling along the vertical support posts, the wheel rests on the cam lobe. Rotating the camshaft, secured by the bearing supports, induces corresponding motion on the wheel (simulating road profiles). Monitoring the angular velocity of the cam is the Hall sensor, signaled by the passing of ferrous excitor wheel teeth across its surface. The operation of the Hall sensor is discussed more in Section II.D.2.

5. Material Selection

As mentioned above, the test rig must be rigid enough as not to greatly influence the sensed motion of the system. For instance, if either the sprung or unsprung mass contains a flexural mode around the frequency the system is being agitated, there will be discrepancies between the sensed motion and the actual motion. Concurrently, the sprung mass must be light enough to ensure the LBPMM will have enough force to control its motion. Therefore, the materials used are important.

For the cross members in the sprung and unsprung masses, thin-walled chrome-moly (AISI 4130 steel) tubing is the material choice. Combining large stiffness with small mass, the tubing is ideal for this situation. Using a finite-element algorithm for flexural displacement of an Euler beam, the first four natural frequencies are calculated. Employing one element along the 0.305 m length of tubing, the lowest mode that is not associated with rigid body dynamics is around 1500 Hz, well above the disturbance frequencies encountered in the experiment. Note that this calculation was conducted solely on one support beam. The addition of the other components that attach to the beam will constrain motion even more, causing the natural frequency predicted to be much higher.

The vertical support posts are constructed of solid aluminum bars due to its ease of manufacture and non-corrosive nature. Since the sprung and unsprung masses are not

responsive to axial deformations of the posts, their motion can be neglected. However, since the sensors could pick up motion that is not purely vertical, the same analysis is run as above, except observing that motion at the lower end is constrained to zero. With a length of 0.56 m and diameter of 0.019 m, using the appropriate values for 6061 Aluminum reveals the lowest natural frequency to be around 40 Hz. This is closer to the bandwidth of the desired controller, but it is still 4 times greater, so the motion of the beam should not affect readings if the sensor output is attenuated at these frequencies.

Knowing these to be the most crucial areas for vibration analysis, the rest of the test rig can be assumed rigid, as the diameters of the other structural components are larger than 0.019 m or are much shorter. This validates the assumption that their corresponding natural frequencies are higher than those analyzed.

All structural components not mentioned are machined out of 6061 aluminum, except for the bearing guides, base plates, and excitor wheel. These are made of carbon steel. The base plate (Figure II-6) material selection adds mass to the base creating a more stable footing on the table, not as susceptible to movement during testing. The bearing guides (Figure II-4) are machined from carbon steel because they have thin flanges that constrain the motion of the sprung and unsprung masses in a vertical direction. The modulus of elasticity of steel is much higher than aluminum, making these flanges more resistant to local deformation. Because the Hall switch requires a ferrous material crossing its sensing surface to operate properly, the excitor wheel was machined from carbon steel as well.

Based upon the above calculations, the test rig design is structurally rigid for the application at hand. An experimental vibration analysis of the sprung mass is undertaken and discussed in Chapter III to determine the natural frequency of the mass-spring system. In addition, the same analysis is conducted on the vertical support post to help determine the attenuation frequency that needs to be adapted in the controller.

D. Data Acquisition and Control

The motion of the system is monitored via sensors mounted on the experimental test rig and fed into a personal computer. The software then calculates the corresponding force needed to control the system and the signal is sent to the PWM amplifiers. The amplifiers then generate the current necessary to produce such a force.

1. DS1104 Controller Board

To monitor sensed outputs and provide actuation signals, a personal computer outfitted with a dSPACE® DS1104 DSP controller board. Among other connections available, the board is equipped with four 16-bit analog-to-digital (A/D) and four 12-bit A/D channels to gather the observed data, which operate in the range of ±10 VDC. Eight 16-bit digital-to-analog (D/A) interfaces for control output in the range of ±10 VDC to amplifiers or actuators. The software supplied is Control Desk Developer Version 2.1.1, which uses Matlab 6.1.0.450 (R12.1) Simulink® for control algorithm design. Control Desk contains a graphical user interface (GUI), allowing data acquisition to be displayed on layouts via drag-and-drop virtual instruments. Saving data to file is also possible through Control Desk's data capture abilities.

2. Motion Sensing

To gauge system excitation, sensors are placed as in Figure II-7. An accelerometer is placed on each mass, and a linear variable differential transformer (LVDT) monitors the displacements of the sprung and unsprung masses relative to each other.

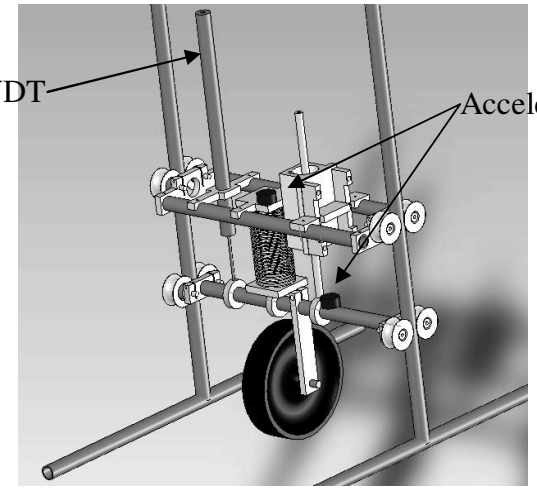

Figure II-7 Sensor positioning on experimental apparatus

Sensing the displacement of the unsprung and sprung mass relative to each other is the LVDT, Schaevitz Sensors model DC-SE 4000. Internally, the basic components are a powered primary coil, two unpowered secondary coils, and a moving iron core. The orientations of these are diagrammed in Figure II-8.

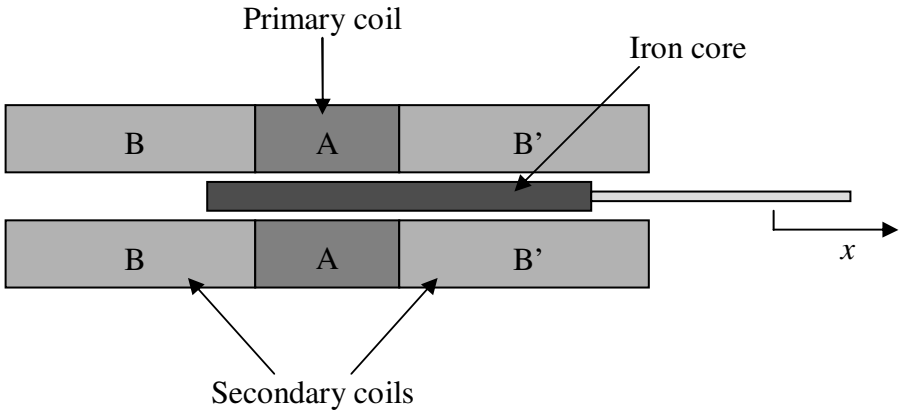

Figure II-8 Diagram of internal components of LVDT

The two identical secondary coils are placed on opposite sides of the primary coil, with the terminals connected in such a way that the current phase is opposite each other (denoted by B and B' in Figure II-8). The position of the iron core (x) induces a magnetic flux on the secondary coils, created by the effects of the alternating current in primary coil A. The opposite phase produces a net voltage according to the length of the iron core in each respective secondary coil. For example, when the iron core length in

each coil is equal, the net voltage is zero (they cancel each other out). When the length is greater in one than the other, the corresponding net voltage magnitude and phase angle changes. These values determine the location of the iron core within the housing.

The chosen LVDT requires a 10-VDC input, supplied by Agilent 3644A programmable power supply, which it converts internally to an AC voltage. The output is a linear voltage signal between 0–5 VDC, capable of observing 0.1016 m of travel and frequencies up to 200 Hz.

The sprung mass acceleration is monitored by PCB[7] model 356B18 (serial number 25571), a tri-axis accelerometer being recorded solely in the *z*-axis (vertical motion). PCB accelerometer model 353B15 (serial number 77353) observes the acceleration of the unsprung mass. The basic working components of these accelerometers are featured in Figure II-9, with (2-5) governing the dynamics of the system.

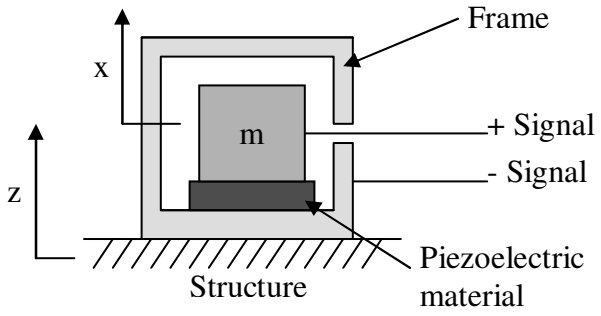

Figure II-9 Diagram of accelerometer components

$$m\ddot{x} = k_p\left(z - x\right) + c_p\left(\dot{z} - \dot{x}\right) \tag{2-5}$$

Equation (2-5) equates the force acting on the mass *m* is equal to the of the piezoelectric material due to the difference in motion of the mass (*x*) and structure (*z*), with known piezoelectric spring constant k_p and damping coefficient c_p. Dividing through by *m* results in the acceleration of *x*. Provided that the stiffness k_p of the piezoelectric material is sufficiently high and the mass *m* is low, the internal natural frequency is well above the prescribed frequency range of the sensor, resulting in a

[7] PCB Piezotronics, 3425 Walden Avenue Depew, NY 14043

response in *x* that is linearly proportional with that of *z*. Thus, measuring the acceleration in *x* can be adjusted by a gain factor to describe the acceleration in *z*.

When the piezoelectric material undergoes deformation changes, a small voltage differential output is produced. Effectively, the accelerometer creates a signal proportional to the acceleration of the device structure.

Both accelerometers have a frequency range of 1–10000 Hz. Supplied with these are gain factors of 971 mV/g and 10.28 mV/g for serial numbers 25571 and 77353, respectively, as calibrated by PCB. The Signal Conditioner, PCB model 482A22, provides power to the accelerometers and conditions the voltage fluctuations created to produce a signal output of ±10 VDC.

Although the frequency range being detected is on the low end of the accelerometers' spectrum, they were chosen because larger devices that would shift the measured frequency range would have been much heavier and thus introduced adverse effects given the actuation force of the motor.

As discussed in Section II.C.4, the Hall sensor, Cherry Sensors[8] model GS 100701, records the angular velocity of the disturbance input by monitoring the rate at which the ferrous teeth of the excitor wheel cross its surface. An electrical schematic of the Hall sensor is shown in Figure II-10.

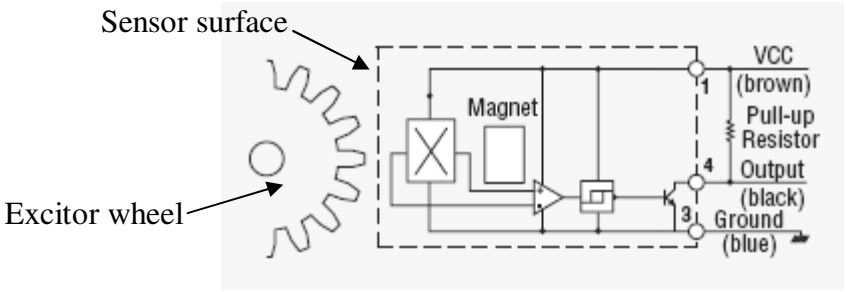

Figure II-10 Electrical schematic showing operation of Hall sensor GS100701[8]

When a tooth moves across the sensor surface, the circuit between the supply voltage (*VCC*) and ground is closed, producing an output of 0 V. On the other hand, when no tooth is present, the output signal is 10 V. An additional requirement is a pull-up

[8] Cherry Corporation, 10411 Corporate Drive #2 Pleasant Prairie, WI 53158

resistor rated at 3 kΩ connected from the supply voltage to the Output wire. Using the voltage increase from 0 V to 10 V as a trigger edge, the DS1104 board records the time differential and prescribed angular rotation. With these, the angular velocity can be calculated. Since the voltage requirements are the same, powering the Hall sensor is the same Agilent 3644A power supply used for the LVDT.

3. LVDT Signal Conditioning

While the A/D channels of the DS1104 have a range of ±10 VDC, the output of the LVDT is only 0–5 VDC. Thus, to increase the resolution of the LVDT, the conditioning circuit presented in [20] is implemented to shift the output range of the LVDT to match that of the A/D channel. In addition, this conditioning board also contains an anti-aliasing filter to reduce the effects of noise present in the signal.

III. EXPERIMENTAL VERIFICATION OF TEST RIG CHARACTERISTICS

For modeling and simulation purposes, it is important to accurately portray the dynamics of the quarter-car test rig. In the following processes, an experimental analysis verifying the characteristics of several key components is carried out, including the force constant for the LBPMM as well as the dynamics of motion pertaining to the quarter-car test rig.

A. PWM Amplifier Calibration

As mentioned in Chapter II, the PWM amplifiers accept a voltage input from the DS1104 DSP board and produce a current proportional to the voltage input. Therefore, the DS1104 must know the gain that relates the voltage received to current produced. In order to evaluate this, the amplifiers must first be adjusted to accommodate the expected output current range.

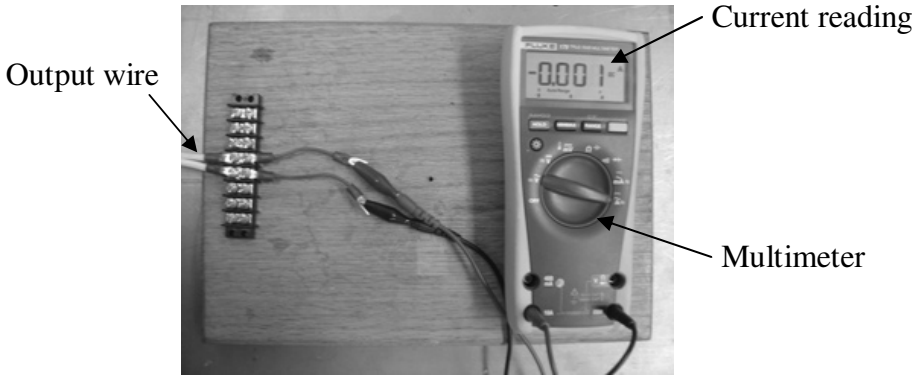

Figure III-1 Direct current output measurement of PWM amplifiers using a multimeter

For both procedures, the voltage adjustment is made in dSPACE®, while the current output from the amplifier is directly measured as shown in Figure III-1 using a Fluke®[9] model 179 True-rms multimeter, capable of ±1% precision.

1. PWM Amplifier Range Adjustment

The PWM amplifier is adjustable to provide output ranges up to ± 6 A continuous current through external potentiometers (pots). The pots have a 10-turn adjustment range and are located on the amplifier as depicted in Figure III-2.

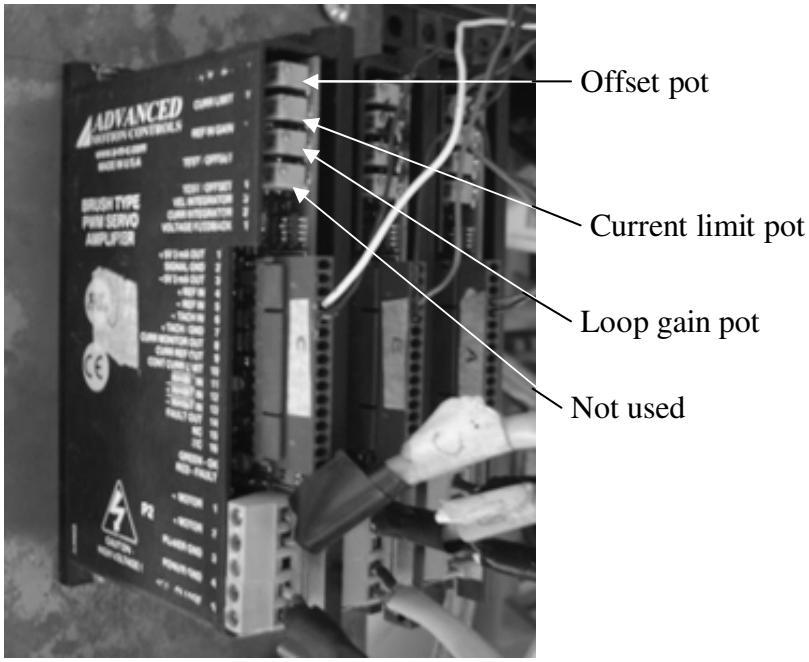

Figure III-2 Picture of PWM amplifiers showing potentiometer location

In order to adjust the output current to the prescribed range with zero offset, the following steps are taken:

1) Set the output voltage from dSPACE® to maximum 10 VDC.
2) Adjust the Offset pot until current measures 0.000 A.

[9] Fluke Corporation, P.O. Box 9090 Everett, WA 98206

3) Increase Current limit pot to maximum.
4) Adjust Loop gain pot until current reading displays 3.000 A.
5) Decrease Current limit pot until current reading displays 2.800 A.
6) Increase Loop gain pot until current reading displays 6.00 A.

Although the current limit is only adjusted to +6 A, the output is presumed linear and thus negative voltage will produce the −6 A portion of the range. Since these amplifiers contain an inner control loop, it is important to keep the loop gains as close as possible to each other. This way the outputs will behave in a similar fashion, and by applying this procedure to all of the amplifiers, the internal loop gains for each amplifier are kept as close as possible with respect to each other.

2. Gain Calibration

Once the PWM amplifiers' ranges have been set, the relationship between input voltage and output current must be established. These gains are used to adjust the output in the controller so dSPACE™ can provide the proportionally correct voltages. For this, the voltages are adjusted incrementally by 1 VDC from +10 VDC to −10 VDC. The corresponding measured current values are allowed to come to equilibrium and then recorded. The currents and voltages are then plotted and fitted with a linear regression trendline. The gains are displayed in Table III-1.

Table III-1 Fitted trendline slope and correlation (R^2) values

	PWM A	PWM B	PWM C
SLOPE (A/V)	0.6854	0.6934	0.6113
R^2	0.9904	0.9957	0.995

Table III-1 demonstrates the discrepancies between each PWM amplifier output. Since the controller outputs three different voltage signals, these gains can be applied to

their corresponding coil amplifier output, producing a result that is closer to desired than lumping them into a single factor for all the amplifiers.

B. LBPMM Evaluation

When modeling a motor (assuming linearity), the constant that relates output force to supplied current (k_f) is required to determine the governing differential equations of motion. Its relationship is given in (3-1).

$$F = k_f i \tag{3-1}$$

One concern is that the constant above describes k_f with respect to a single current. However, the LBPMM operates on three separate currents. Thus, these three currents must be equated to an equivalent single current.

The *dq*-frame in rotating machinery is the coordinate frame fixed to the rotor, with the direct (*d*) axis aligned with the rotor magnetic axis and the quadrature (*q*) axis leading the direct axis by 90° of electrical pitch. Analyzing the Lorentz force equation,

$$\vec{F} = \vec{J} \times \vec{B} \tag{3-2}$$

where the force is equal to the cross product of the current density $\vec{J}$ and the magnetic flux $\vec{B}$, the component of the current density perpendicular to the magnetic flux produces the force. When the stator current is transformed in this manner, the force is merely the product of J_q and $\vec{B}$. Since $\vec{B}$ is aligned with the *d*-axis, the quadrature current will always remain perpendicular to the magnetic flux.

The same relationship holds true for linear motors, with the quadrature current producing axial force. The direct current, however, also produces a lifting force as well. Figure III-3 representing the coordinate frame on the mover of the LBPMM.

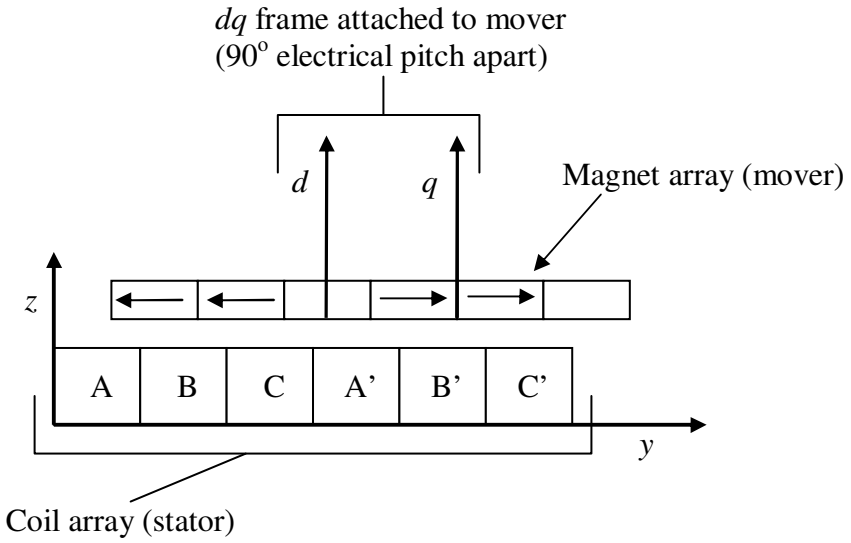

Figure III-3 Diagram of LBPMM with *dq*-frame placed on mover

From [22], the free volume current density due to current-carrying coils spanning one electrical pitch is equated to an infinite complex Fourier series, given in (3-3).

$$J(y) = \sum_{-\infty}^{\infty} \tilde{J}_n e^{-jk_n y} \tag{3-3}$$

From above, $\tilde{J}_n$ denotes the *n*th complex Fourier coefficient corresponding to angle $k_n y$, where k_n equals $2\pi n / l$ and *y* is the distance along the (lateral) *y*-axis. Assuming that the current density along the coils reflects the fundamental sinusoidal pattern, the current density from (3-3) can be simplified to Equation (3-4), which assumes the current density to only be a product of the fundamental Fourier component (evaluation only for *n* equal to 1 and -1) [22]. J_a and. J_b represent the fundamental real and imaginary Fourier coefficients.

$$J_x(y) = 2J_a \cos(k_1 y) + 2J_b \sin(k_1 y) \tag{3-4}$$

Now that the desired current density of the stator has been established, the next step is to map this on the *dq*-frame, so the two dimensional forces can be defined as:

$$F(y) = k_f i_q \tag{3-5}$$

$$F(z) = k_f i_d \tag{3-6}$$

1. *dq* Decomposition

Figure III-4 displays the desired current density waveform components defined in Equation (3-4) at $y = 0$. Included are the respective locations of the stator coils as well as the mover, positioned by the location of the direct and quadrature axes. In Figure III-4, the direct axis (*d)* is aligned with the *z'*-axis (fixed to the mover) and the quadrature (*q*) axis leads the direct axis by π/2 radians of electrical pitch.

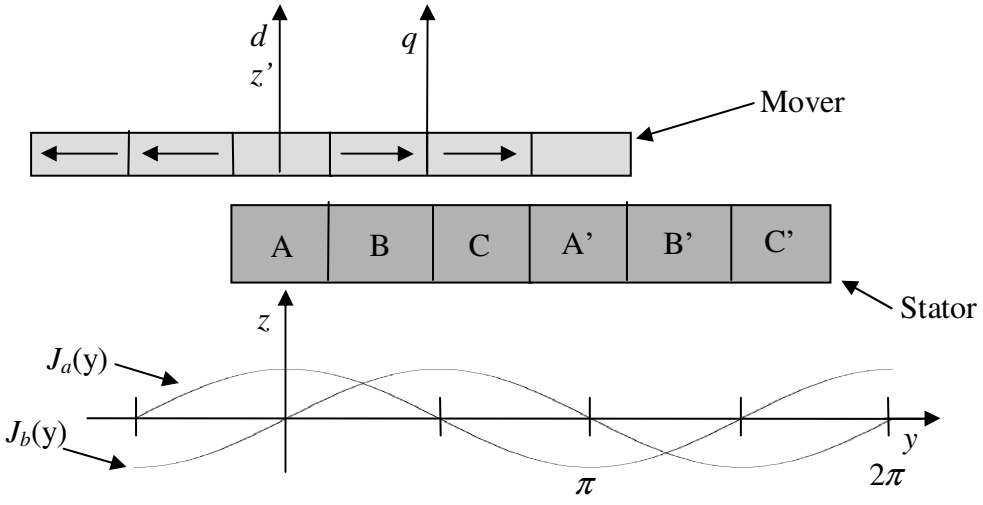

Figure III-4 Diagram of LBPMM showing current density and *dq*-axis location at y = 0

For simplicity and, given the symmetry of the magnetic field, the forces defined by the Lorentz force equation are situated at points corresponding to maximum force output (i.e., the portion of the magnetic field that is perpendicular to the current). The

vertical force component, that location is π/2 radians of electrical pitch ahead of the *d*-axis and π/2 radians of electrical pitch behind the *q*-axis. Therefore, the above mentioned relationships between J_a and J_b and the *dq*-frame defines the transformation presented in (3-7), which agrees with the results given in [22].

$$\begin{bmatrix} J_q \\ J_d \end{bmatrix} = \begin{bmatrix} \cos(k_1 y) & \sin(k_1 y) \\ \cos(k_1 y + \frac{\pi}{2}) & \sin(k_1 y + \frac{\pi}{2}) \end{bmatrix} \begin{bmatrix} J_a \\ J_b \end{bmatrix} = \begin{bmatrix} \cos(k_1 y) & \sin(k_1 y) \\ -\sin(k_1 y) & \cos(k_1 y) \end{bmatrix} \begin{bmatrix} J_a \\ J_b \end{bmatrix} \tag{3-7}$$

Combining (3-5), (3-6), and (3-7), the equivalent forces produced by the current components J_a and J_b result in

$$\begin{bmatrix} f_y \\ f_z \end{bmatrix} = k_f \begin{bmatrix} \cos(k_1 y) & \sin(k_1 y) \\ -\sin(k_1 y) & \cos(k_1 y) \end{bmatrix} \begin{bmatrix} i_a \\ i_b \end{bmatrix} \tag{3-8}$$

Finally, knowing that the physical currents densities J_A, J_B, and J_C are spatially distributed $\pi/3$ radians apart from each other (there are six equally distributed current phases per electrical pitch, and $J_{n'}$ is equal to $-J_n$), the *ab*-plane can be mapped to these physical current densities through the transformation [22] in (3-9).

$$\begin{bmatrix} J_A \\ J_B \\ J_C \end{bmatrix} = \begin{bmatrix} 2 & 0 \\ 2\cos\left(\frac{\pi}{3}\right) & 2\sin\left(\frac{\pi}{3}\right) \\ 2\cos\left(\frac{2\pi}{3}\right) & 2\sin\left(\frac{2\pi}{3}\right) \end{bmatrix} \begin{bmatrix} J_a \\ J_b \end{bmatrix} = T_{32} \begin{bmatrix} J_a \\ J_b \end{bmatrix} \tag{3-9}$$

Since the coils are radially symmetric, f_z cancels out and can be neglected. Thus, after combining (3-5), (3-8) and (3-9). The three phase currents can be related to *dq*-current components. Removing f_z simplifies the resulting equation, and in the end the three coil currents are given by

$$\begin{bmatrix} i_A \\ i_B \\ i_C \end{bmatrix} = T_{32} \begin{bmatrix} \cos(k_1 y) \\ \sin(k_1 y) \end{bmatrix} i_q \tag{3-10}$$

Equation (3-10) is used in the controller to convert the control output (i_q) into the three physical currents needed to actuate the LBPMM, with k_1 equaling the spatial period of the motor, 99.26 rad/m.

2. Force Constant Determination

The information presented in Section III.B.1 is important because it demonstrates that the three coils can be transformed into the current component responsible for producing lateral forces, validating (3-1).

By fixing the control output i_q in dSPACE®, the LBPMM must be able to support a load proportional to the product of this current and k_f.

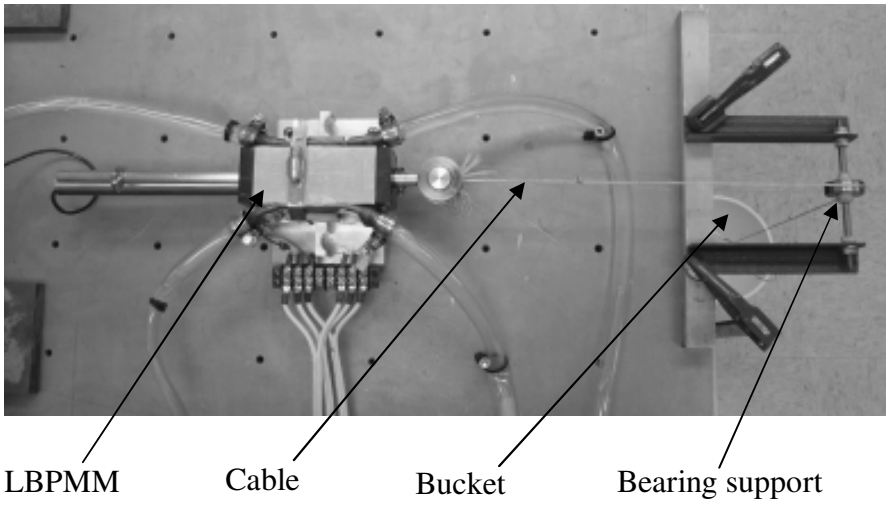

Figure III-5 Picture displaying experimental setup to determine force constant

To measure this load, a cable is fixed at the end of the mover and suspended over the edge of a table across support bearing, while the other end of the cable supports a bucket

that slowly has water added to it. Figure III-5 displays the experimental setup used to determine the force constant. When the weight of the bucket becomes greater than the force created by the LBPMM, the mover becomes dislodged, at which the addition of water is ceased. The mass of the bucket is then measured on a Denver Instrument model APX-6001 precision scale.

This procedure is conducted first with no current to determine the friction force present, yielding a value of 1.110 N. Succeeding this, the force capability at different quadrature currents applied over balanced three-phase current distribution and different locations on the shaft are evaluated. The Simulink® block diagram loaded onto dSPACE® contains the three-phase decomposition of the control output (i_q), and and is given in Appendix II.E.

Ten test runs were completed for each trial, with the highest and lowest values of each removed from the data set. Of the remaining values, the average and sample standard deviation (σ) are calculated. Finally, the mean and σ values are calculated for this data set. The results are tabulated in Table III-2.

Table III-2 Results from force constant determination trials

	Trial 1	***Trial 2***	***Trial 3***	***Trial 4***	***Trial 5***
i_q (A)	0.2500	0.5000	1.0000	2.0000	2.0000
Position (m)	0.0000	0.0000	0.0000	0.0000	0.0200
Support Load (N)	1.8303	3.6610	7.3317	14.6349	13.7855
σ (N)	0.0775	0.0965	0.0658	0.0213	0.0713
k_f, average (N/A)	7.2370				
σ,average (N/A)	0.1925				

The above experiments proved to be very repeatable, with all measured values falling within ±5% of the average. This assures that the force constant calculated is accurate enough to be used for modeling the behavior of the motor.

C. Test Rig Evaluation

Once the force constant has been calculated, the test rig is ready to be assembled. First, the sprung and unsprung mass assemblies are built, followed by measuring their respective masses using the APX-6001 scale. The sprung mass (M_s), with full cooling-jackets and hoses, is recorded at 3.299 kg, while the unsprung mass (M_{us}) is 2.278 kg. These are then slid over the vertical support posts and the spring secured to its upper and lower platforms. The fully assembled test rig is shown in Figure III-6.

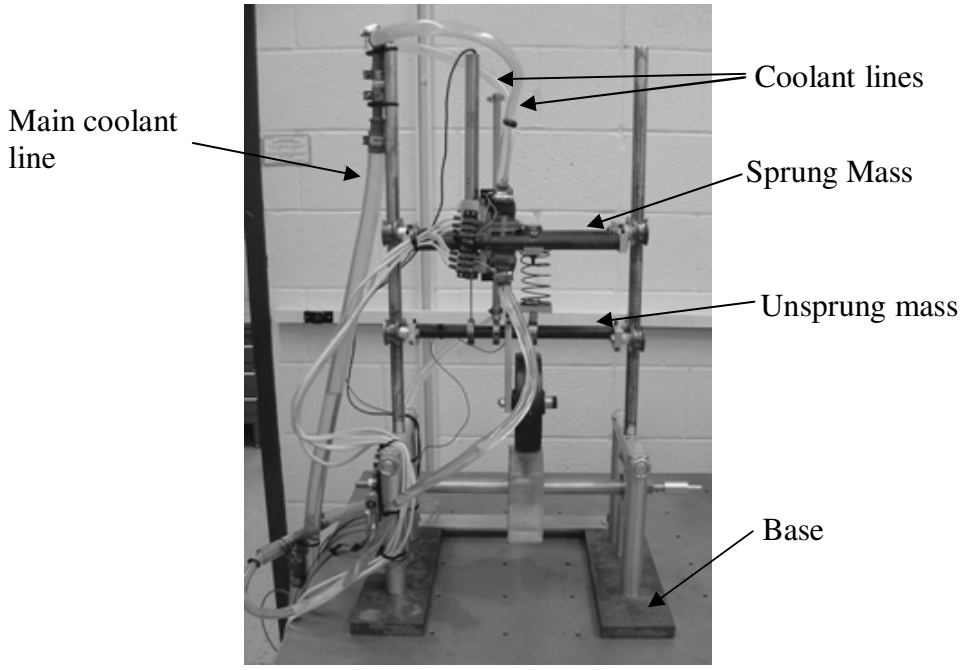

Figure III-6 Fully assembled test rig

Zooming in on the sprung mass, Figure III-7 displays the corresponding component layout, while Figure III-8 closes in on the unsprung mass, revealing the location of important elements.

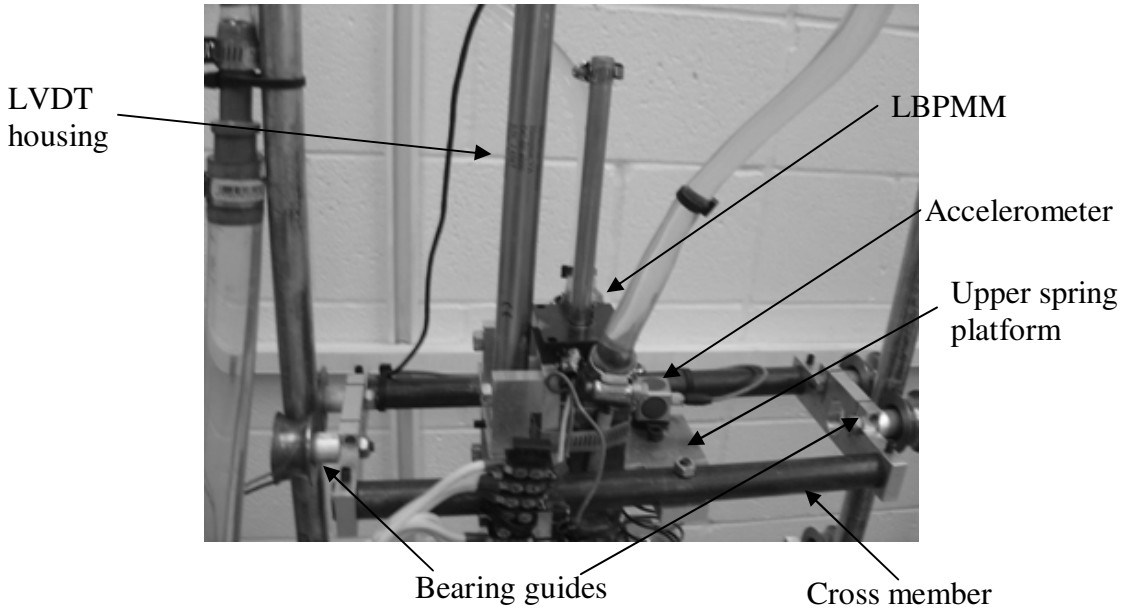

Figure III-7 Sprung mass component layout

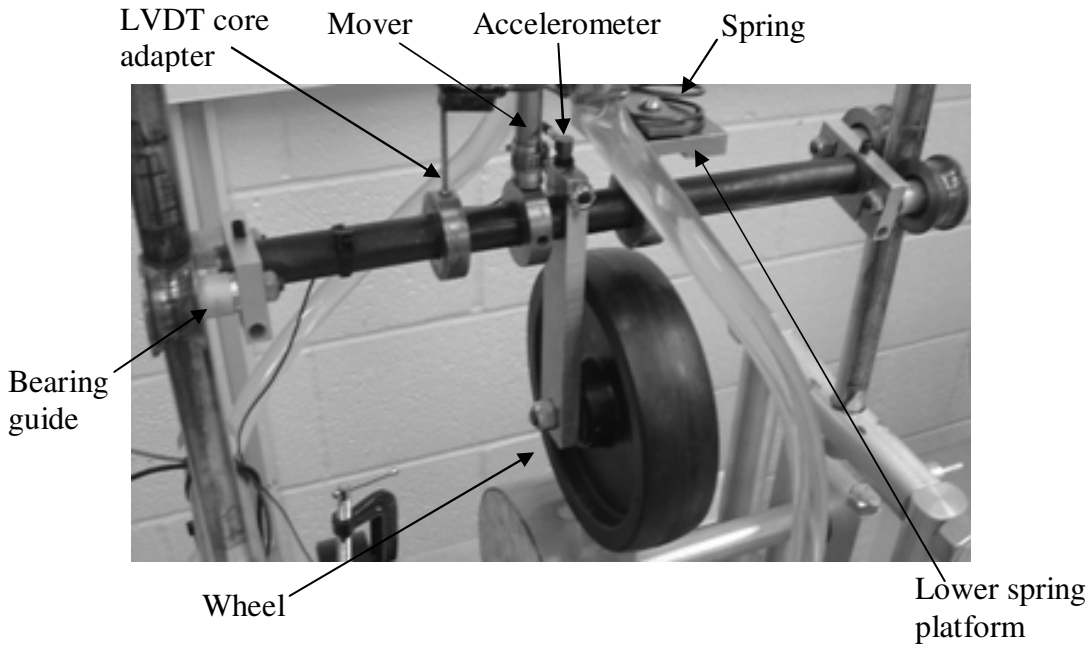

Figure III-8 Unsprung mass component layout

A third view, depicted in Figure III-9, is a close-up of the base, showing the excitation system.

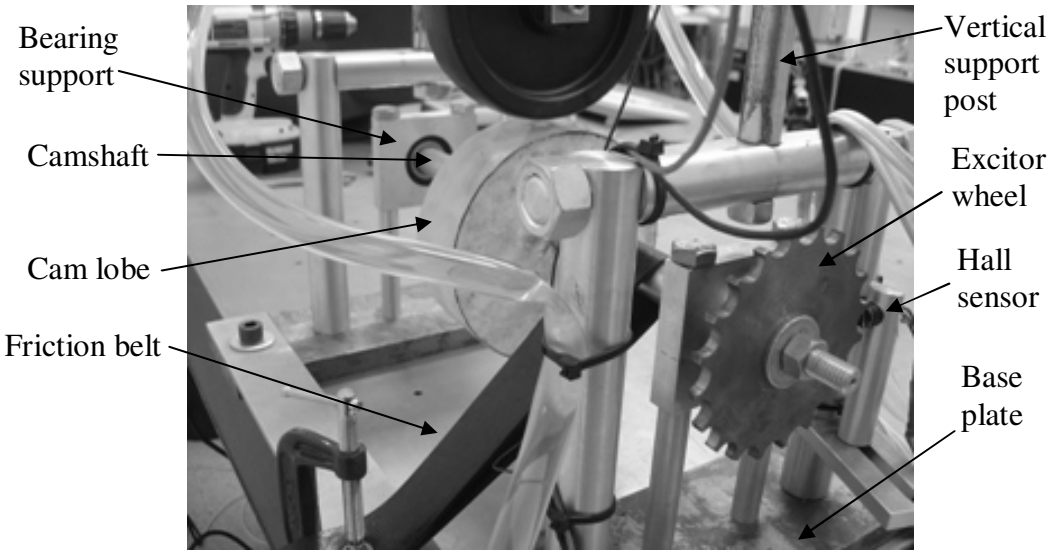

Figure III-9 Picture of base, displaying major components

1. Experimental Determination of Natural Frequencies

With the test rig together, the resonant frequencies of the system due to the oscillation of the sprung mass can be determined. Due to the nature of the test rig being evaluated, there are two mechanical resonant frequencies (given the two bodies of mass).

The natural frequencies are determined by providing an initial deflection to the sprung mass. The sprung mass response is observed by the accelerometer atop it. Providing dSPACE® with the Simulink® block diagram in Appendix II.A, the DSP board captures the motion of the sprung mass after being released from maximum spring compression. A fast-fourier-transform (FFT) magnitude plot of the collected data points is presented in Figure III-10.

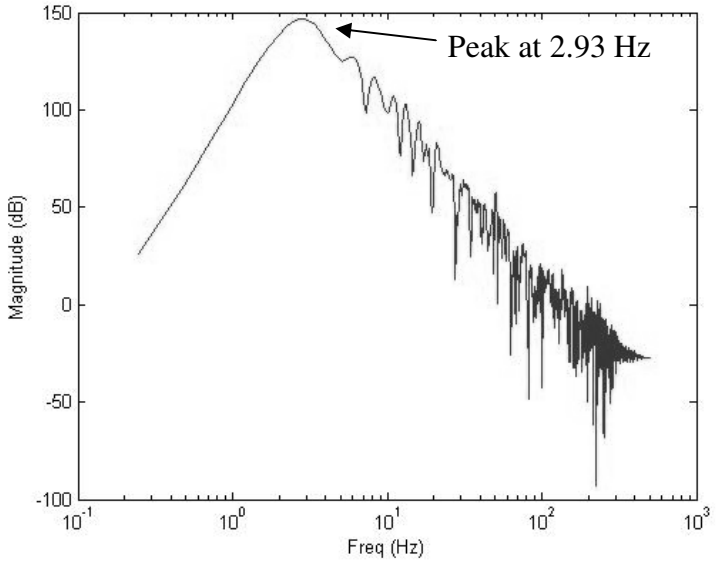

Figure III-10 FFT magnitude plot of sprung mass response to initial displacement

The peak at 2.93 Hz denotes the damped natural frequency of the sprung mass system. The second mode is not captured in the response above, due largely to the overdamped nature of the tire compound chosen and the magnitude of its contribution in comparison to the first mode.

The measurement was taken off an unfiltered LVDT signal, and as the FFT shows, it is quite noisy (a noise analysis is carried out in Chapter VI to clean it up). However, the resonant peak is very pronounced. Figure III-11 displays t he phase plot of the LVDT signal.

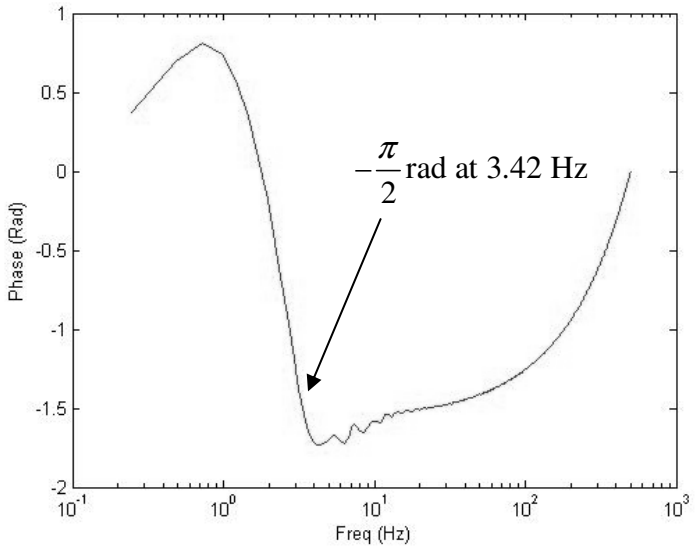

Figure III-11 FFT phase plot of sprung mass response to initial displacement

The undamped natural frequency of the system is revealed as 3.42 Hz, shown by the -0.5π radians crossing of the phase taken from the LVDT response. This data proves extremely useful for modeling the system, resulting in better development of the controller designs discussed in Chapter IV.

2. Vertical Support Post

Section II.C.5 theoretically calculated the fundamental bending modes of vertical support post and a single sprung mass cross-member. The results from the cross-member justified the assumption that the other structural components can be assumed rigid, including the sprung and unsprung mass assemblies. The first bending mode for the vertical support post, however, was around 40 Hz, much closer to the frequency bandwidth of the proposed controller. In actuality, the first bending mode should be higher due to the motion constraints imposed by the bearing guides' influence.

Attaching the unsprung mass accelerometer to the end of the post, the same location opposite the accelerometer is tapped using the plastic end of a screwdriver. The FFT of the accelerometer signal was calculated in the same manner as before, yielding a

resonant peak at 29 Hz, 11 Hz lower than predicted. Because this motion could affect the output of the sensors, the magnitude of the controller needs to attenuate this frequency and above. This should not be a problem, though, given the low bandwidth desired. The design of this controller is discussed in the next chapter.

IV. CONTROLLER DESIGN

The results presented in the previous section provide system parameters that allow for more accurate modeling, and thus controllers to be designed with minimal error. The following section discusses the mathematic model built to characterize the experimental setup and the methods for designing the control functions driving the desired system responses.

A. Experimental Test Rig Model

In order to facilitate effective controller design, the actual system must be modeled as accurately as possible. Figure IV-1 graphically depicts the experimental test rig, from which the governing equations of motion are developed below.

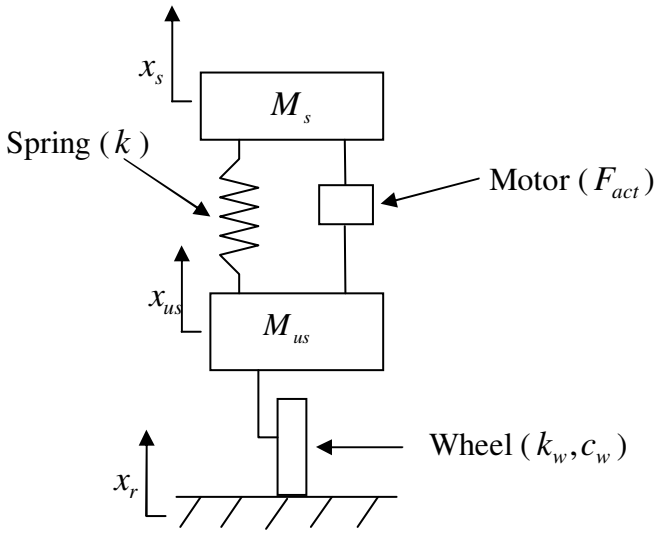

Figure IV-1 Graphic model of quarter-car test rig

$$M_s \ddot{x}_s + k\left(x_s - x_{us}\right) = F_{act} \tag{4-1}$$

$$M_{us} \ddot{x}_{us} + k\left(x_{us} - x_s\right) + k_w\left(x_{us} - x_r\right) + c_w\left(\dot{x}_{us} - \dot{x}_r\right) = -F_{act} \tag{4-2}$$

The motion of the sprung mass (M_s) is represented in (4-1), with spring force proportional to its deflection by a spring constant k and an actuation force (F_{act}) supplied by the motor. The same spring force and F_{act} act on the unsprung mass (M_{us}), exemplified in (4-2), although their loading is in opposite direction compared to the sprung mass. Additionally, forces imposed on the unsprung mass by the wheel are included, modeled by the spring constant k_w and viscous damping coefficient c_w.

Going further, these equations can be restructured into state-space form using the states of the model as proposed by [6], $\begin{bmatrix} \dot{x}_s & \dot{x}_{us} & x_s - x_{us} & x_{us} - x_r \end{bmatrix}^T$. The benefit of organizing the states as such is due to the type of motion sensing applied to the experimental test rig. Although the two accelerometers that monitor $\ddot{x}_s$ and $\ddot{x}_{us}$ can be integrated twice to provide the respective mass positions, much less error is inherent in feeding back the direct measurement of the LVDT that collects $x_s - x_{us}$. Further, it would be easier to incorporate a device to measure tire deflection ($x_{us} - x_r$) than to sense road disturbance x_r from a vehicular-mounted sensor.

In all, these equations can be rearranged, given the state vector definition, to generate a system of equations fashioned in the matrix form of (4-3) and (4-4).

$$\dot{\vec{x}} = A\vec{x} + Bu \tag{4-3}$$

$$y = C\vec{x} \tag{4-4}$$

Matrix *A*, *B*, and *C* are known as the state matrices, where *A* contains the coefficients connected to the states, *B* contains the coefficients pertaining to the input force (u), and *C* is a matrix that dictates the observed state(s) of the model. Formatting the governing equations of motion into that introduced by (4-3) yields the following.

$$\begin{bmatrix} \ddot{x}_s \\ \ddot{x}_{us} \\ \dot{x}_s - \dot{x}_{us} \\ \dot{x}_{us} - \dot{x}_r \end{bmatrix} = \begin{bmatrix} 0 & 0 & \frac{-k}{M_s} & 0 \\ 0 & \frac{-c_w}{M_{us}} & \frac{k}{M_{us}} & \frac{-k_w}{M_{us}} \\ 1 & -1 & 0 & 0 \\ 0 & 1 & 0 & 0 \end{bmatrix} \begin{bmatrix} \dot{x}_s \\ \dot{x}_{us} \\ x_s - x_{us} \\ x_{us} - x_r \end{bmatrix} + \begin{bmatrix} \frac{1}{M_s} \\ \frac{-1}{M_{us}} \\ 0 \\ 0 \end{bmatrix} F_{act} + \psi(\dot{x}_r) \tag{4-5}$$

$$\psi(\dot{x}_r) = \begin{bmatrix} 0 \\ 0 \\ 0 \\ -1 \end{bmatrix} \tag{4-6}$$

The equation shown in (4-6) appears because the entirety of (4-2) cannot be completely represented by the states. While this vector is important in simulating model response, it does not conveniently fit into the control design methodologies chosen in this development. Still, by placing the equation set in this format, controller analysis can effectively commence given matrices *A* and *B*.

Finally, all that is needed is a suitable output matrix (*C*) that will agree with what state is selected as the feedback.

B. Model-Based Control Design

This section discusses the control design methods centered on the use of the model presented in Section IV.A. First, however, the desired goals of these controllers must be realized. They are:

1) Provide the ability to respond successfully to a reference input to the system. Zero-error tracking is not necessary because position placement is not integral to operation and the system will naturally come to rest at equilibrium. .
2) Reject road disturbances to the sprung mass in the range of up to 10 Hz (20π rad/s).

3) Allow for sufficient phase margin (PM > 30°) to account for inaccuracies in the system model.
4) Attenuate responses of inputs to all frequencies above 50 Hz (100π rad/s), allowing for maximum decay while maintaining the phase margin requirement.

The above guidelines govern the designs of both state-space and classical control. Figure IV-2 displays the limitations imposed by the above on an open-loop-frequency-response plot, dictated by the loop-shaping technique given in [23].

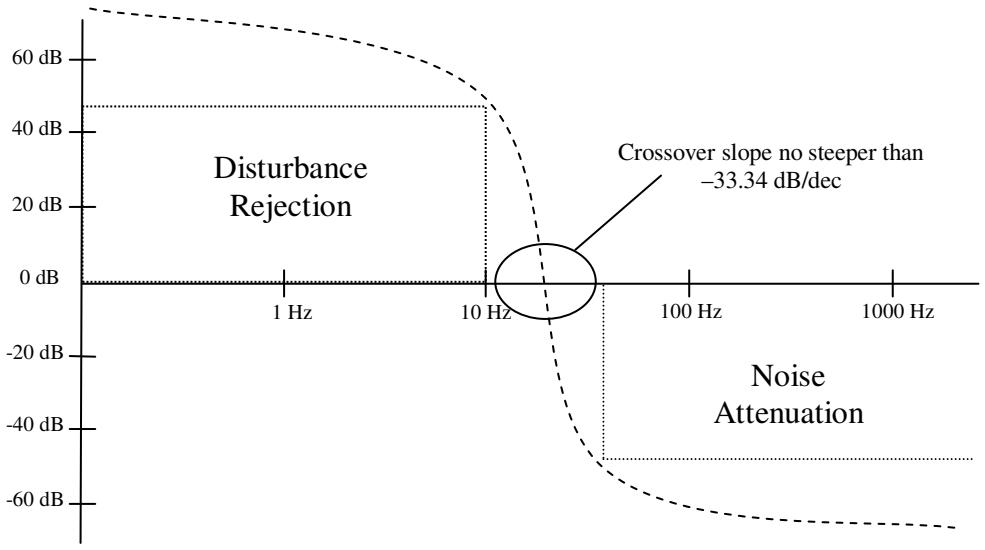

Figure IV-2 Design considerations reflected on open-loop-frequency-response plot

The system that generates these open loop characteristics are then implemented in negative unity feedback, displayed in Figure IV-3.

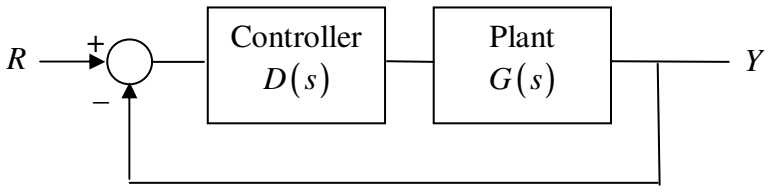

Figure IV-3 General closed-loop unity feedback block diagram

Generally speaking, the dynamics of the system are now governed by a new transfer function that combines the Controller and Plant (characterized by the response in Figure IV-2), in which the input is a difference from the system output, *Y*, and the designated reference input, *R*. Working through the mathematics, the closed-loop transfer function from the above block diagram turns out to be

$$\frac{Y(s)}{R(s)} = \frac{D(s)G(s)}{1 + D(s)G(s)} \tag{4-7}$$

Additionally, the closed-loop characteristic equation (which contains the closed-loop poles) of the system is equivalent to the denominator of (4-7), or

$$L(s) = 1 + D(s)G(s) \tag{4-8}$$

The closed-loop characteristic equation is vital in determining stability of the system, as all roots of $L(s)$ must have a negative real part to ensure stability. All control design methods presented are validated via limitations afforded by the closed-loop characteristic equation maintaining robust negative roots for all modeled and unknown system characteristics.

1. Open-Loop Constraints Determination

In order to apply the constraints given above, one must reveal the numeric values at which to design around. The first step is identifying a suitable substitute for *s* that relates the Laplace transform to frequency domain calculations. This substitution is defined as

$$s = j\omega \tag{4-9}$$

The representation of (4-9) denotes the substitution of variables in the Laplace domain that allows for frequency-based calculations to occur in the real-imaginary plane.

Useful in determining the magnitude of disturbance rejection required in Figure IV-2 is considering the maximum allowable error to an input, described as a sum of sinusoids over a bound range as described in [23]. To exemplify this method, the rejection range for inputs of unity sinusoids is bound to $0 \leq \omega \leq 20\pi$ rad/s. The closed-loop error to a reference input is defined as the following transfer function in the Laplace domain:

$$S(j\omega) \equiv \frac{1}{1 + D(j\omega)G(j\omega)} \tag{4-10}$$

with $D(j\omega)$ and $G(j\omega)$ representing the controller and plant transfer functions, respectively. Further, the error is a multiplication of the sensitivity and the reference input to the system, *R*, as shown in (4-11).

$$E(j\omega) = S(j\omega)R \tag{4-11}$$

For low-frequency disturbance rejection, the sensitivity is dictated by the high gains of the controller and plant portion, and can be approximated to

$$|S| \approx \frac{1}{|DG|} \tag{4-12}$$

Further, as the sensitivity is a relation of bound error output (e_b) to reference input (R), it can be equated to (4-13)

$$\frac{1}{W_1} = \frac{|e_b|}{|R|} \tag{4-13}$$

Since the error has been defined bounded (and the plant transfer function has no unstable poles), the error equation can be reduced to

$$\left|DG\right| \geq W_1 \tag{4-14}$$

Thus, by establishing W_1 as the lower-bound for the open-loop low-frequency response, the prescribed disturbance rejection bound by the arbitrary bound error selection.

Likewise, the upper-bound for high frequency attenuation can be assigned for open-loop design. Given the unknowns that occur in the model due to introduced noise effects and the lack of interest in controlling at these frequencies, it is beneficial to remove their effects as best as possible. The unknown plant transfer function including all nuances can be equated to be

$$G(j\omega) = G_0(j\omega) + \left|G(\omega) - G_0(\omega)\right|\Delta(j\omega) \tag{4-15}$$

as in [23], with *G* representing the unknown plant and G_0 denoting the modeled plant transfer function. Additionally, the high frequency error is separated into a magnitude and phase error. The latter is denoted in (4-15) as $\Delta(j\omega)$ and has a magnitude in the range of $0 \leq \left|\Delta\right| \leq 1$. Through rearrangement, Franklin, et al. arrived at the following [23]:

$$\left|TW_2\Delta\right| < 1 \tag{4-16}$$

The inequality of (4-16) places a maximum bound on the magnitude of the complementary sensitivity function (*T*) multiplied by an assigned uncertainty in the plant ($W_2\Delta$). Due to $\left|\Delta\right|$ having a maximum value of 1, it can be removed, leaving only *T* and W_2 which are shown below.

$$T \equiv \frac{D(j\omega)G_0(j\omega)}{1 + D(j\omega)G_0(j\omega)} \tag{4-17}$$

$$W_2 = \left| \frac{G - G_0}{G} \right| \tag{4-18}$$

Thus, W_2 is the value consider when minimizing the high-frequency responses. Relating to open-loop design, (4-19) places this constraint in context.

$$\left| DG_0 \right| < \frac{1}{W_2} \tag{4-19}$$

To meet the phase margin requirement selected, the slope at the crossover point must be no steeper than –1.667, or –33.34 dB/dec. Knowing this, the validity of choosing the specified attenuation frequency can be addressed. With the imposed limitations developed above, the minimum frequency that will be fully attenuated is calculated through

$$\frac{\log(W_1) - \log(W_2)}{\log(\omega_1) - \log(\omega_2)} = -1.667 \tag{4-20}$$

By arbitrarily setting $W_1 = W_2 = 200$ for excellent disturbance rejection and noise attenuation, one can calculate that or ω_2 must be at minimum 11494π rad/s (5747 Hz), which would leave a large frequency band of uncertainty and noise. Thus, these values are tailored to allow for optimum performance in both categories using the immovable constants relating to low-band design frequency and the phase-margin slope limitation.

2. Classical (Lead-Lag) Control Design

Classical design begins with converting the equations of motion to a Single Input, Single Output (SISO) transfer function in the S-domain, using the Laplace transformation. Choosing the plant input as F_{act} and the output as $\dot{x}_s$, the transfer function appears as in (4-21).

$$\frac{\dot{x}_s}{F_{act}} = \frac{s\left\{\left[M_{us}\right]s^2 + \left[c_w\right]s + k_w\right\}}{\left[M_s M_{us}\right]s^4 + \left[M_s c_w\right]s^3 + \left[k\left(M_s + M_{us}\right) + M_s k_w\right] + \left[c_w k\right]s + 2k^2 + k_w k} \tag{4-21}$$

Inputting the values determined in Chapters II and III, the open loop Bode plot is constructed in Figure IV-4, showing the inherent gain and phase margins.

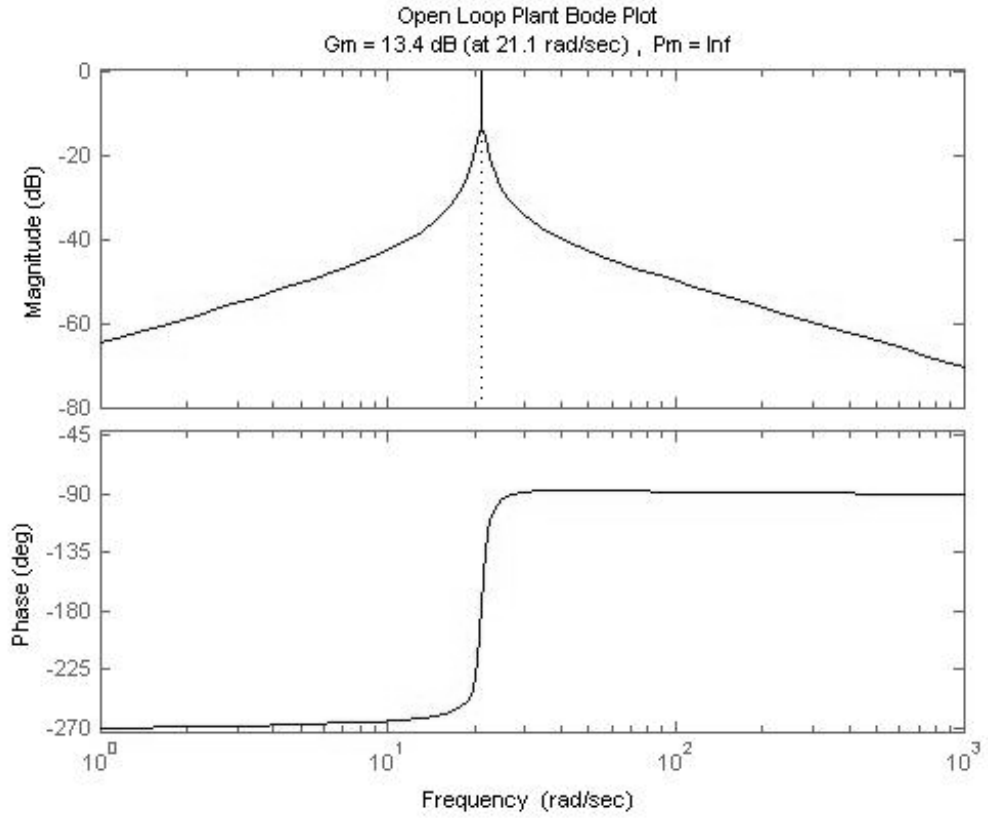

Figure IV-4 Open Loop Plant Response Bode Plot

The lack of damping between the sprung an unsprung masses leads to the large resonance at 21.1 rad/s (3.36 Hz). The inexact replication of the natural frequency extracted in Section III.C.1 exemplifies the modeling errors present, so sufficient phase margin must be present to ensure stability. When comparing this to the plot depicted in Figure IV-2, the plant is effective at high frequency attenuation, yet rejection of

disturbances in the lower frequencies (as experienced in driving conditions) needs much attention.

The next step is to design a controller capable of achieving the goals set forth. Although there are several control schemes available, a lead-lag network is chosen due to both its straightforward method in applying the necessary gain to the low-frequency band as well as adjusting for proper phase margin to allow for stability robustness. Proportional-Integral-Derivative (PID) control was also looked into, but results were not as desired.

Principally, to increase the gains important for disturbance rejection, the shape of the low-frequency bandwidth must be adjusted by introducing lag compensation. Initially, the low-frequency shaping was to be inclusive of all frequencies less than 10 Hz through addition of free integrators. This, however, was decided against due to the plant zero located at $s = 0$ rad/s. While acceptable for modeling purposes, any errors around that zero location would cause ineffective closed-loop pole location if, say, the actual location of that zero was in the right half plane. Alternatively, as the goal of this controller is not to provide steady-state convergence, it was decided that a low-frequency cutoff would be acceptable below 1 rad/s (given that the exciting acceleration is a function of ω). Effectively, this is the location chosen for the lag-compensation pole. Conversely, in order to minimize the induced increase (and isolate the adverse phase shift) in the low-frequency bandwidth, the lag-compensator zero is placed at $\omega = 5$ rad/s, before the plant resonance.

While lag compensation is essential in shaping the plant response, it is not enough. Thus, lead compensation is added at slightly higher frequencies to shape the portion of desired disturbance rejection where the plant response rolls off, i.e. the plot slope becomes negative. Naturally, the ideal location for the upper corner frequency (the lead zero) is around the spot where the plant response fully develops its negative slope. Consequently, this also will increase the desired rejection range, so the choice is to place the lead zero such that minimization of this said increase will occur. Initially, this location is chosen to be ~50 rad/s, with the lead pole placed at 100 rad/s to force attenuation above this frequency.

To further drive high-frequency attenuation, another pole is place at 100 rad/s, increasing the rate of decay. Thus, the initial control transfer function $\hat{D}(s)$ is set at

$$\hat{D}(s) = K\frac{(s+5)(s+50)}{(s+1)(s+100)^2} \tag{4-22}$$

with the control gain *K* to be adjusted, allowing proper loop placement at the desired magnitude. This is done with ease using the *SISOTOOL* Graphic User Interface (GUI) in Matlab®, which activates in interactive design layout portrayed in Figure IV-5.

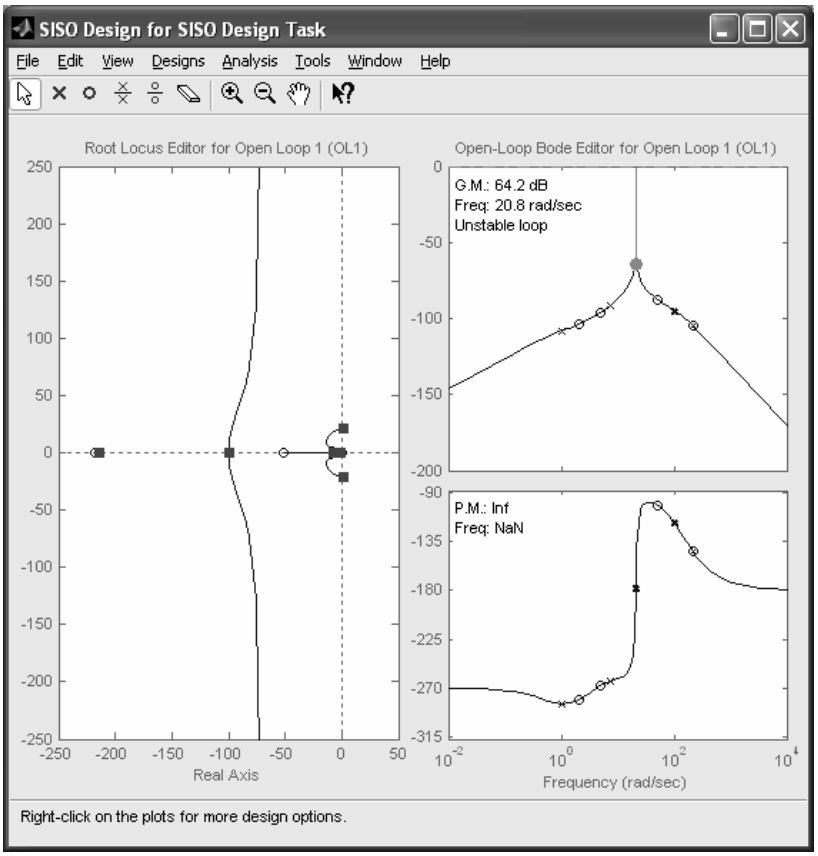

Figure IV-5 *SISOTOOL* GUI used to interactively shape the open-loop transfer function

With this tool, pole-zero locations and loop gains can be easily adjusted with quick confirmation of their effect on the open loop stability. Loaded in the *SISOTOOL* GUI at

the time of capture in Figure IV-5 is the Loop Transfer function with unity gain *K*. The goal is to increase this gain until the disturbance rejection bandwidth is sufficient with an adequate PM, dictated in the lower right screen. After some tuning, the optimal controller is settled at the transfer function given in (4-23).

$$D(s) = 103600\frac{(s+5)(s+51)}{(s+1)(s+100)^2} \tag{4-23}$$

Following this lead-lag addition, the compensated (*DG*) open-loop bode plot is shown in Figure IV-6.

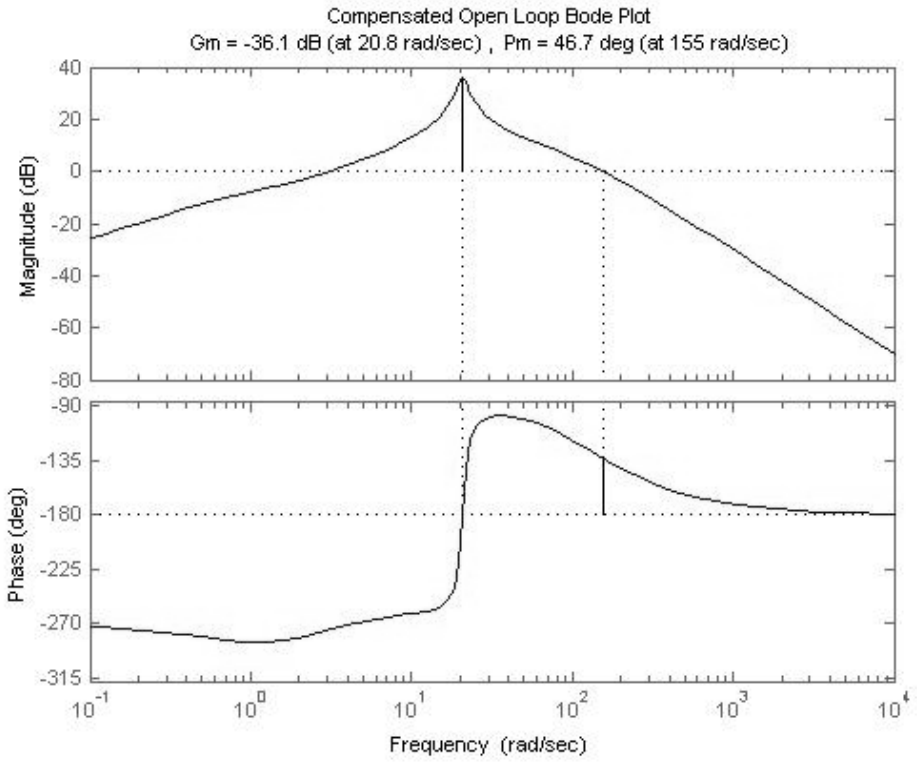

Figure IV-6 Compensated open-loop Bode plot

As mentioned, the low frequency bandwidth resembles more of a band-pass filter, with lower corner frequency of ~3 rad/s and crossover frequency of 155 rad/s. For the range in between $8 \le \omega \le 63$ rad/s, the error magnitude $\left|E(j\omega)\right|$, as defined in (4-11) is less than 0.1 for unity input, while high frequency attenuation asymptotically decreases at

a rate of –40 dB/dec while still maintaining suitable a PM of 46.7°. Although not explicitly mentioned during this development, another critical factor in successful control is the actual control force that can be exerted and the effects of the system nuances that cause response differing from expected. Therefore, while the poles are adequately selected, the gain may need additional tuning when implemented in the actual system.

3. State-space Control Design

Previously, a classical control design resulting in a lead-lag compensator was introduced. To complement the established controller, a design implementing the state matrices *A* and *B* as developed in (4-5) (with *C* to be determined below), is presented.

The first step is to select a proper state output vector *C* such that the system can be defined observable. This is done through the observability test of an arbitrary selection of *C* via (4-24), displayed in [23].

$$O = \begin{bmatrix} C \\ CA \\ CA^2 \\ CA^3 \end{bmatrix} \tag{4-24}$$

The resulting observability matrix *O* must be nonsingular to define a system that is observable, driven by proper selection of *C*. As expected, by selecting the output state $\dot{x}_s$, the criteria set forth by the observability matrix are met, and the resulting *C* vector can be expressed as in (4-25).

$$C = \begin{bmatrix} 1 & 0 & 0 & 0 \end{bmatrix} \tag{4-25}$$

The block diagram analogous to Figure IV-3 for state-space systems, showing control with full state feedback, is shown in Figure IV-7

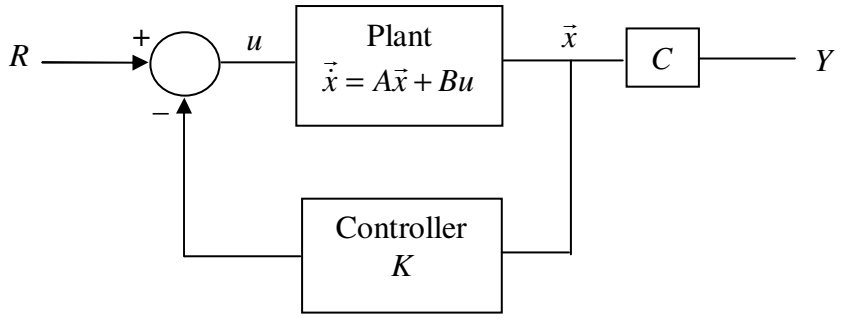

Figure IV-7 Closed-loop block diagram with full-state feedback

While, mathematically, classical control responses are calculated in the Laplace domain, state-space control responses are done in the time domain through (generally by methods of numerical integration) solving the *n* first-order equations. From Figure IV-7, the control input *u* to the plant is equivalent to

$$u = R - K\vec{x} \tag{4-26}$$

where *K* is the control gain vector given in (4-27), with values to be determined.

$$K = \begin{bmatrix} K_1 & K_2 & K_3 & K_4 \end{bmatrix} \tag{4-27}$$

For this assessment, the reference input is chosen as the constant 0 which, when substituted into (4-3), yields

$$\dot{\vec{x}} = \left(A - BK\right)\vec{x} \tag{4-28}$$

Although implementation of the state-space control law is different from classical control design, the methods for design are still conducted in the Laplace domain. Therefore, defining the closed loop characteristic equation, (4-29), and ultimately finding the solution to its roots from (4-30) is of utmost importance.

$$L = \left[sI - \left(A - BK \right) \right] \tag{4-29}$$

$$\det\left[sI - \left(A - BK \right) \right] = 0 \tag{4-30}$$

Quite simply, the path forward is to select poles that the system should ideally exhibit. Explicitly, the idea is to shape the open loop transfer function to resemble that of Figure IV-2. In this instance, it was chosen to shape the system to act as a dominant second-order system with good damping characteristics and force the two supplemental poles to a range sufficient to attenuate the high frequency dynamics of the closed-loop system. With the attenuation goal set forth in Section IV.B.1, the supplemental poles are arbitrarily placed at $s = -100$ rad/s.

While placing the two dominant second-order poles on the real axis would be ideal, given that critical damping would be achieved (i.e. the damping ratio ζ would be 1), it would require a larger amount of control force. Knowing that the low-frequency disturbance band extends to 20π rad/s, the real part of the dominant poles is selected to be –60 rad/s. Through trial-and-error of simulation presented in Chapter V it was settled, based on a balance of control force input and response magnitude, that the dominant poles would be set as an imaginary pair at $s = -60 \pm 5j$ rad/s. The resulting damping ratio of the dominant poles is $\zeta = .995$, as calculated by [23] using (4-31).

$$\zeta = \sin^{-1}\left[\tan\left(\frac{\mathrm{Im}\left[p(j\omega) \right]}{\mathrm{Re}\left[p(j\omega) \right]} \right) \right] \tag{4-31}$$

To ease the path in calculating the control law gains, Matlab®'s *acker* function plays the major role. Supplying this function the state matrices *A* and *B*, as well as the desired closed-loop poles, *acker* foregoes the mathematics outlined in [23] and returns the proper gains to satisfy the desired output of (4-32).

$$K = \left[-1280 \quad -610 \quad 25720 \quad -416920 \right] \tag{4-32}$$

By definition [23], having all poles in the left-half plane (LHP) of the *s*-plane, the system is declared stable. Unlike classically designed control, however, the control law has no effect on the open-loop zeros of the system. Therefore, instability can arise by not accounting for the phase shifts associated with these zeroes. A remedy to this is to install an overall gain adjustment to align the crossover frequency with a suitable phase margin. Through trial-and-error graphical comparisons using the simulation in Chapter V the overall gain that brings stability to the system is

$$K_c = 0.01 \tag{4-33}$$

By selecting the above gain, the individual gains in vector K are adjusted to provide stable disturbance rejection/noise attenuation under constraints exhibited by control force saturation, as in the classical controller designed in Section IV.B.2.

V. REFERENCE INPUT ASSIGNMENT AND SOFTWARE SIMULATION OF CONTROL DESIGNS

In this section, the reference input discussed in Chapter IV will be established; and from this, simulations that gauge the designed controllers' effectiveness in tracking this reference will ensue.

A. Reference Input Assignment

The goal of these controllers, as discussed in Chapter IV, is to track an assigned reference input. According to Gobbi, et al. [18], the optimum control algorithm is to simulate the sprung mass motion as if there was a damper fixed to it and an inertial frame as shown in Figure V-1 (for a general passive quarter-car model), otherwise known as inertial-frame damping in this text.

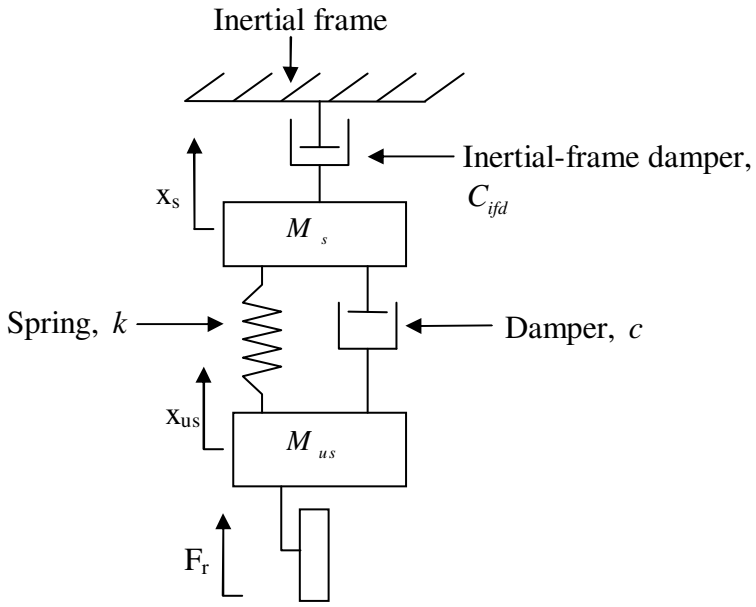

Figure V-1 Inertial-frame damping diagram

Building off this knowledge, a reference input is constructed from that of (5-1) and (5-2) which govern the dynamics of the system, using C_{ifd} to represent the inertial-frame damping (IFD) coefficient.

$$M\ddot{x}_s + k\left(x_s - x_{us}\right) + c\left(\dot{x}_s - \dot{x}_{us}\right) = -C_{ifd}\left(\dot{x}_s\right) \tag{5-1}$$

$$M\ddot{x}_{us} + k\left(x_{us} - x_s\right) + c\left(\dot{x}_{us} - \dot{x}_s\right) = F_r \tag{5-2}$$

Since sprung mass dynamics are of principal concern, (5-1) contains the relationships to dictate the reference velocity the controller intends to track. Relating to the model presented in Chapter IV, the inertial-frame damping reference input simplifies to

$$\dot{x}_{s.ref} = -\frac{M_s\ddot{x}_s + k\left(x_s - x_{us}\right)}{C_{ifd}} \tag{5-3}$$

By feeding sprung mass acceleration and the LVDT signals, the above trajectory is quite easily constructed.

The other reference input of interest is that when $C_{ifd} \to \infty$, or the reference velocity goes to zero. This zero reference is applied as well to the simulations and experimental validations in the same manner as the IFD reference input.

B. Software Simulation

As mentioned in the control design for both classical and state-space methods, the plant model was forced to exclude the disturbance input of the road (x_r). Modeling errors, such as this, are reason for response simulation in a software algorithm before implementation in the actual system. Additionally, the robustness of the controller can be tested, as well as monitoring of how large the theoretical control force will be under trying situations.

For all the controllers presented, the supplemental design methodology is to choose disturbance frequencies and simulate the system response. Not only does this increase the likelihood of the controllers' robustness, it provides verification for the state-space and adaptive designs, both of which did not have Bode plots display expected responses. Also, exact modeling of the tire's characteristics was not obtained, so the robustness of the controllers is also tested with ability to respond appropriately with various tire damping values. Another observation important in assuring effectiveness is that of expected control force to be supplied by the motor. It is important to keep this force below 50 N to avoid saturation instabilities.

Matlab®'s Simulink® interface provides an excellent platform in which easy layout and rapid simulation are allowed. Overall, the graphic program used to simulate such plant responses are broken down into a constants-declaration block, plant simulation block, and controller section. The complete layout is displayed in Appendix I.

1. Description of Simulation Program Subsets

Beginning, the plant model is drawn to exactly replicate the governing equations of motion dictated in Section IV.A. The plant function receives all inputs of necessary states, disturbance inputs, control force, and constants and outputs the accelerations of the two masses. These accelerations are, in turn, integrated to provide the input states to the system and controllers. As implied, the disturbance input (arbitrarily defined by the user) is fed into the road position (x_r). All simulations utilize the same sinusoidal disturbance with amplitude of 0.0127 m, equivalent to the sine disturbance of the test rig. Appendix I.A isolates this section of the overall simulation program by showing input-output connections and examining the internal connections that govern the block's output.

The 'Constants' block from Appendix I contains the block where the declaration of all plant parameters is located. These are changed to reflect misrepresentations of the model when the values were selected, ultimately allowing the robustness of the controller to be tested under changes to the plant. Except where noted, all constants set are those used in designing the controllers.

In the controllers section, the multiple control blocks are amassed with inputs of reference and states that are fed back, and outputs to the control force input "u." Tuning these with respect to simulated plant responses is done through the addition of a gain-adjustment block preceding the designed controller in Appendix I.B. Algorithms that develop the reference tracking signals are generated in Appendix I.D.

Throughout the simulation program, there are signal lines branching off that lead to "Scope" blocks. These are to monitor real-time during the simulation what the signal is doing. Using these outputs, the controller gain is tuned to optimize the response via adjustment of the included controller gains. These adjustments are discussed in-detail below.

2. Classical Controller Simulation

From the open-loop bode plot of the experimental test rig model, the maximum amplitude of the uncompensated system will occur with an excitation frequency of around 21 rad/s. Figure V-2 shows the response for a chosen simulation frequency of ω equaling 20.5 rad/s.

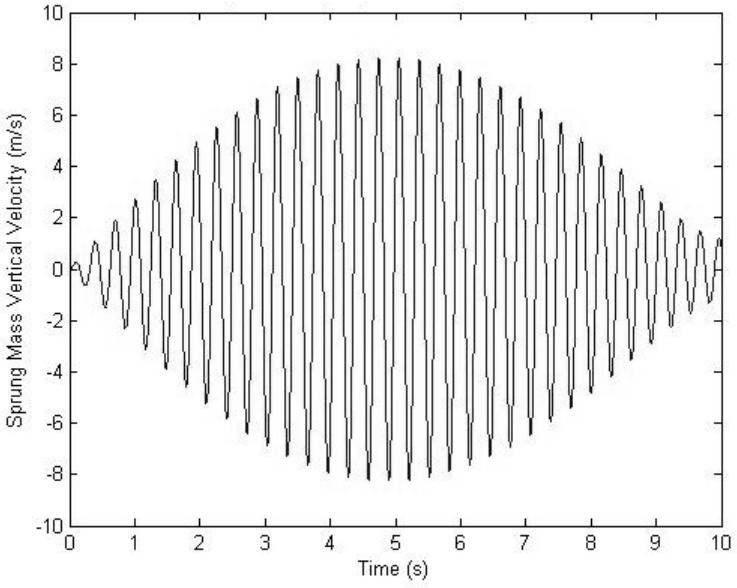

Figure V-2 Uncompensated system response at ω=20.5rad/s

The beating phenomenon exhibited in Figure V-2 that causes the response to periodically grow and decay is due to the imperfect, however close, matching of the excitation frequency and the system's natural frequency. Excitation frequency that would have equaled the system's natural frequency would have caused continuous growth in the sprung mass response.

Beginning, the controller designed in the classical fashion is simulated using both references and varying tire damping. Referring to Section IV.B.2, the chosen controller transfer function is

$$D(s) = 103600 \frac{(s+5)(s+51)}{(s+1)(s+100)^2} \tag{5-4}$$

When adding this controller to the system for a zero reference input, the resulting response is shown in Figure V-3.

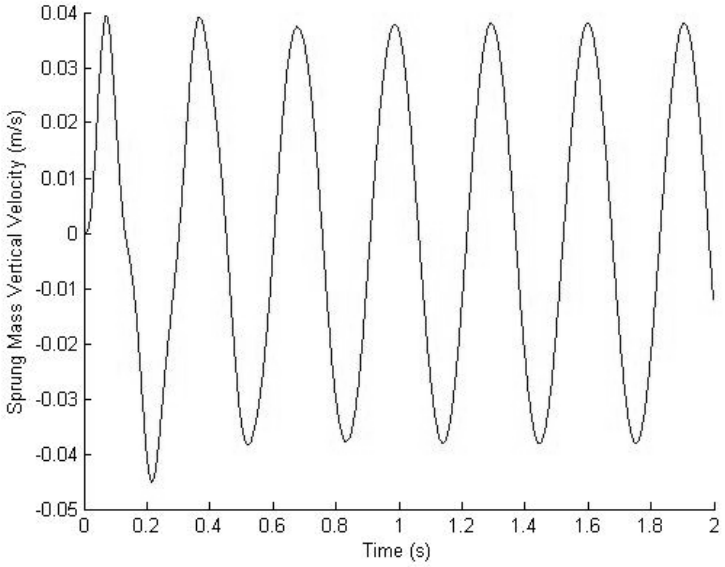

Figure V-3 Compensated response at 20.5 rad/s, using zero reference

Visibly, there is a considerable amount of disturbance rejection, as the maximum amplitude is attenuated to 0.5% of its uncompensated value. The corresponding control force applied via simulation is shown in Figure V-4.

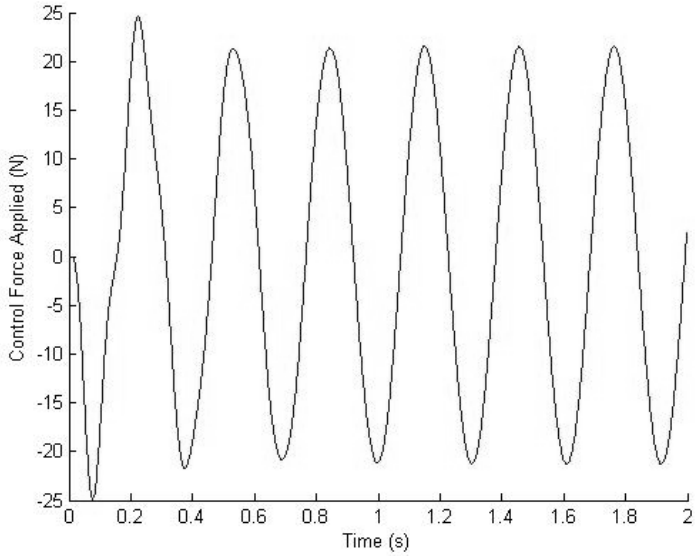

Figure V-4 Control force output at 20.5 rad/s, using zero reference

As explained, varying the tire's stiffness is a good way at testing the controller's robustness due to its ability to compensate for the shift in resonance.

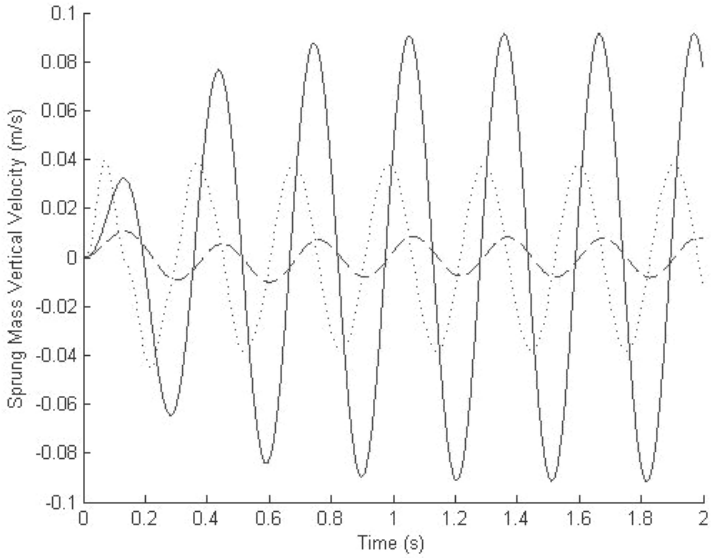

Figure V-5 Compensated response at 20.5 rad/s for tire stiffness values of 100 N/m (dashed), 1000 N/m (solid), and 10000 N/m (dotted), using zero reference

Additionally, as tire stiffness is a function of multiple parameters that can change dramatically under different driving conditions. Figure V-5 overlays plots for damping values of 100 N/m (dashed line), 1000 N/m (solid line), and 10000 N/m (dotted line).

The above graph shows that tire stiffness greatly affects the tracking error, but the controller is able to maintain bounded output of a fairly low magnitude. This exhibition of robustness confirms that, around this frequency, the system will be able to behave as hoped. However, when the two resonant frequencies move closer together (1000 N/m tire stiffness), more control force is required to reject input disturbances. Figure V-6 displays this applied force for the varying tire stiffnesses.

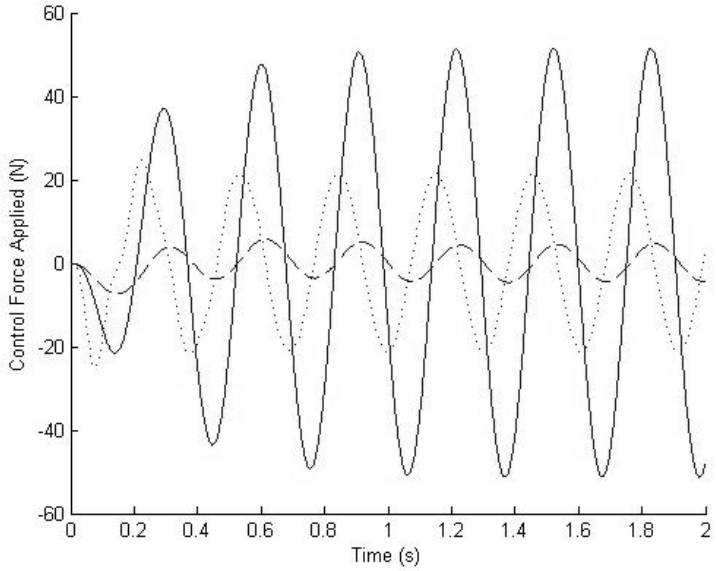

Figure V-6 Control Force applied at 20.5 rad/s for tire stiffness values of 100 N/m (dashed), 1000 N/m (solid), and 10000 N/m (dotted), using zero reference

Controller performance is not as desired, however, at the higher end of the disturbance-rejection band. As an example, only about 20% of the disturbance is rejected at a simulated road disturbance of 50 rad/s, which is plotted in Figure V-7.

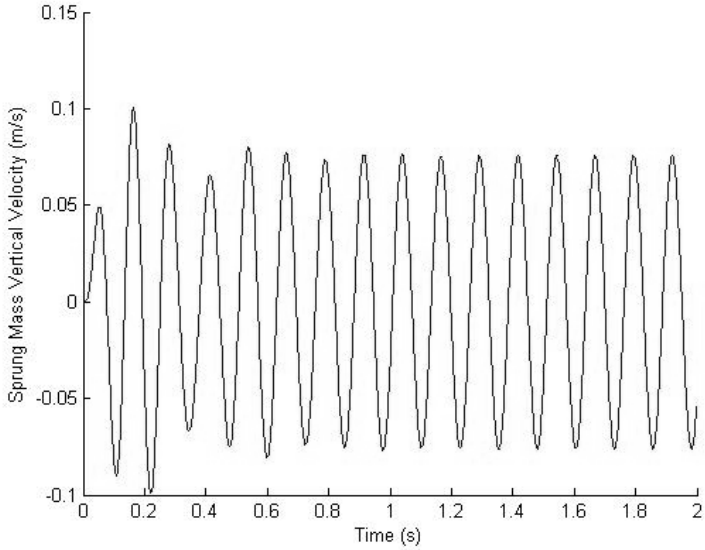

Figure V-7 Compensated response at 50 rad/s, using zero reference

With the control force approaching its upper limit, evidenced by the control force plot of Figure V-8, the controller would benefit little from tuning to expand the rejection band. Only by increasing the force capacity of the motor would a tunable solution present itself.

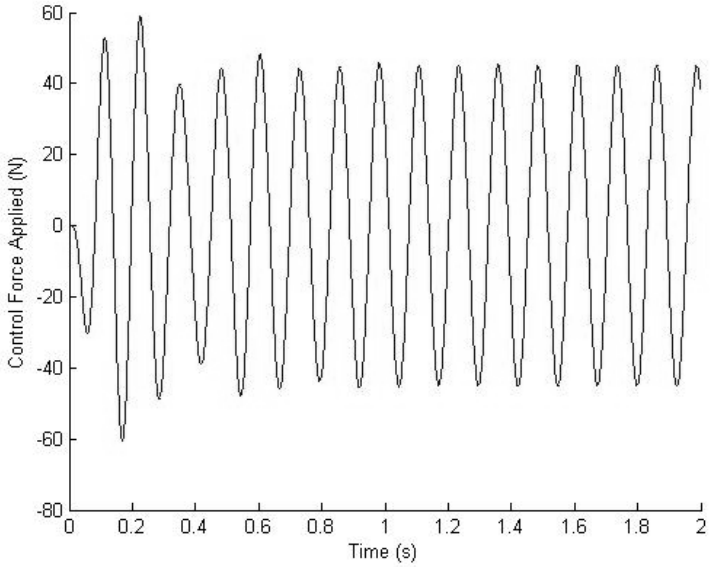

Figure V-8 Control force output at 50 rad/s, using zero reference

In the same fashion, simulation analysis of the compensated system continues using the inertial-frame damping reference input. Figure V-9 displays responses at 20.5 rad/s for varying IFD values of 100, 500, and 1000 N-s/m

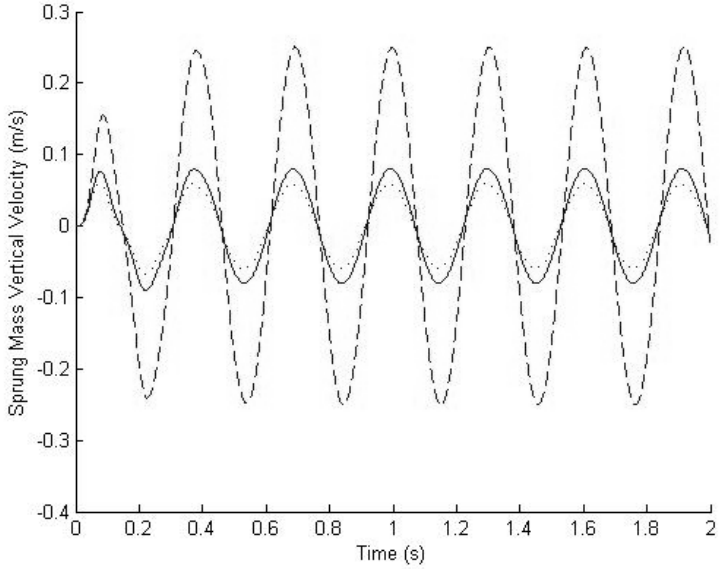

Figure V-9 Compensated response at 20.5 rad/s, using inertial-frame damping reference C_{ifd} = 100 N-s/m (dashed), 500 N-s/m (solid), 1000 N-s/m (dotted)

As expected, the increased inertial-frame damping drives the response to the limit $C_{ifd} = \infty$ N-s/m, or zero reference velocity input. Comparing the force outputs, not much difference is present at 20.5 rad/s, as evidenced by the contents of Figure V-10.

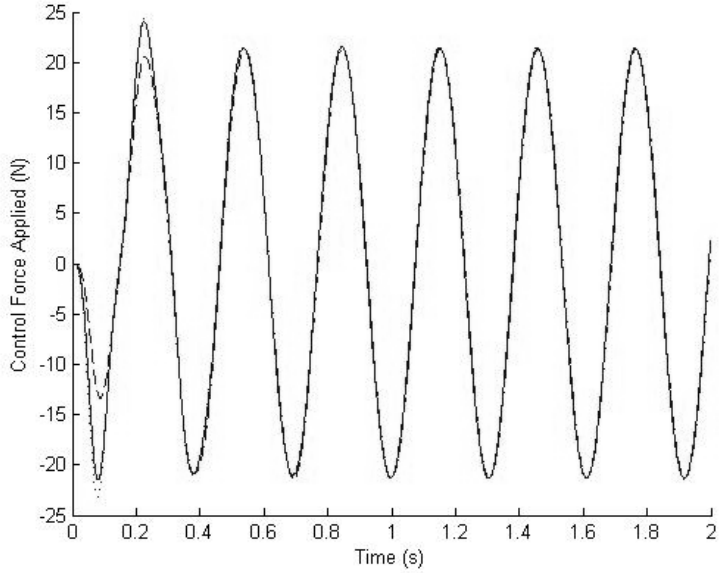

Figure V-10 Control force output at 20.5 rad/s, using inertial-frame damping reference C_{ifd} = 100 N-s/m (dashed), 500 N-s/m (solid), 1000 N-s/m (dotted)

Meanwhile, Figure V-11 and Figure V-12 display the compensated response and control force, respectively, of the simulated test rig at 50 rad/s.

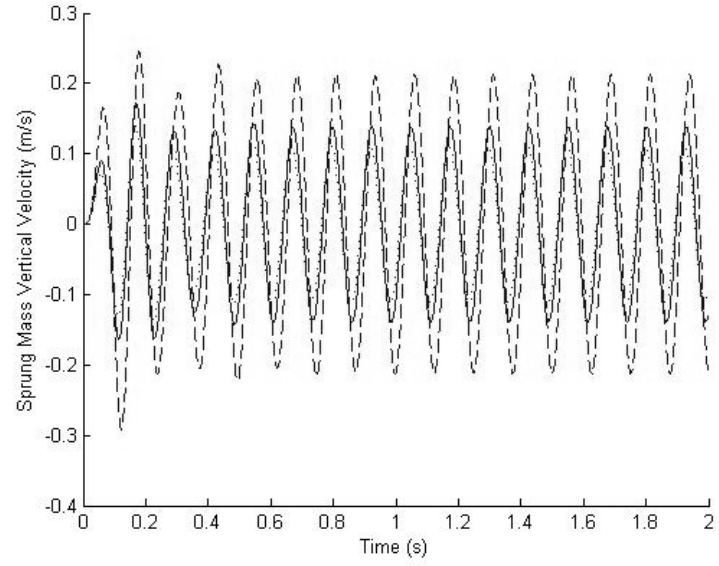

Figure V-11 Compensated response at 50 rad/s, using inertial-frame damping reference C_{ifd} = 100 N-s/m (dashed), 500 N-s/m (solid), 1000 N-s/m (dotted)

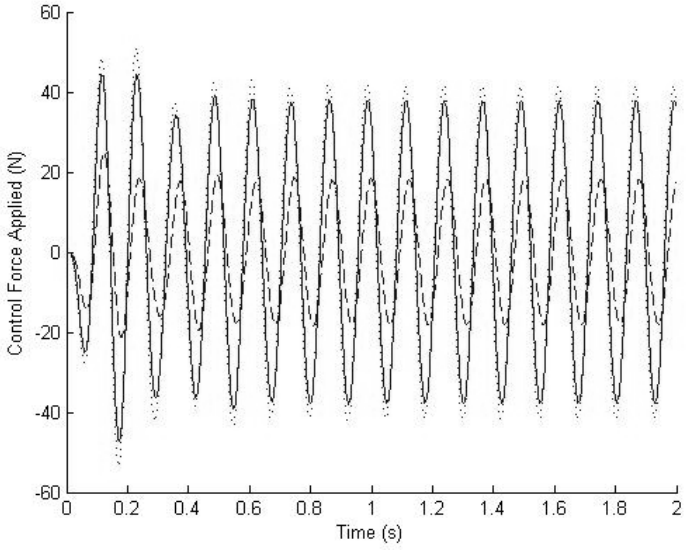

Figure V-12 Control force output at 50 rad/s, using inertial-frame damping reference C_{ifd} = 100 N-s/m (dashed), 500 N-s/m (solid), 1000 N-s/m (dotted)

Once again, these plots approach the zero-reference response as $C_{ifd} \to \infty$. Therefore, from a response-controlling point of view, simulations verify that the ideal reference is zero. However, for avoiding saturation or power-saving modes, using inertial-frame damping would be beneficial.

In all, simulations of the classical control response reveal that performance is admirable, and the controller design incorporates a fair margin for modeling errors. Application to the actual test rig in Chapter VII, however, will determine effectiveness in the setting of purpose.

3. State-space Simulation

Similar to the classical controller analysis, simulation continues through testing the capabilities of the state-space control. Recall from IV.A, the controller gains applied to the four states $\begin{bmatrix} \dot{x}_s & \dot{x}_{us} & x_s - x_{us} & x_{us} - x_r \end{bmatrix}^T$ are

$$K = \begin{bmatrix} -1280 & -610 & 25720 & -416920 \end{bmatrix} \tag{5-5}$$

The plot of compensated response (Figure V-13) reveals terribly divergent behavior, showing the controller's inability to accommodate the change in plant design from its state-space model.

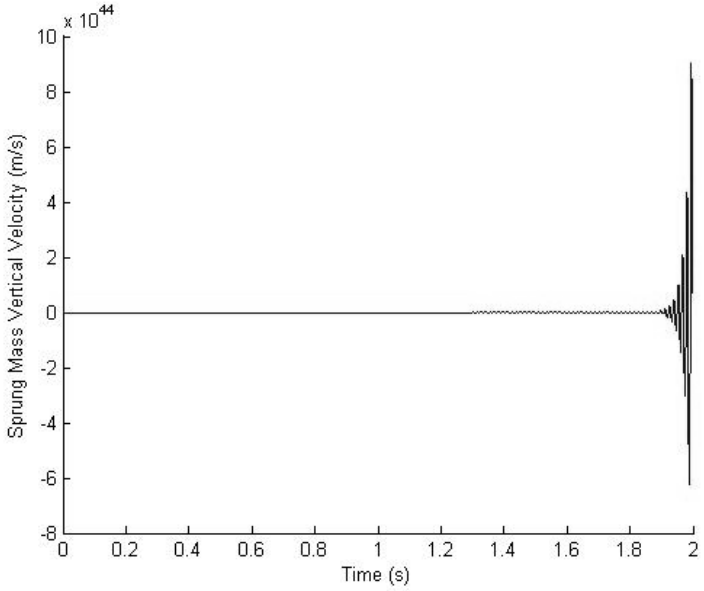

Figure V-13 State-space compensated response at 20.5 rad/s, using zero reference

The difficulty, as expressed in Section IV.B.3, is no analogue to the classical control open-loop Bode plot was done to establish margins of robustness. Therefore, the chosen tuning method is to adjust a lead gain factor that would effectively change the crossover frequency and introduce a stable phase margin to the system. One necessary drawback, though, is that the disturbance rejection abilities will be lessened. After trial and error, the most effective gain factor is $K_c = 0.01$ with positive feedback. However, this addition is still not enough. Evidence that the controller does not adjust well to the more representative simulation model (compared to the state-space counterpart), is the controller cannot maintain a bounded output when tire deflection is fed back. Substituting 0 for this remedies the issue, and is considered acceptable given the relatively small displacements encountered. Adapting all of the above into the state-

space algorithm, the refined response to the 20.5 rad/s disturbance is now displayed in Figure V-14.

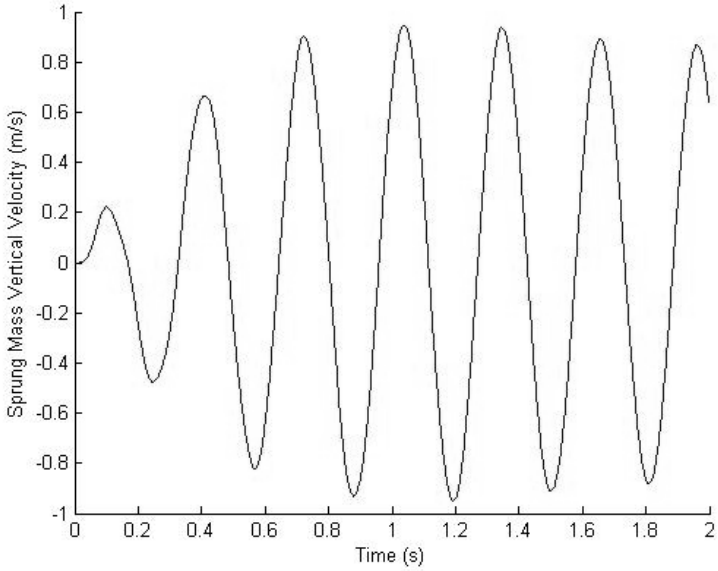

Figure V-14 State-space compensated response at 20.5 rad/s, using zero reference

As exhibited by the above plot, the designed state space controller is not nearly as effective as its classical counterpart as it is only able to reject the disturbance to ~10%.

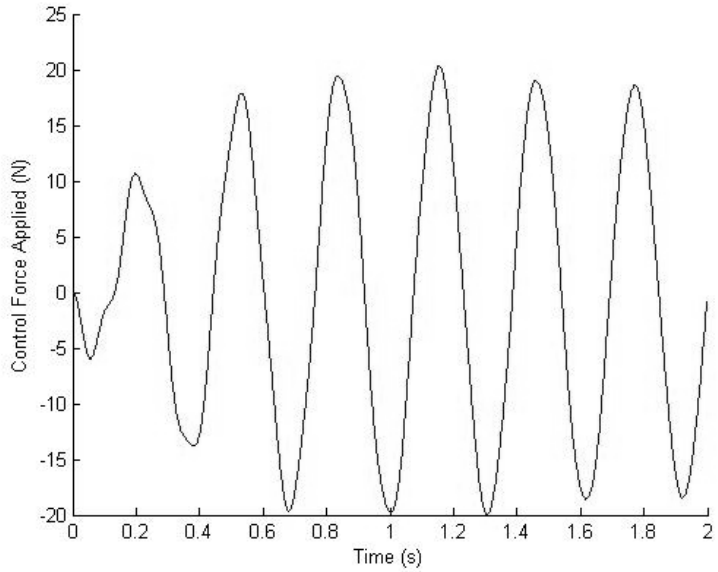

Figure V-15 State-space control force applied at 20.5 rad/s, using zero reference

Corresponding, the required control force (Figure V-15) is less than that needed by the classical controller, however not nearly the decrease expected with over 100 times the compensated response!

Higher frequency attenuation is noticeably better, however, as demonstrated by the output in Figure V-16 (control force output in Figure V-17).

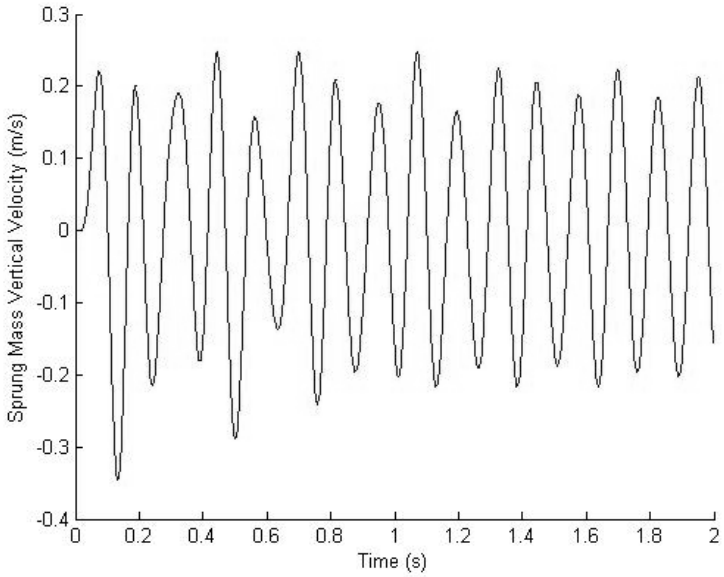

Figure V-16 State-space compensated response at 50 rad/s, using zero reference

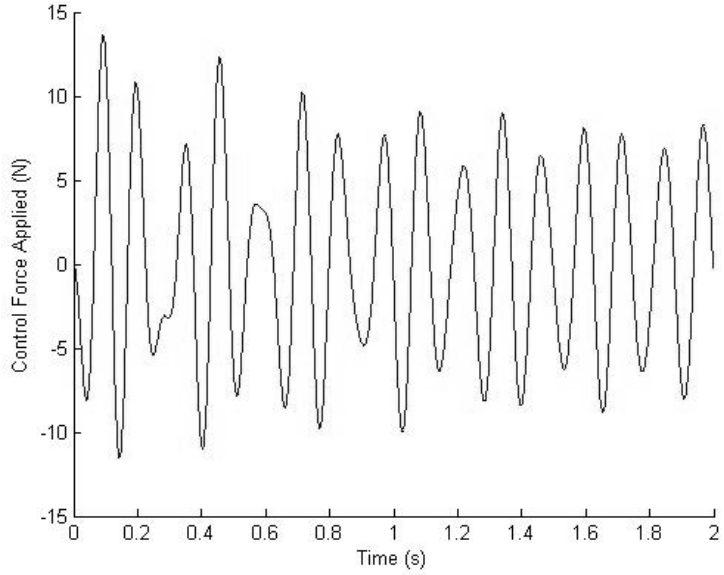

Figure V-17 State-space control force applied at 50 rad/s, using zero reference

As is shown by the inertial-frame damping demonstration with the classical controller, this reference allows for relaxation of control force requested, although at the expense of larger responses. The state-space controller requires no forces near the threshold, so no gains would present themselves with its implementation. Still, data from tracking a inertial-frame damping reference in reality is presented in Chapter VII.

Overall, the state-space controller performs satisfactorily, but not nearly as admirably as the classical controller. Simulation reveals that effects from not being able to include all information about the states in control design weighs heavy on instigating gross instability.

VI. EXPERIMENTAL SOFTWARE AND FILTER DESIGNS

Now that controller designs are rigorously simulated and approved for testing, it is time to prepare the program that drives the actual implementation. Constructed in Simulink®, the program is designed by the user to read the sensor inputs from the analog-to-digital (ADC) converters, apply the appropriate signal conditioning, and output the PWM amplifier signal through digital-to-analog (DAC) converters. This program is then compiled and loaded onto the dSPACE® DSP board. Communication between the controller and user is now fed through ControlDesk®, the graphic user interface (GUI) intimately connected with the board signals.

This section discusses the block diagram designed to load into dSPACE® and the user interface built for operator intervention. Continuing, a discussion of the method for filtering adverse noise from the incoming sensors is carried out in attempt to provide the best control performance possible.

A. Experimental Software Development

Although the method for designing the block diagram is the same as was done for the simulation code, different aspects are used, omitted and added. Specifically, there is no plant simulation because the control force is outputted to the actual system. Further, while the control force directly acted on the plant as such, this design must employ the three-phase decomposition presented in Section III.B.1 to drive current production from the PWM amplifiers. Appendix II displays signal routing on the macroscopic scale, with Appendix II.C containing the inertial-frame reference creation of the ‘ref_create’ block.

A noticeable difference can be found in the ‘controller’ block, the location of the state-space and classical controllers (Appendix II.B). A closer look at the classical control will reveal that is coded in discrete domain. The compiler that uploads the block diagram into dSPACE® cannot register continuous-time transfer functions. Thus, it is necessary to emulate the classical control as well as the sensor filters to their discrete-time equivalents.

Emulation is carried out via the modified matched pole zero procedure outlined in [23], where the following steps are taken:

1) Transform the *s*-domain poles to discrete time using the relationship

$$z = e^{sT} \tag{6-1}$$

where z is the discrete pole location and T is the sampling period of the data acquisition.

2) Add discrete time zeros at $z = -1$ until the degree of the numerator equals the degree of the denominator.
3) Set the discrete-time gain by selecting an arbitrary frequency for $s = j\omega$. Most often, for simplicity, this frequency is $s = 0$ rad/s. However, zeros and poles placed at 0 rad/s yield unusable results, and another frequency must be chosen.

Setting the sampling period $T = 0.001$ s, the controller of (4-21) from Section IV.B.2 is converted into its discrete time equivalent, shown below.

$$D(z) = K_D \frac{(z+1)(z-0.95)(z-0.995)}{(z-0.999)(z-0.9048)^2} \tag{6-2}$$

Instead of setting the controller gain via the third emulation step, during a pre-screening its value was adjusted to deliver the strongest resistance to manual movement while not losing stability. The gain block 'llgain' from the macroscopic block view (Appendix II) applies this to the control output. Likewise, the state-space gain was altered from –0.01 to –0.025 as shown in the 'ssgain' block of the same view.

Appendix II.D is an addition to the simulation program. Whereas the force acted directly on the plant, this algorithm must deliver signals to the detached PWM amplifiers which, in turn, generate actuation of the motor. Therefore, the force constant determined in Section III.B.2 acts as a gain, found in the '1/kf' block, to convert the force into an

equivalent motor current. Finally, the decomposition of this current into its three balance phases occurs and the ensuing output is shipped to the DAC blocks.

On the other end, all sensor signals are brought in through the 'daq' block of Appendix II.A, including the LVDT, accelerometers, and Hall switch. Speed is generated through the difference algorithm at the bottom, while accelerations and LVDT displacement signals are filtered and corrected for proper unit outputs before being manipulated into supplying state data.

B. Sensor Noise Analysis and Filter Design

Thus far, controllers have been designed and simulated with a model that presents ideal characteristics. While the model was slightly different than the simulated test rig, no external factors or errors were present. Sensor noise is commonplace in all electromechanical systems. While the controllers are designed to attenuate high frequency elements, other detrimental signals can be introduced. This section aims at filter design directed at removing the aforementioned problems.

Understanding the nature of sensor feedback is imperative in ensuring proper signals do not get filtered out by mistake. Particularly, at rest accelerometers should not supply a voltage where an LVDT should. Also, when no motion is present there should be no large magnitudes in a frequency plot. These are the main concerns when designing the upcoming filters.

1. LVDT Filter Design

The purpose of the LVDT, as presented in Section II.D.2, is to monitor the relative displacement between the unsprung and sprung masses. This signal is fed back in two locations: one is for the state-space control (recall the third state, $x_s - x_{us}$) and the other is to directly monitor the position of the motor shaft in relation to the coils.

The first step in conditioning the incoming signal from the DS1104 board is to establish the factor that converts position from the supplied ADC channel input. Instrumental in calibrating the LVDT was a digital optical scale from Sony Precision[10] capable of 1 μm resolution. For calibration, the LVDT is connected directly to the optical encoder and, with dSPACE® recording the outputs, the LVDT signal is plotted against the distance traveled by the encoder. A series of 10 trials were collected to yield a gain of 0.005137 m/V. The ADC voltage of ±10 V is rescaled in Simulink® to ±1, arbitrarily labeled as signal. Factoring this 10 V/signal correction with the LVDT gain, the resulting factor implemented in Simulink® is 0.05137 m/signal.

The chosen filter design is a second-order low pass transfer function with corner frequency set at ω_c = 160 rad/s and gain factor of 25600 to raise the magnitude to unity for low frequencies.

$$F_{LVDT}(s) = 25600\frac{1}{(s+160)^2} \tag{6-3}$$

The dSPACE® compiler, however, cannot recognize continuous-time transfer functions, so this was emulated to a discrete-time estimation using the modified matched pole-zero method using sampling period of T = 0.001 s. Equation (6-4) displays the transfer function that was used.

$$F_{LVDT}(z) = .005545\frac{(z+1)^2}{(z-.852)^2} \tag{6-4}$$

2. Accelerometer Signal Conditioning

In the same fashion as the above procedure, conditioning the accelerometer signal is the next step in preparation for the designed controllers' experimental validation. Calibration was not necessary for the accelerometer gain factors. Values supplied by the

[10] Sony Precision Technology America, Inc., 20381 Hermana Circle Lake Forest, CA 92630

manufacturer that were listed in Section II.D.2 were coupled with the acceleration due to gravity (9.81 m/s^2) and the Simulink Correction factor (10 V/signal) to establish the appropriate adjustments.

Counter to the LVDT signal, accelerometers should not have a DC bias when immobile (as voltage is generated by motion). Not only will this confound acceleration measurements, but the velocity states integrated from these will be ever-increasing (or decreasing). This introduces quite a dilemma as the controller tries to track the reference. On the other end, high frequency attenuation is important for the state feedback that does not pass through controllers designed to attenuate this region (i.e. inertial-frame damping and adaptive control).

The chosen removal method is construction of a fourth degree band-pass filter (second-degree high-pass filter coupled with a second-degree low-pass filter). Despite the loss of low-frequency signals generated through motion, the lower cutoff frequency could be selected such that the contributions from the rejected frequencies would be neglible. If precise positioning or control was required, other methods would most likely need to be sought. It was chosen to establish the lower corner frequency at $\omega_{cl} = 0.001$ rad/s. Maintaining similarity between the LVDT signals, an upper corner frequency $\omega_{cu} = 160$ rad/s is selected. The result for unity across the pass bandwidth (established at $\omega = 10$ rad/s) is the filter in Equation (6-5).

$$F_{ACC}(s) = 25700 \frac{s^2}{(s+0.001)^2 (s+160)^2} \tag{6-5}$$

Once again, adhering to the dSPACE® compiler's requirements, the controller is emulated to discrete domain in the same manner as the LVDT filter. With a sampling interval $T = 0.001$ s, the result is that of (6-6).

$$F_{ACC}(z) = 0.0109 \frac{(z+1)^2 (z-1)^2}{(z-0.999)^2 (z-0.852)^2} \tag{6-6}$$

With the information presented in this section uploaded into dSPACE®, experimental validation is ready to commence. Experimental layout and presentation of the results are discussed in the following section.

VII. EXPERIMENTAL VERIFICATION AND RESULTS

To this point, all applicable instrumentation and processing needs have been installed and prepared for experimentation. Exciting the test rig with various profile disturbance wheels and recording the data is all that remains. In this section, the data captured from the dSPACE® system during operation is visualized, coupled with discussions of the findings.

The data presented are primarily focused on sprung mass response, particularly acceleration. While the focus in Chapter V was plotting sprung mass velocities, the goal was to see how well the controllers were able to track a reference input. This input, though, is the chosen method to tune the desired acceleration of the sprung mass. A mixture of time-based and frequency-based results will constitute the results discussion.

A. Disturbance Excitation

The test rig is designed with two exciting disks providing sinusoidal and step inputs, whose details are discussed in II.C.4. Driving this shaft is a Milwaukee®[11] variable-speed electric drill, Model 0299-20, with speed range of 0 – 850 rpm (89 rad/s). This drill is secured via cable ties to the motor mounting table and attached at the chuck to a fabricated driveshaft extension bit. Speed control is left up to the operator manually squeezing the trigger while observing the tachometer readout in ControlDesk® GUI for experimentation (see Appendix III).

Although the drill outputs substantial torque, a considerable dead-band region is present in the drill's loading system. As a result, when the disturbance excitor wheel begins its negative-slope region, sharp transients cause rapid speed changes that end in hard stops as the loading is reestablished. Hence, a leather strap is tightly wrapped around the shaft to induce enough resistance such that loading forced to one side of the dead-band.

[11] Milwaukee Electric Tool Corporation, 13135 W. Lisbon Rd Brookfield, WI 53005

The selected sequence for collecting data is to begin exciting the test rig at a nominal frequency. Once transients have been removed and the disturbance tachometer reads near its goal, an assistant initializes the data acquisition process. Collection commences for a period of 10 seconds. This process is repeated for multiple frequencies at the various experimental phases, which are discussed in greater detail below, for both the sinusoidal and step-input disturbances.

Given regard for the safety of the experimental test rig, sinusoidal excitations are swept in increments of 5 rad/s, from 10 rad/s to 40 rad/s. With much larger destructive loads present, the step input spans only from 10 rad/s to 25 rad/s.

Implementing the above excitation technique, data is gathered and plotted to reveal the accelerations endured by the sprung mass. Beginning with sinusoidal input, the data will be presented by controller type: no controller, classical, and state-space. As stated earlier, acceleration of the sprung mass is the variable of concern, and the data presentation must support its examination. Therefore, plots include time response and frequency spectrums of the sprung mass signal.

B. Sinusoidal Excitation Analysis

The first collection of experimental data involves employment of the disturbance excitation wheel that effectively applies a disturbance displacement (x_r) as a function of the wheel's angular velocity (ω), modeled by

$$x_r(\omega) = 0.0127 \sin(\omega t) \text{ m} \tag{7-1}$$

The following analysis is presented using three-dimensional plots, with axes displaying disturbance velocity, frequency, and magnitude of acceleration. In each plot, the frequency and magnitude axes display the frequency response corresponding to the sample recorded while being excited at a prescribed disturbance velocity (excitation frequency). To produce realistic values across the frequency spectrum, the sampled data set was treated as one period analyzed via a Fourier series expansion. The complex

Fourier coefficients gathered from a modified FFT analysis were converted to real-valued coefficients in the manner described in Appendix IV.

Beginning with a base response, the analysis will continue with examination of the controllers' effects on sprung mass acceleration attenuation both with and without referencing inertial-frame damping.

1. Base Response to Sinusoidal Excitation

In order to understand the controllers' effectiveness, a base plot of the test rig response to sinusoidal disturbance input with no control force is plotted. Figure VII-1 produces a response spectrum for the corresponding disturbance excitation inputs.

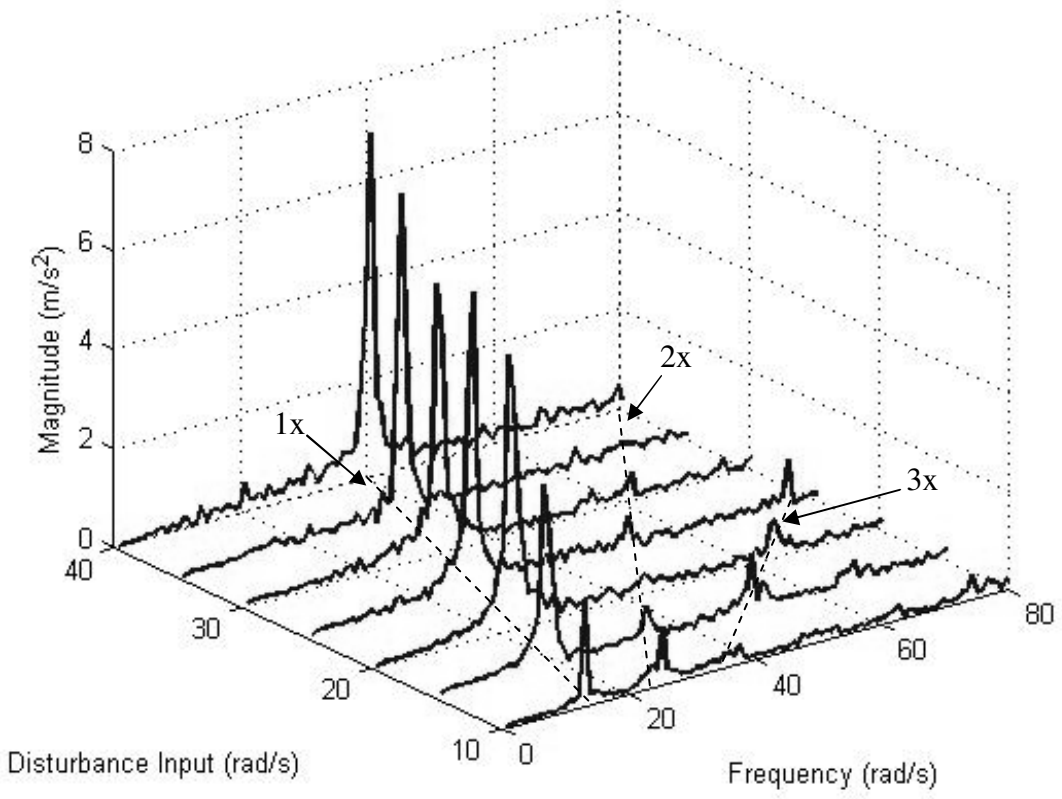

Figure VII-1 Base response spectrum of test rig (sinusoidal input)

As predicted by the model, resonance appears in between 20 and 25 rad/s, exhibited by the high points. Imperfect disturbance applied (see Section VII.A) gives the characteristics of a sawtooth wave, with harmonic peaks a along the 2x and 3x lines. However, with the 1x and 3x frequencies being the largest, there is additional square-wave dynamics present, showing the noticeable coulomb friction inherent in the system. The significance of the second peak in the 10 rad/s disturbance is its vicinity to the system resonance.

In the time domain, the two plots referring to 15 rad/s and 25 rad/s disturbance excitations are shown in Figure VII-2, elaborating on the information above.

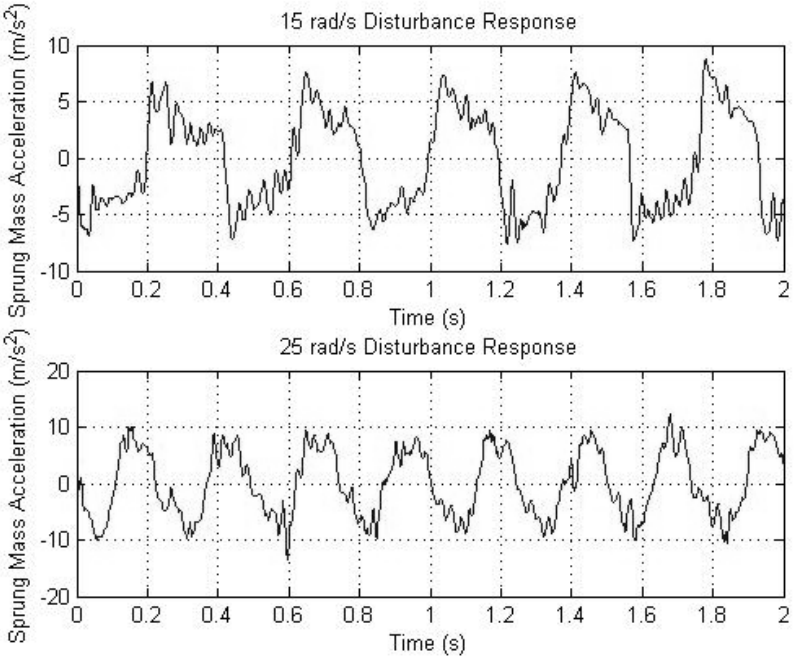

Figure VII-2 Base time response of test rig (sinusoidal input)

Clearly exhibited is the prominent square-wave dynamics and underlying sawtooth-wave presence (especially with the 15 rad/s response). Also, as expected, the overall amplitude is larger at 25 rad/s, but the aforementioned amounts of coulomb friction present limit the sprung mass acceleration to around 10 m/s^2. Comparisons of the compensated responses will be made to this, a basis for determining the usefulness of the controllers.

2. Classical Control Response to Sinusoidal Excitation

Paralleling the analysis of the base response dynamics, the test rig response with the classical controller in place is examined. The order of analysis is placed by the equivalent magnitude of inertial-frame damping reference. Specifically, trials of damping values C_{ifd} = 250 N-s/m, 500 N-s/m, and 1000 N-s/m will lead, followed by the zero reference response. The following plots dissect the collected sprung mass acceleration signals. Before discussion of the observations gathered from this data, the responses of all trials are displayed in the same fashion as shown in Figure VII-1 and Figure VII-2.

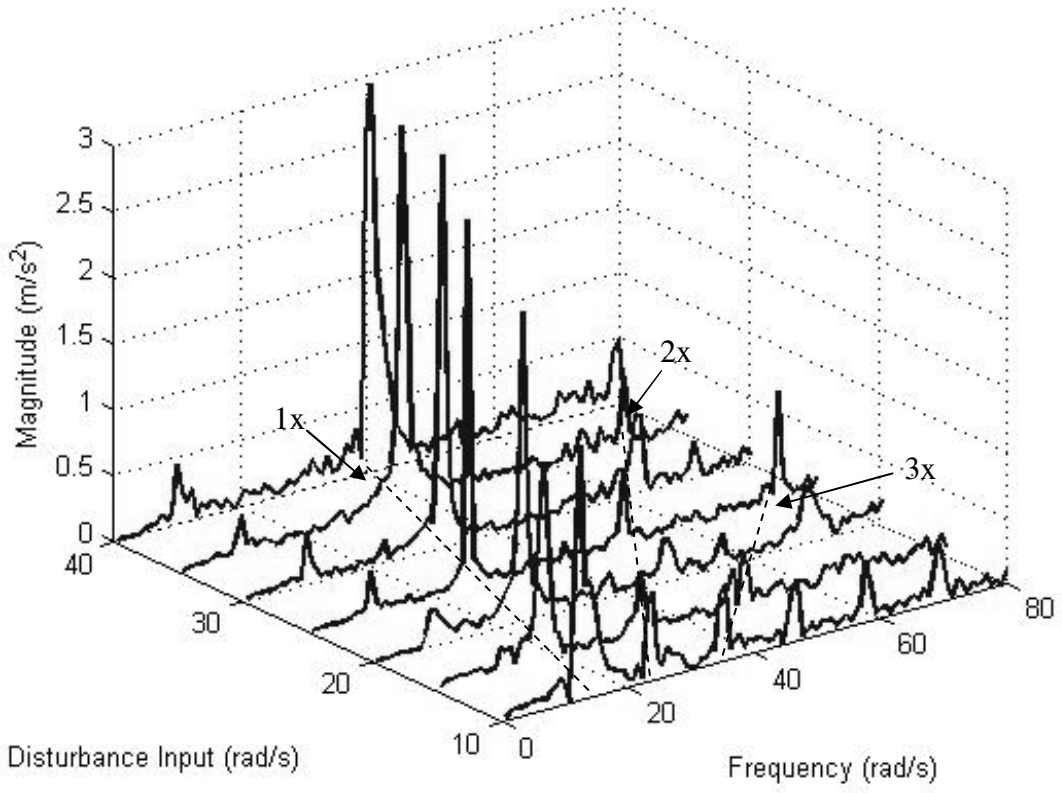

Figure VII-3 Classical response spectrum of test rig (sinusoidal input), C_{ifd} = 250 N-s/m

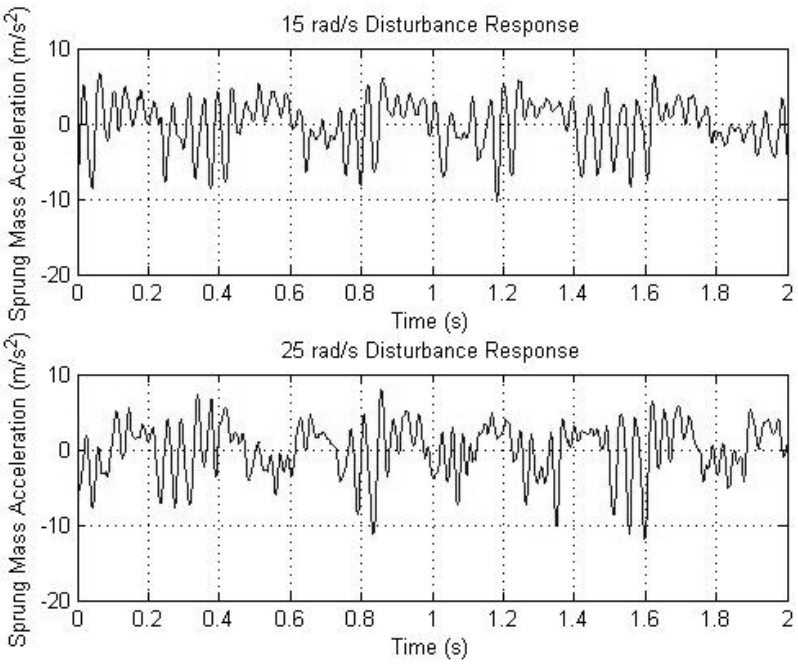

Figure VII-4 Classical time response of test rig (sinusoidal input), C_{ifd} = 250 N-s/m

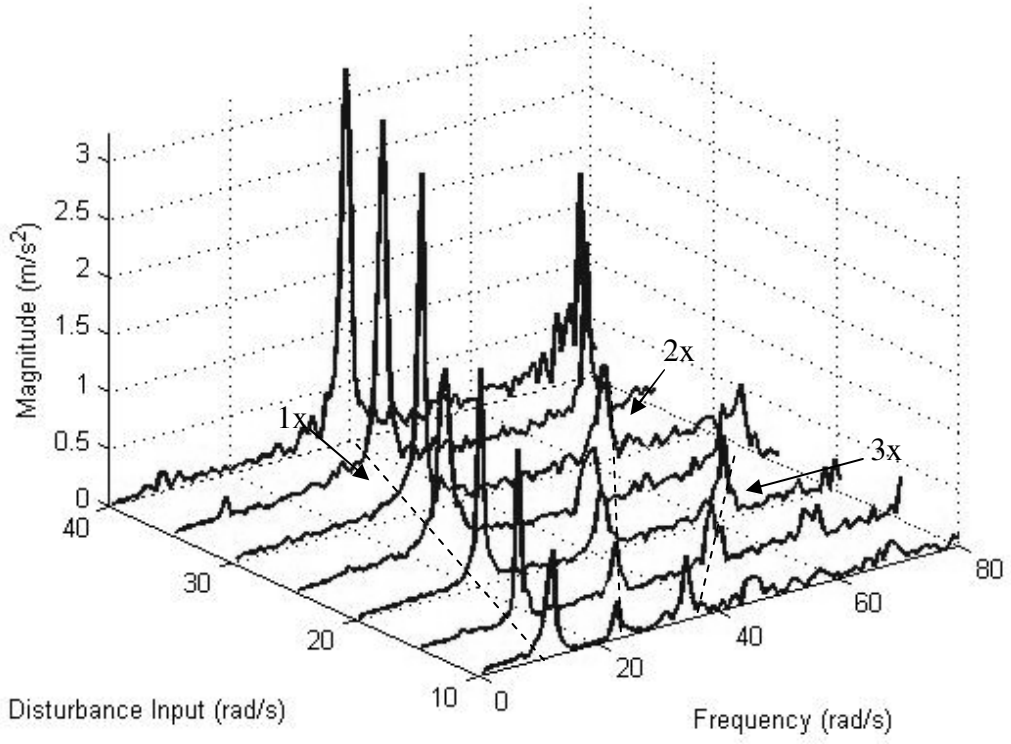

Figure VII-5 Classical response spectrum of test rig (sinusoidal input), C_{ifd} = 500 N-s/m

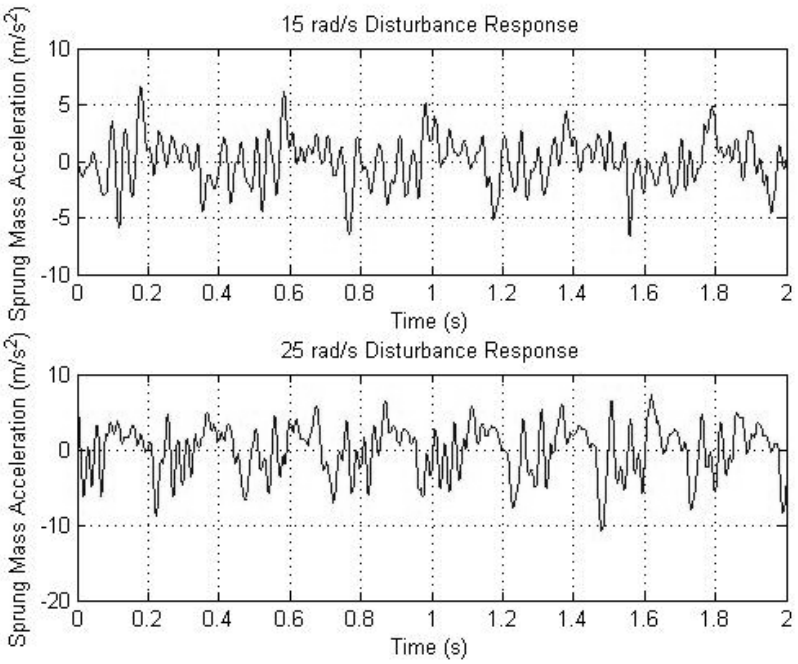

Figure VII-6 Classical time response of test rig (sinusoidal input), C_{ifd} = 500 N-s/m

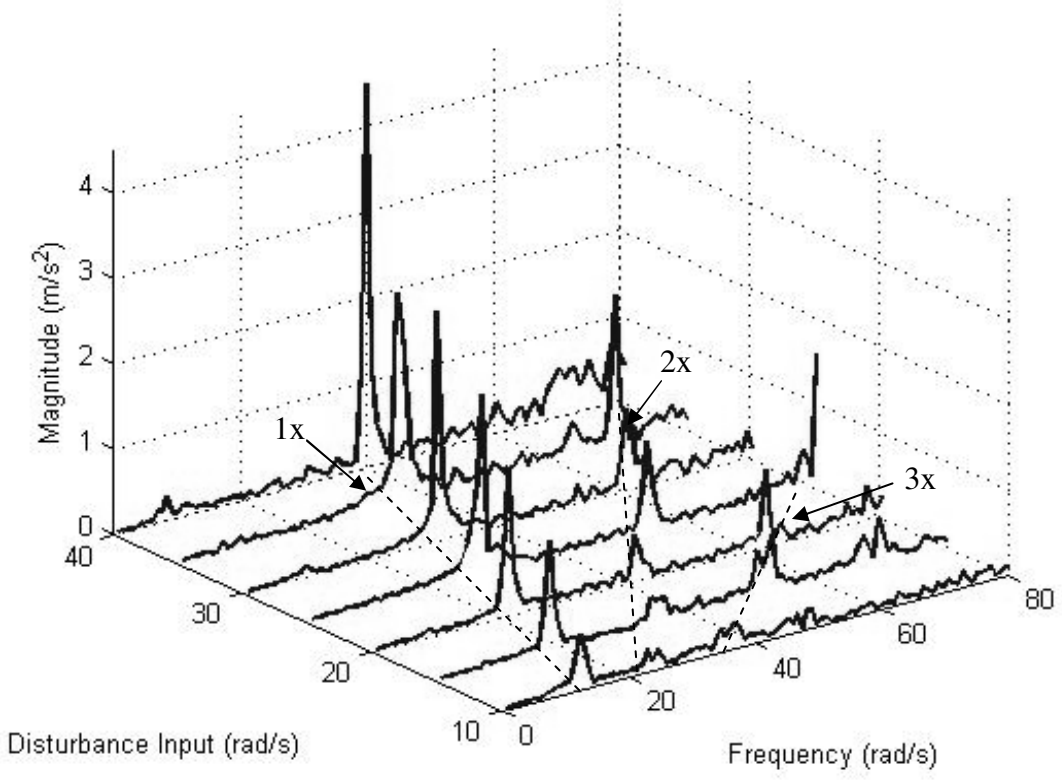

Figure VII-7 Classical response spectrum of test rig (sinusoidal input), C_{ifd} = 1000 N-s/m

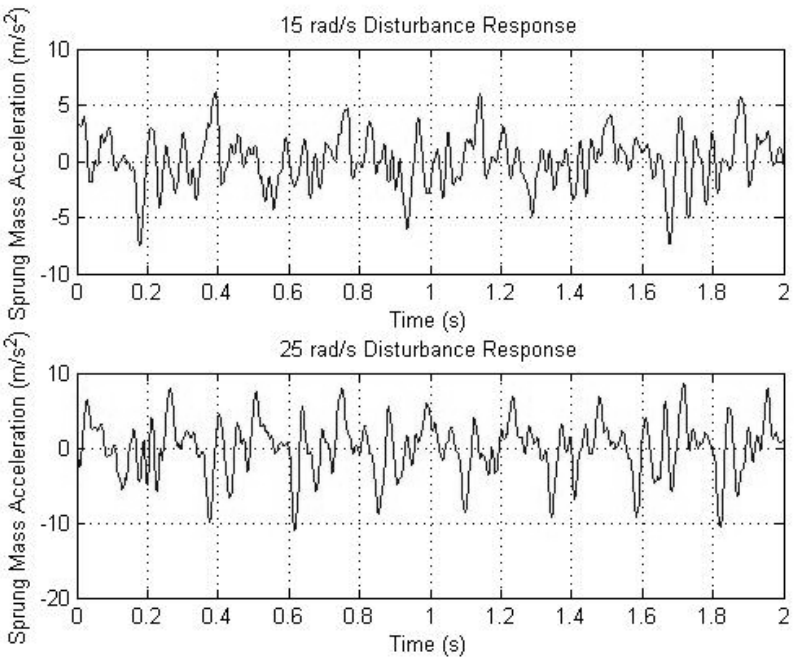

Figure VII-8 Classical time response of test rig (sinusoidal input), C_{ifd} = 1000 N-s/m

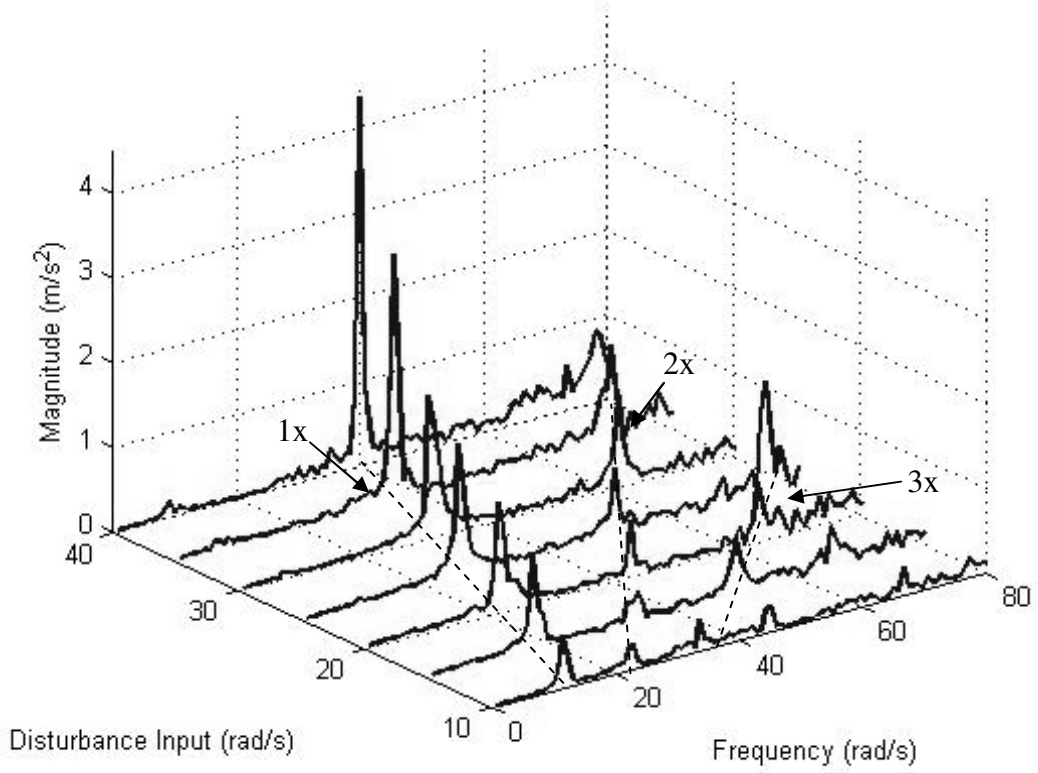

Figure VII-9 Classical response spectrum of test rig (sinusoidal input), zero reference

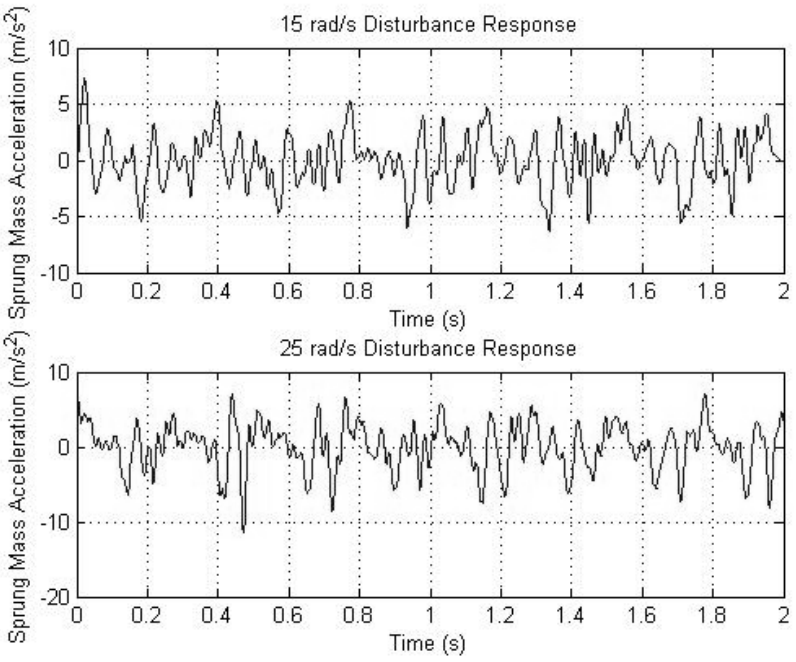

Figure VII-10 Classical time response of test rig (sinusoidal input), zero reference

Figure VII-3 displays the frequency spectrum for the sprung mass acceleration after adding compensation and a reference of C_{ifd} = 250 N-s/m. Similarly, Figure VII-4 shows the time response for the 15 rad/s and 25 rad/s disturbance. Again, the sawtooth and square-wave components are present, denoting the strong effects of coulomb friction forces and disturbance input dynamics. Overall, though, disturbance rejection in the controller bandwidth is much better, as the 1x output is attenuated approximately 50%. Higher-frequency dynamics intervene, however, and cause spikes that seem to negate the rejection effects, as evidenced by the amplitudes present in the time response of Figure VII-4.

With the classical controller tracking the inertial-frame damping reference C_{ifd} = 500 N-s/m, the response spectrum is plotted in Figure VII-5 and time response in Figure VII-6. The disturbance frequencies excite the sprung mass in similar fashion to the same reference using C_{ifd} = 250 N-s/m, but with slightly better performance at the lower band. It is now easy to see that the bandwidth of the controller that rejects the largest amount is $\omega <$ 30 rad/s. Rejection is still agreeable at ~50% with a 40 rad/s disturbance. The time responses show better attenuation than those pertaining to

C_{ifd} = 250 N-s/m. Higher frequency components still introduce large spikes, but the recognition of the controller bandwidth exemplifies the controller's inability to remove said disturbances.

For the classical compensated response referenced to C_{ifd} = 1000 N-s/m, Figure VII-7 displays the frequency response of the acceleration at the various disturbance frequencies. The result is further rejection of the 1x responses, and this time the controller's bandwidth seems to have increased by providing good rejection through ω = 35 rad/s. No improvement is made from the previous C_{ifd} reference at 40 rad/s, signifying that either motor saturation is limiting the bandwidth of the controller or modeling errors could have introduced unstable margin shifts. Figure VII-8 expresses the same results, as the acceleration amplitudes are improving save the high frequency spikes.

Finally, the frequency spectrum for the classical-compensated response trying to track the zero reference input is shown in Figure VII-9 (time-based reponse shown in Figure VII-10). When comparing the frequency spectrum magnitudes to the base response plot in Figure VII-1, The response when applying zero reference is the best yet for frequency components below ω = 35 rad/s. At the frequency component along the 1x line (synchronous to the disturbance input frequency), Figure VII-9 displays nearly 80% rejection at 25 rad/s when compared to the base response. At ω = 35 rad/s, though, the inertial-frame damping reference with C_{ifd} = 1000 N-s/m provides a better synchronous rejection of 67% compared to 60% from zero reference. This trend continues for the other inertial-frame damping values, as the response resulting from inertial-frame damping reference C_{ifd} = 250 N-s/m rejects 57% of the synchronous disturbance, compared to 39% rejection when using zero reference. The suggestion is that when higher disturbance frequencies are presented, relaxation of the inertial-frame damping value would perform better than maintaining a fixed value throughout the entire disturbance excitation spectrum.

Overall, the classical controller performs well. The effects of coulomb friction were not able to be overcome, which seemed to be the cause for introducing the high-frequency spikes.

3. State-space Control Response to Sinusoidal Excitation

Moving on, the same the same sequence of experimentation is conducted on the state-space controller design. Simulation results from Section V.B.3 yield responses less desirable than those of its classical counterpart. Evaluation on the actual plant is the true basis for the effectiveness of this design, however.

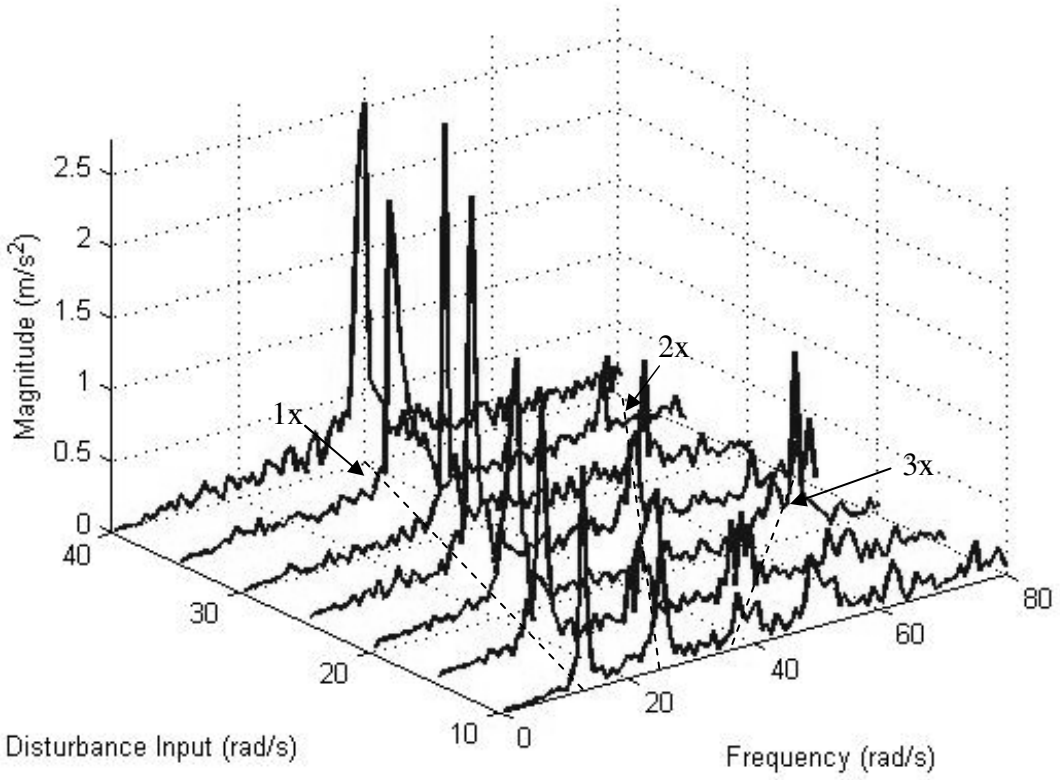

Figure VII-11 State-space response spectrum of test rig (sinusoidal input), C_{ifd} = 250 N-s/m

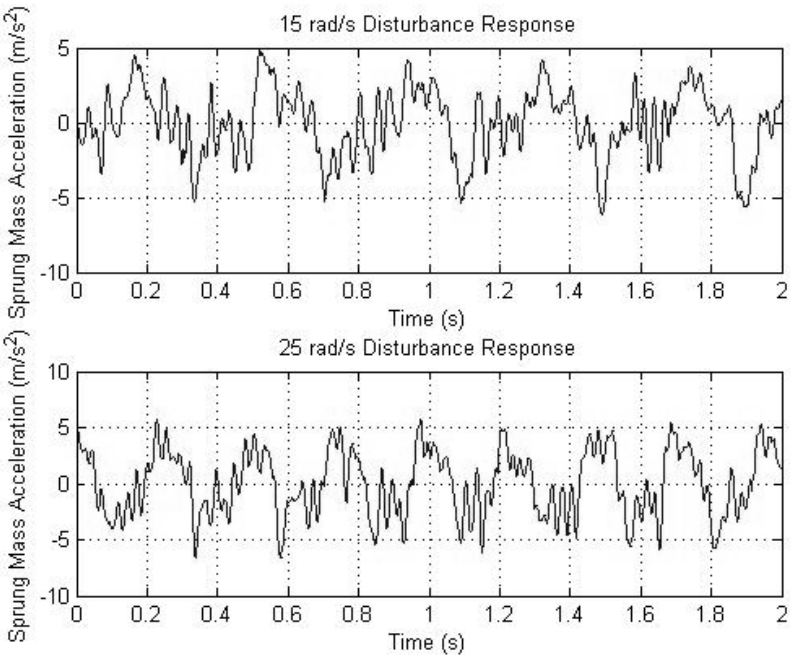

Figure VII-12 State-space time response of test rig (sinusoidal input), C_{ifd} = 250 N-s/m

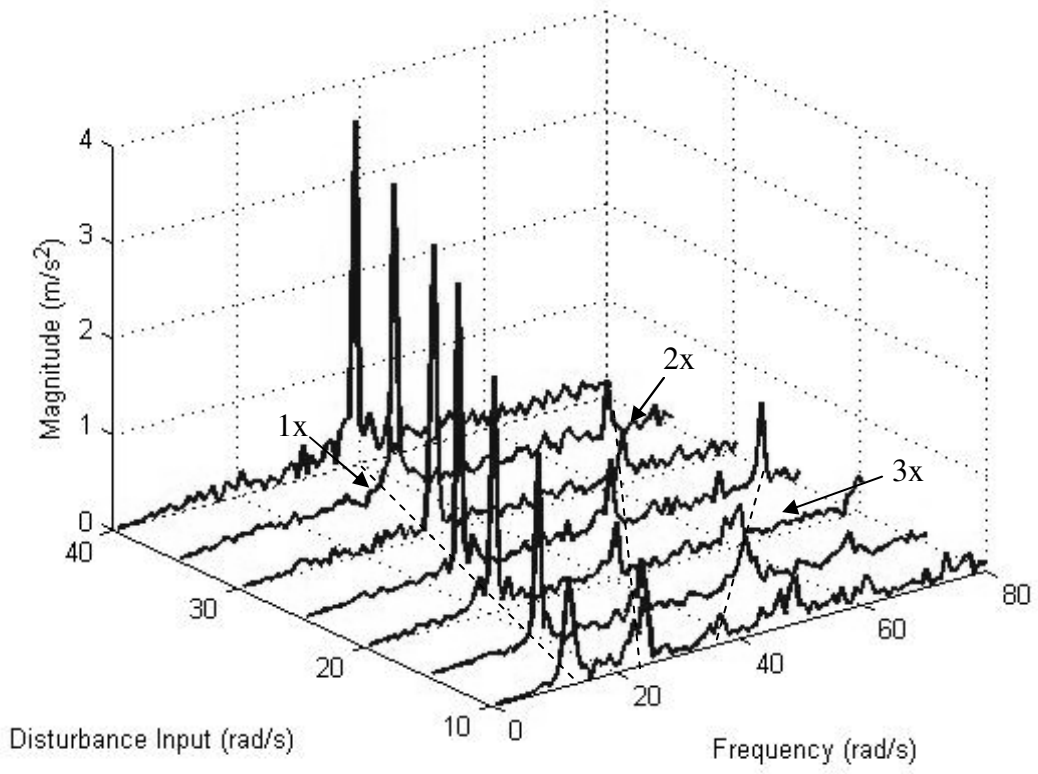

Figure VII-13 State-space response spectrum of test rig (sinusoidal input), C_{ifd} = 500 N-s/m

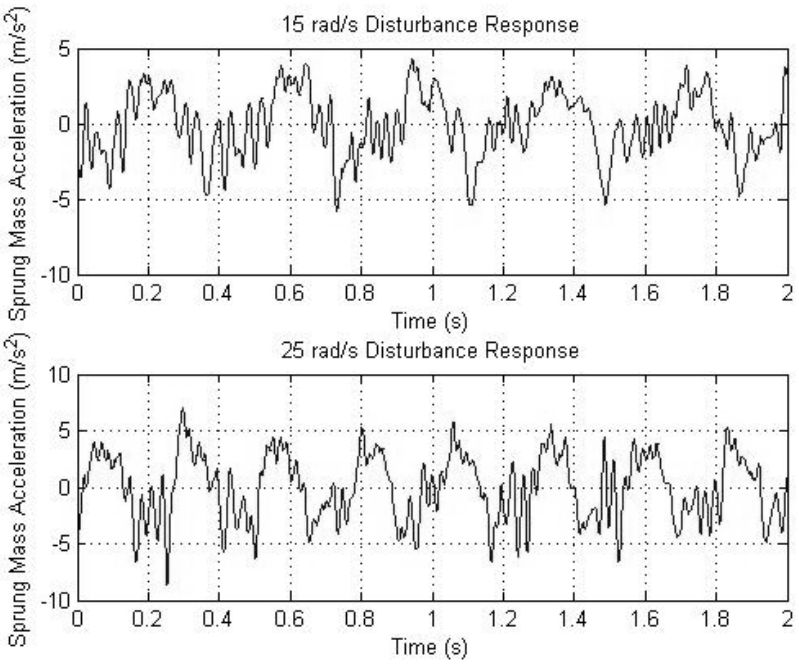

Figure VII-14 State-space time response of test rig (sinusoidal input), C_{ifd} = 500 N-s/m

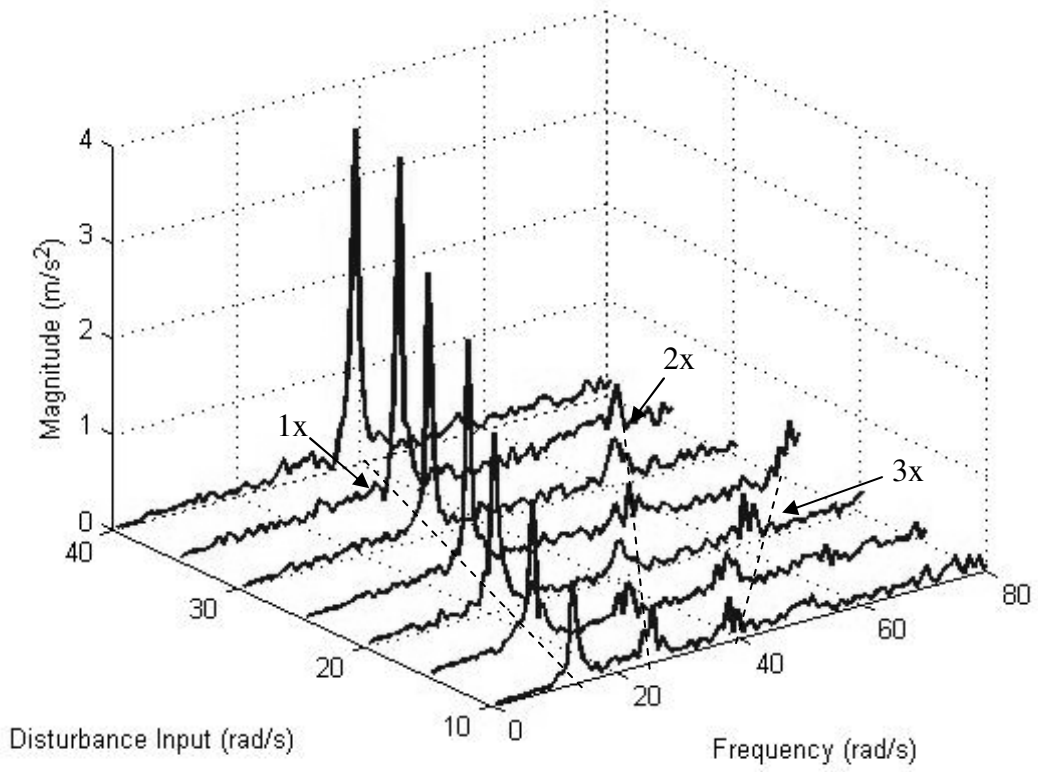

Figure VII-15 State-space response spectrum of test rig (sinusoidal input), C_{ifd} = 1000 N-s/m

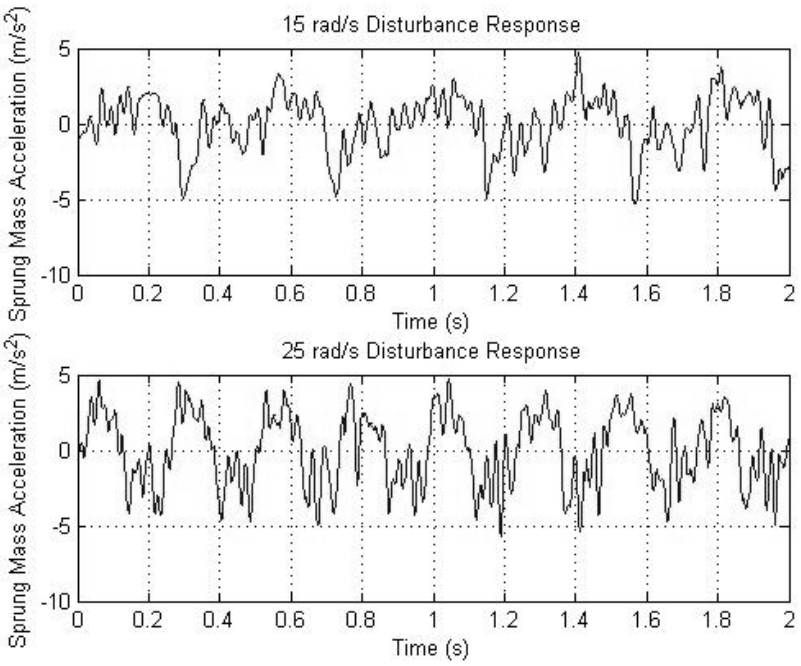

Figure VII-16 State-space time response of test rig (sinusoidal input), C_{ifd} = 1000 N-s/m

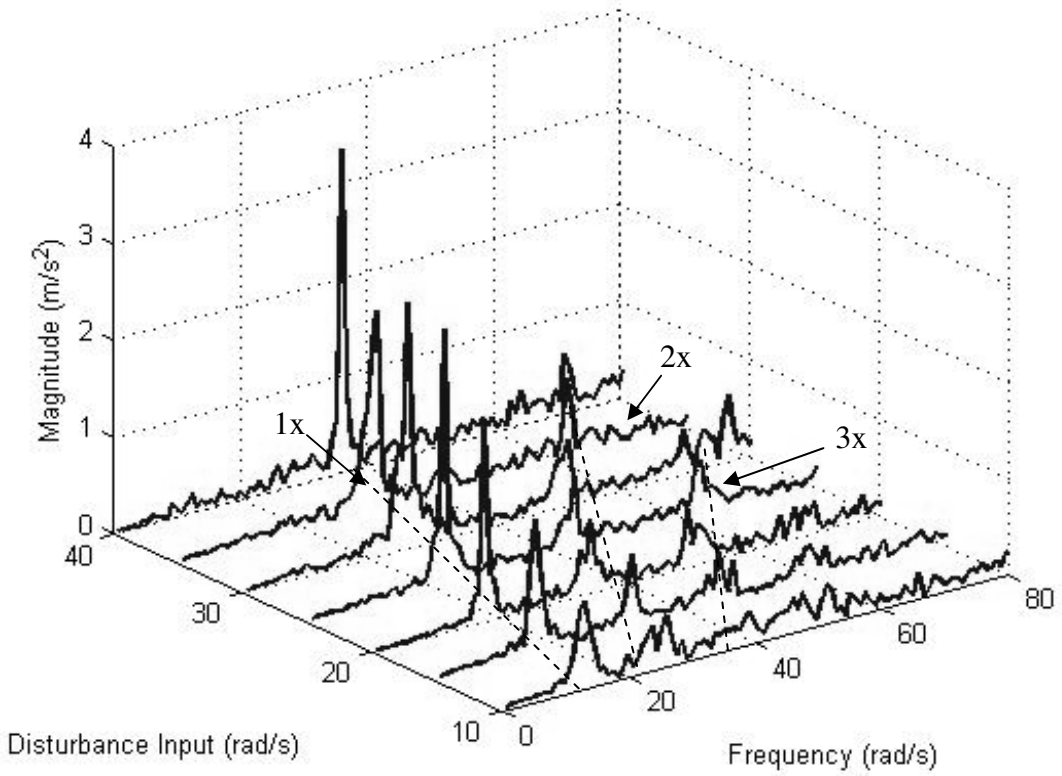

Figure VII-17 State-space response spectrum of test rig (sinusoidal input), zero reference

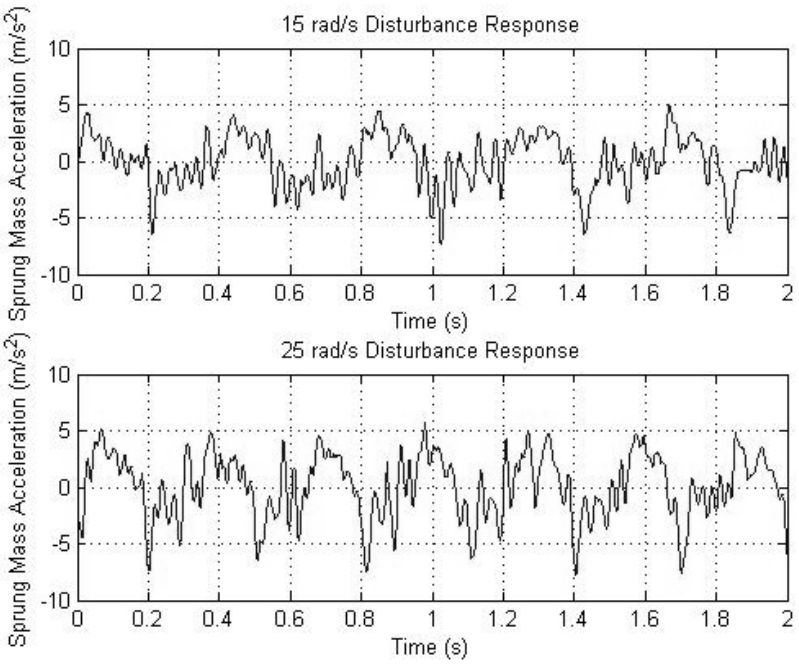

Figure VII-18 State-space time response of test rig (sinusoidal input), zero reference

Contrary to simulation results, the state-space controller performed quite respectably. In fact, the spectrum presented in Figure VII-11 as the result of tracking a inertial-frame damping reference C_{ifd} = 250 N-s/m displays response nearly identical with its classical control counterpart. However, the responses to disturbances at frequencies of 35 rad/s and 40 rad/s are slightly lower. Figure VII-12 confirms this statement, with the responses containing lower amplitudes due to high-frequency spikes.

Likewise, rejection of 1x disturbances continues to emulate the results of classical control, shown in Figure VII-13. The reference inertial-frame damping value of 500 N-s/m begins to approach the high-frequency attenuation limitations higher than 35 rad/s, but the rejection at 25 rad/s is somewhat lower at ~68%. Figure VII-14 shows that high-frequency additions are not as large, though, when compared to the same reference with classical control.

Raising the inertial-frame damping value to C_{ifd} = 1000 N-s/m has little effect on the upper disturbance frequencies along the 1x line, but supersynchronous (greater than 1x) frequencies that contribute to the sawtooth and square-wave components seem to

have decreased in Figure VII-15. Again, Figure VII-16 shows that these high-frequency subsets are not as prominent as with the preceding control design.

Wrapping up the sinusoidal disturbance experimentation with the state-space design, Figure VII-17 displays the frequency spectrum coinciding with the sprung mass acceleration with zero reference input. Rejection across the widest band is evident when compared to the inertial-frame damping, but once again the response at 40 rad/s is not as reduced. Also, the resonance disturbance of 25 rad/s is not as greatly rejected as the classical controller, with about 68% again removed. The benefit by contrast is once again the controller's ability to avoid peaks from high-frequency signals, shown by Figure VII-18.

Overall, the state-space controller's ability to reject disturbance inputs sinusoidal in nature is quite good. As with the classical controller's response using inertial-frame damping, lower values offered the best high-frequency rejection, while low frequencies were best removed by using a zero reference input signal.

C. Step Input Excitation Analysis

In the previous section, a detailed discussion covering the effects of the controllers and various reference inputs on rejecting sinusoidal road disturbances. With the excitation altered, the same line of experimentation is conducted. Frequencies are not tested to as large a magnitude, though; sharp lateral loading that occurs with such excitation application proves to be too much stress on the rig components. Prior screening exercises at frequencies higher than 25 rad/s dismantled the test rig, requiring, in one case, remanufacturing of the unsprung mass vertical guide supports.

Mathematically, the step input disturbance excitation produces a square wave, in which one wheel revolution spans one period (as in the sinusoidal excitation wheel). The angular profile is defined as follows:

$$x_r(\theta) = \begin{cases} 0 \text{ m} & , 0 \le \theta < \pi \\ 6.35\text{x}10^{-3} \text{ m}, & \pi \le \theta < 2\pi \end{cases} \tag{7-2}$$

Data is presented exactly as before, with an analysis on the base response followed by the classical and state-space controllers. The inertial-frame damping reference studies, though, are left out in consideration of test rig preservation.

1. Base Response to Step Input Excitation

The response of the test rig without any compensation is displayed as the spectrum of frequency components in Figure VII-19.

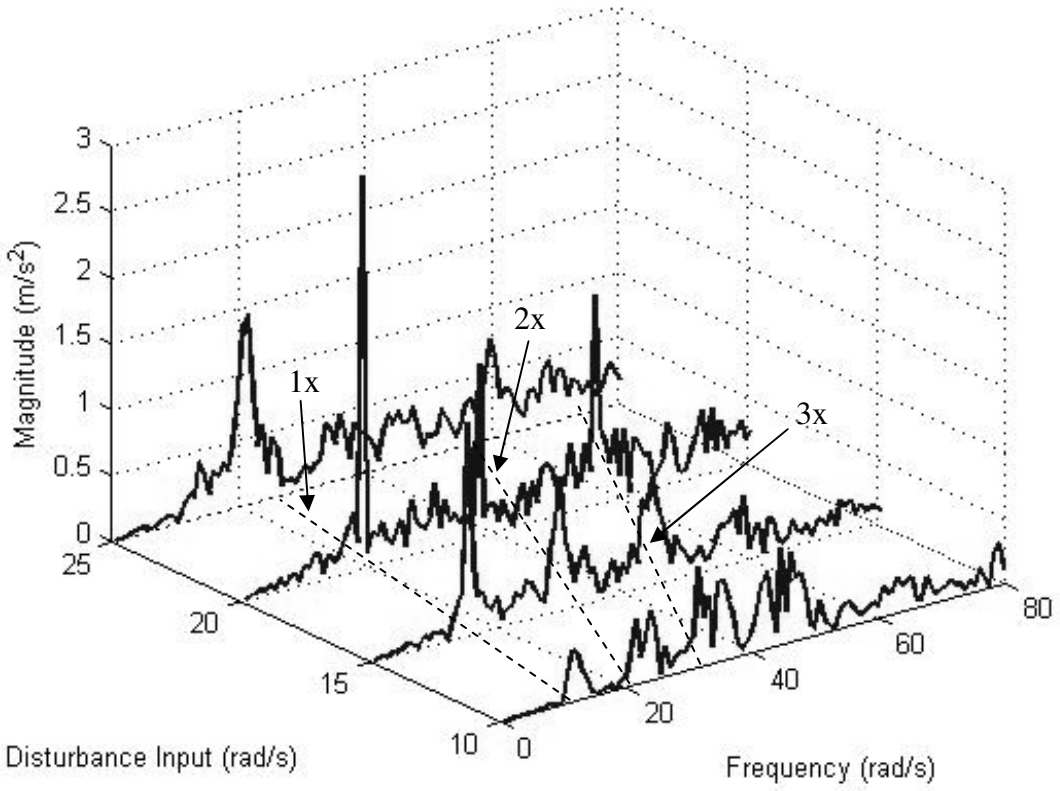

Figure VII-19 Base response spectrum of test rig (step input)

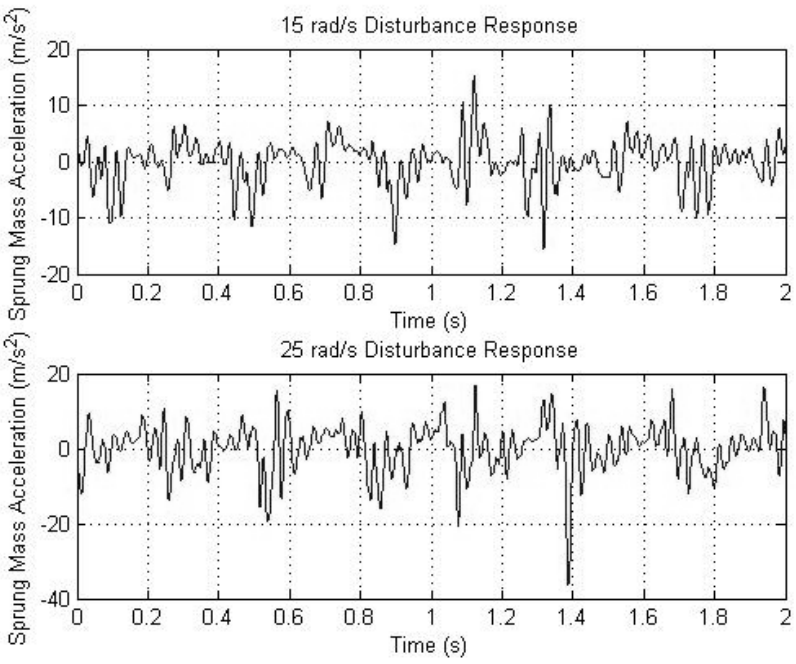

Figure VII-20 Base time response of test rig (step input)

Once again, every harmonic component is present in the prescribed range, showing that the response contains a sawtooth pattern. Additionally, since a step input disturbance will excite theoretically an infinite frequency response, all disturbance inputs have a strong acceleration component at the system's damped natural frequency of roughly 20 rad/s. Figure VII-20 backs up this sawtooth pattern in both disturbance responses, with the incline becoming much more prominent in the 25 rad/s disturbance plot. Also, the binding explains the sharp peaks in the time responses.

2. Classical Control Response to Step Input Excitation

Employing the classical controller, the frequency response spectrum and time response are plotted in Figure VII-21 and Figure VII-22, respectively.

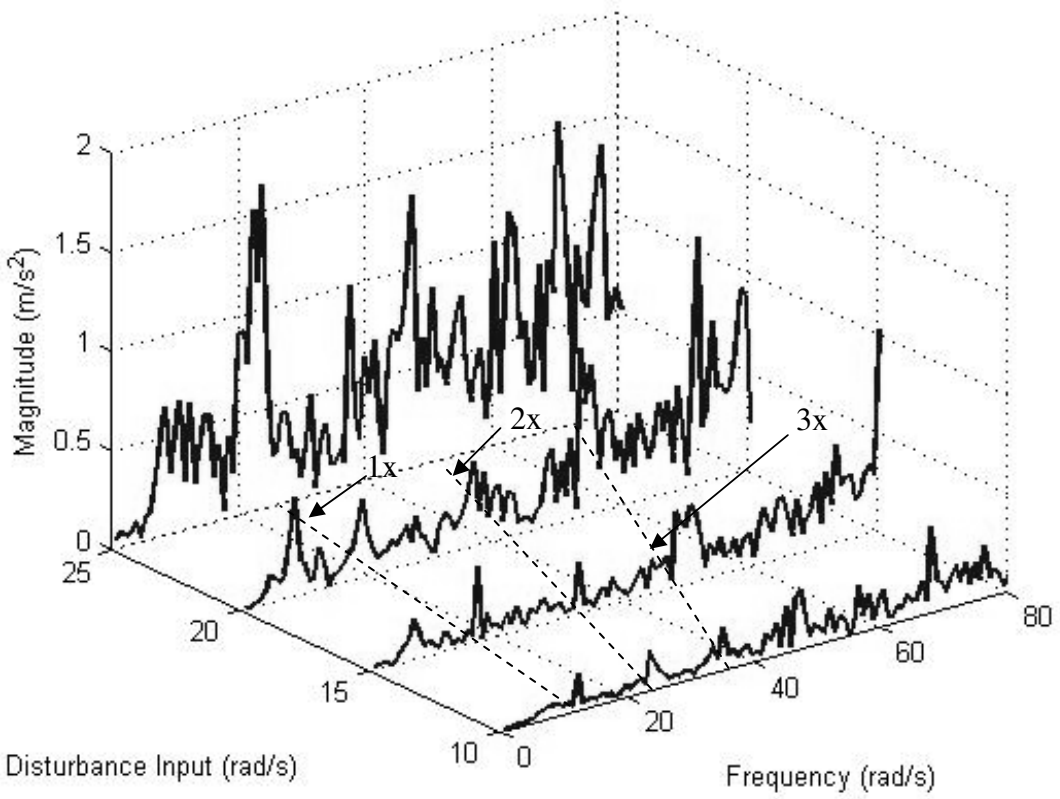

Figure VII-21 Classical response spectrum of test rig (step input), zero reference

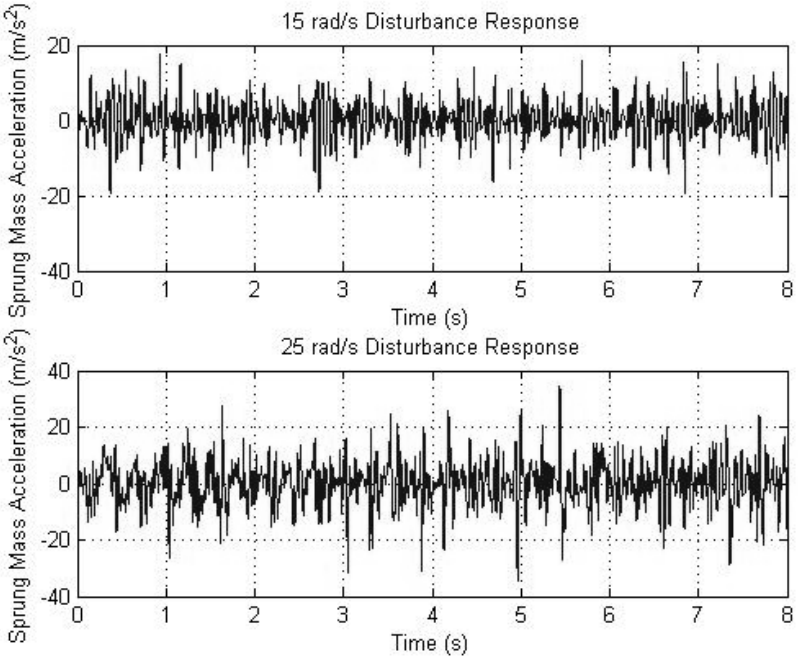

Figure VII-22 Classical time response of test rig (step input), zero reference

The controller works extremely well at rejecting the damped natural frequency components across the first three disturbances. It appears that when the wheel is spinning at 25 rad/s, though, lateral forces are significant and the motor is not able to counteract the resulting friction resistances generated. Overall, in the range of effectiveness, the classical control works well. As an example, the 20 rad/s damped natural frequency acceleration contribution is almost 85% rejected when the 20 rad/s disturbance is active.

3. State-space Response to Step Input Excitation

Rounding out the analysis involving step disturbances is the effect of compensation with the state-space controller. Figure VII-23 explores the frequency response spectrum, with Figure VII-24 displaying the acceleration based in the time domain.

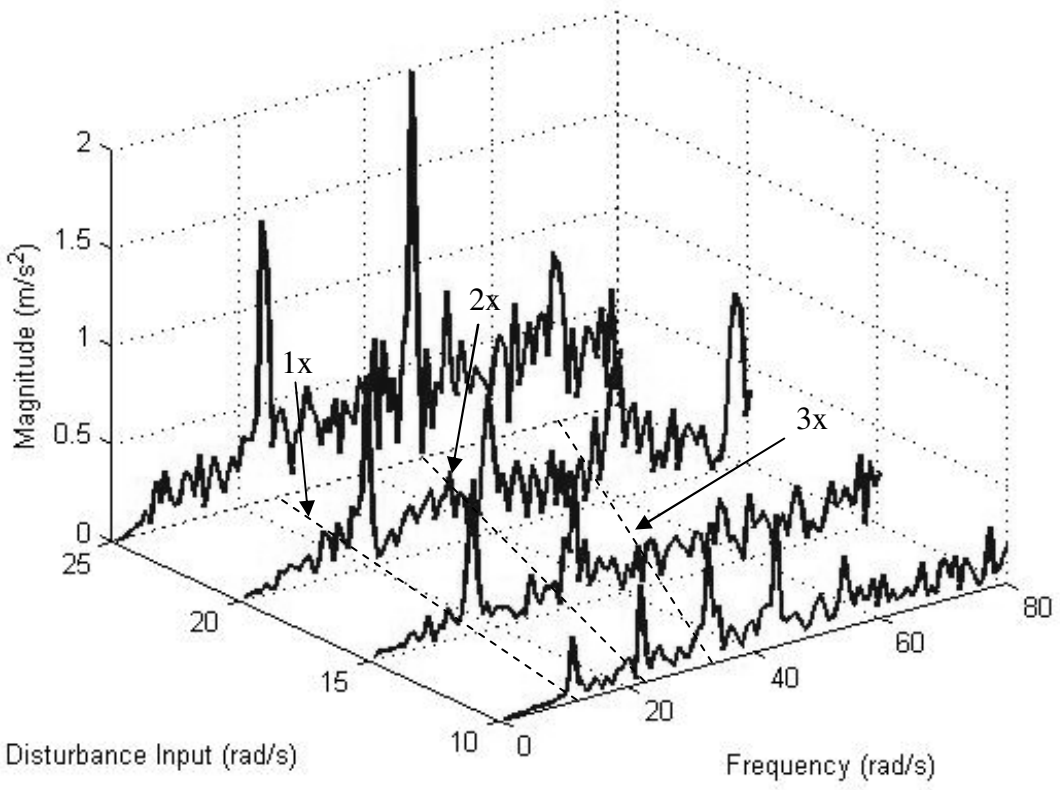

Figure VII-23 State-space response spectrum of test rig (step input), zero reference

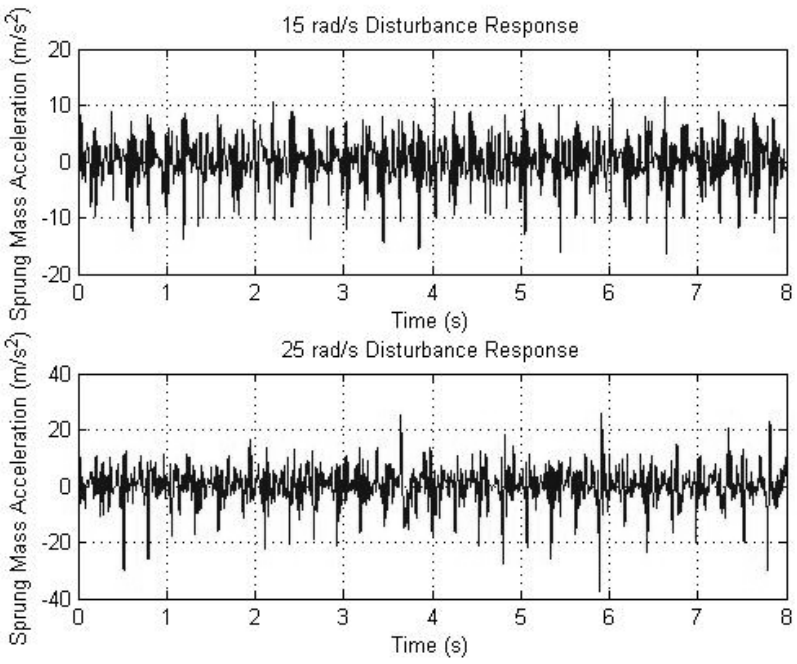

Figure VII-24 State-space time response of test rig (step input), zero reference

As in the other responses, the appearance of binding is exemplified by the sawtooth harmonics present in the frequency spectrum and large spikes in the time domain. While rejection of the damped harmonic frequency is not as dominant as it was for the classical control response, the other components exhibit smaller amplitudes similar to the sinusoidal excitation comparison.

Physically, this section of experimentation was extremely taxing on the system, forcing limitations on the disturbance applied. Evidence of the periodic sharp peaks in time domain signify that, because they are in the normal direction to the laterally-applied force, a surge of friction loading is suspect at the steps.

D. Mass Addition Experimentation Testing Controller Robustness

To further complement the demonstrations of controller effectiveness, it was decided to gauge how well the system would respond to an addition of an arbitrary mass, an unknown every vehicle experiences. Theoretically, the end product would be a leftward shift in natural frequency. Since this would slide the resonance into a regime of

better stability, it is strongly believed that the system would behave in a more stable manner, and this is intended to be validated via experimentation. Below, all three controllers are subjected to the plant with added mass arbitrarily selected to be 0.548 kg (about 17% of the sprung mass). The chosen reference for all cases is zero input velocity.

1. Classical Control Response to Added Mass

In the same manner as the preceding analysis, the response is broken into both the frequency domain and time domain, as shown in Figure VII-25 and Figure VII-26 respectively.

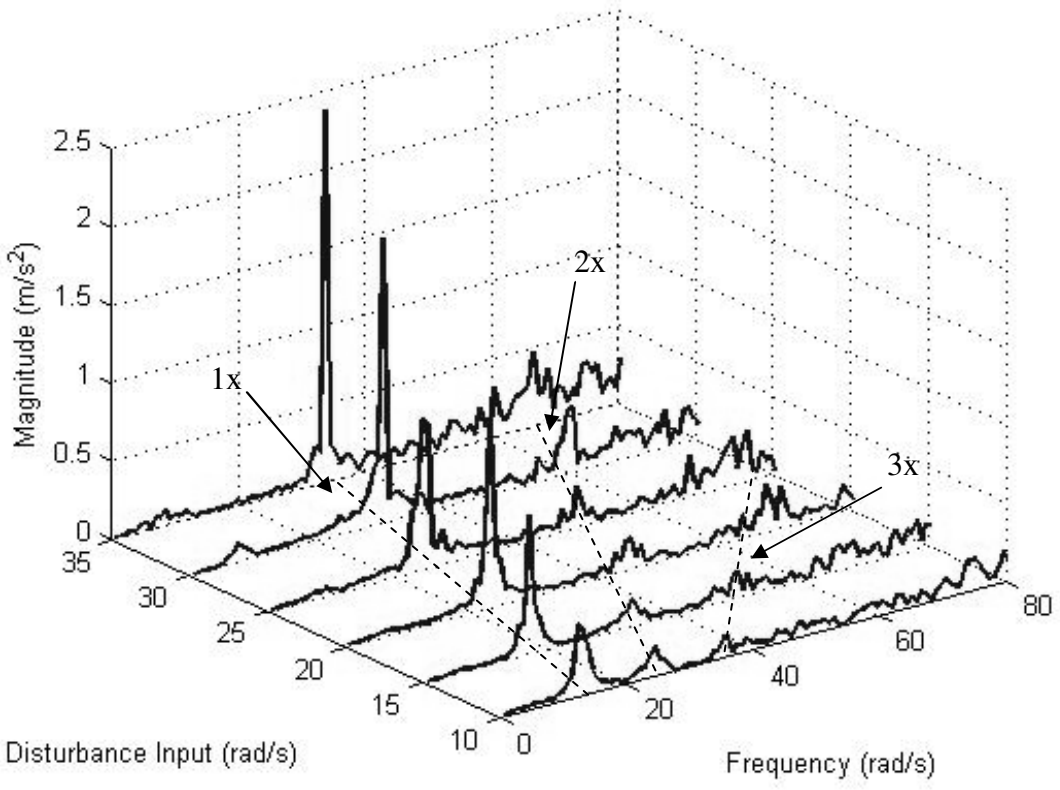

Figure VII-25 Classical response spectrum of test rig with added mass, zero reference

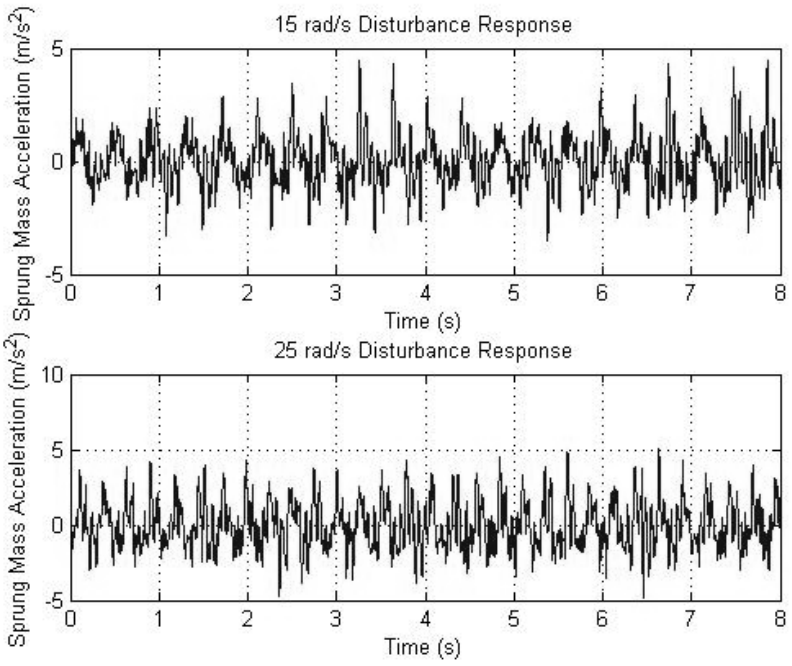

Figure VII-26 Classical time response of test rig with added mass, zero reference

As predicted, the sprung mass response for the lower disturbance frequencies is better than without the mass. Once again, though, the disturbances above 30 rad/s produce large synchronous magnitudes. Again, the sawtooth pattern is present in both frequency component representation and time domain pattern. Overall, though, the controller is well-suited for this type of plant alteration.

2. State-space Response to Added Mass

Figure VII-27 presents the frequency domain plot of the state-space compensation applied to the response of the sprung mass acceleration. Likewise, the time domain representations for disturbances at 15 rad/s and 25 rad/s are shown in Figure VII-28.

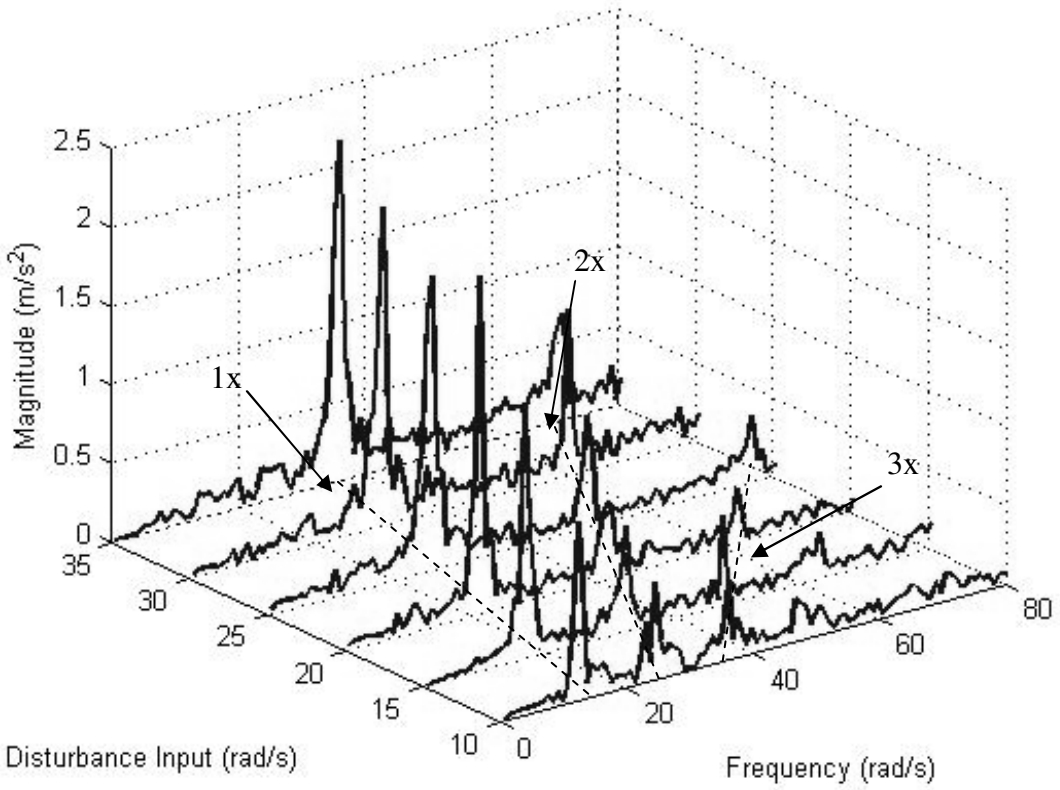

Figure VII-27 State-space response spectrum of test rig with added mass, zero reference

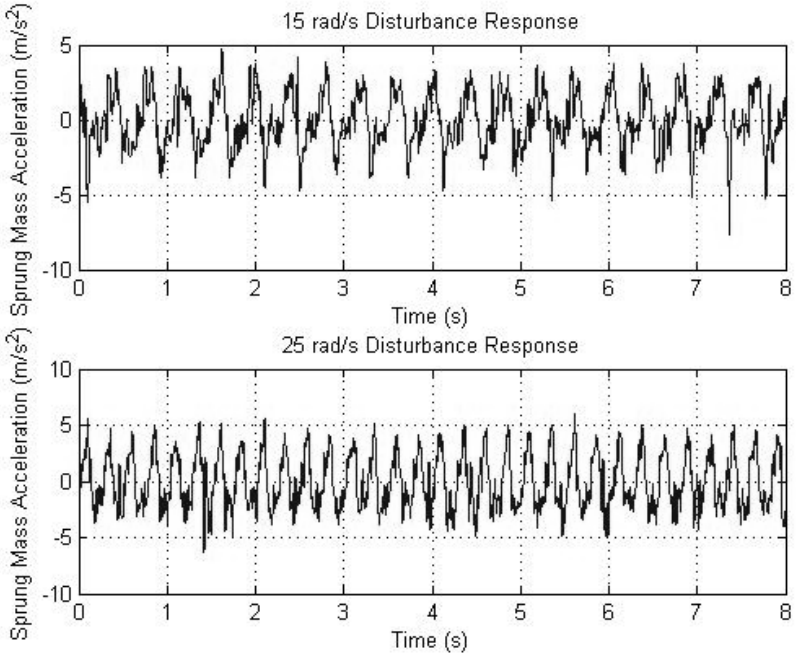

Figure VII-28 State-space time response of test rig with added mass, zero reference

The state-space controller is not as receptive to changes in the sprung mass, as the spectrum plots exhibit larger magnitudes across the plot. When comparing quantitatively, the results of the state-space response magnitudes are about twice their classical counterparts under 30 rad/s. Above this, the values do not vary significantly. Additionally, sawtooth patterns are very pronounced in the time-based plots of Figure VII-28.

Experimental data has been presented and interpreted in great detail. Many hypotheses constructed as to why such happenings occurred. In the following section, the findings expressed and this work concluded. From these conclusions, a recommendation for future work will be proposed for further investigation of optimal control schemes on this quarter-car model.

VIII. CONCLUSIONS AND SUGGESTIONS FOR FUTURE WORK

The contents of this thesis were driven by the implementation of a novel tubular linear motor in a simulated automotive active suspension experiment. Spanning mechanical and software design, fabrication, and testing this document began with a study of similar investigations and ended with a fairly successful system of disturbance rejection. In this section, a discussion of the concluded findings and inspiration for further investigation will be presented.

A. Conclusions

1. Summary of Testing Results

The results section displayed the success enjoyed by the control systems in removal of disturbances to the sprung mass acceleration. Through analysis of the presented plots, the classical and state-space controllers produced sinusoidal disturbance rejection of at worst 50% within their respective bandwidths. At 25 rad/s, the classical controller was able to remove 80% of the base synchronous component, while the state-space controller filtered out nearly 60%. Rejecting disturbances at 40 rad/s was only about 37% with the classical controller, compared to the ~50% rejection of the state space controller. Additionally, the state-space controller would produce better time-based amplitudes when compared to the large spikes present in the acceleration response of the classical compensated system.

The introduction of the inertial-frame damping model for reference input showed improvement at higher-frequency disturbance rejection. Sinusoidal response synchronus components at 40 rad/s using the classical controller were 33% better when inertial-frame damping of C_{ifd} =250 N-s/m. Likewise, the sinusoidal synchronous response under the

employment of the state-space controller enjoyed a 28% reduction in magnitude at 40 rad/s, using the IFD value C_{ifd} =250 N-s/m.

Analysis on the system's ability to reject step disturbances was greatly confounded with the destructive lateral loading transferred during the excitation process. As a result, subjection to excitation could only occur up to 25 rad/s. Across the band, the controllers again were able to attenuate successfully the components within their bandwidths; at the 20 rad/s synchronous response, the classical and state-space controllers removed 85% and 70% of the disturbance, respectively. However, since a theoretically infinite band of frequencies is excited through the step disturbance, the higher frequency components that are brought about from the square- and sawtooth wave dynamics overpowered, resulting in sharp spikes of large amplitude.

2. Conclusions of Test Rig Dynamics

The strong presence of supersynchronous harmonics present in all frequency-spectrum responses prompted a small investigation. First, the peaks occurring at the 1x, 2x, and 3x lines signified there was some sawtooth pattern present in the response. Stronger peaks at the odd harmonics (1x and 3x) led to the conclusion that square-wave dynamics were also prevalent. The conclusion is that the installed roller guides supplied little lateral support, contrary to their intent. Instead, the bulk of lateral stability was introduced through the sliding contacts of the motor shaft and, installed after realization of sharp loading on the motor, a steel rod riding in a bronze bushing. While multiple lubrication techniques were attempted, there was noticeable binding occurring when the wheel was excited upward. The plots of time-based acceleration show strong correlation to this type of movement, which becomes more pronounced as excitation frequency increases.

3. Noise Attenuation Conclusions

Other than the significant friction in inherent in the test rig and ensuing binding, further study concluded that the filters' cutoff frequencies were designed too closely to the operating bandwidth. While not affecting the magnitude across the band, the phase collapse introduced a bit of instability.

Screening exercises prior to experimentation resulted in optimization of control gains. Originally, the gains were reduced because high frequency spikes in the accelerometer noise would make the rig jump uncontrollably. The filter installation remedied these, but the control gains (and ultimately the bandwidths) were sacrificed. However, the success after adding the filters far outweighed the losses, and so they remained. Future experimentation, though, would warrant reexamination of these filters.

B. Recommendation for Future Work

The conclusions presented over the test rig prompt the suggestion for better lateral stability. Large moments induced on the unsprung mass by the lateral wheel loading bind the system, causing unavoidable sawtooth motion characteristics. It is recommended that the either lateral stabilizers are constructed to minimize sliding resistance or replace the wheel excitation system with one that contributes vertical motion only. While the initial design proved useful, these changes will contribute greatly to the effectiveness in experimentation.

Increasing the capability of the motor is another suggestion that will provide greater freedom in control algorithm design. Much time was spent trying to maintain the best control under the threshold of 50 N, which was even after the upgrade from 26 N when the project was initialized. This would open the door for larger bandwidth controllers that could handle the friction loading present in the rig.

Finally, future work should include a revisit of the noise analysis and filter design. The success in this thesis was held back by the relaxation of controller bandwidth, largely due to the phase losses incurred in the filters. While the filters are sorely needed, their

corner frequencies should be pushed further away from the operating window. Also, substitution of the second-order designs for Chebyshev or Butterworth designs could be beneficial.

REFERENCES

[1] D. Hrovat, "Optimal Active Suspension Structures for Quarter-Car Vehicle Models," *Automatica*, vol. 26, no. 5, pp. 845–860, Sep. 1990.

[2] P. Hsu, "Power Recovery Property of Electrical Active Suspension Systems," in *Proc. 31st Intersociety Energy Conversion Engineering Conference*, Aug. 1996, pp. 1899–1904.

[3] M. M. ElMadany, "Design of an Active Suspension for a Heavy Duty Light Truck Using Optimal Control Theory," *Computers and Structures*, vol. 31, no. 3, pp. 385–393, 1989.

[4] A. Guia, M. Melas, C. Seatzu, and G. Usai, "Design of a Predictive Semiactive Suspension System," *Vehicle System Dynamics*, vol. 41, no. 4, pp. 277–300, 2004.

[5] H. K. Fathy, P. Y. Papalambros, A. G. Ulsoy, and D. Hrovat, "Nested Plant/Controller Optimization with Application to Combined Passive/Active Automotive Suspensions," in *Proc. American Control Conference*, June 2003, pp. 3375–3380.

[6] R. Rajamani, "Adaptive Observers for Active Automotive Suspensions: Theory and Experiment," *IEEE Transactions on Control Systems Technology*, vol. 3, no. 1, pp. 86–93, Mar. 1995.

[7] B.-G. Gu and K. Nam, "A Vector Control Scheme for a PM Linear Synchronous Motor in Extended Region," *IEEE Transactions on Industry Applications*, vol. 39, no. 5, pp. 1280 – 1286, Sep. 2003.

[8] W.-J. Kim and B. Murphy, "Development of a Novel Direct-Drive Tubular Linear Brushless Permanent Magnet Motor," *International Journal of Control, Automation, and Systems*, vol. 2, no. 3, pp. 279 – 288, Sep. 2004.

[9] W.-J. Kim, D. Trumper, and J. Lang, "Modeling and Vector Control of Planar Magnetic Levitator," *IEEE Transactions on Industry Applications*, vol. 34, no. 6, pp. 1254–1262, Nov. 1998.

[10] S. Liu, P. Mercorelli, K. Lehmann, "Robust Control of a Permanent Magnet Linear Motor in the Presence of Large Disturbances," in *Proc. IEEE Conference on Control Applications*, June 2003, pp. 1301–1306.

[11] T.-H. Liu, Y.-C. Lee, and Y.-H. Chang, "Adaptive Controller Design for a Linear Motor Control System," *IEEE Transactions on Aerospace and Electronic Systems*, vol. 40, no. 2, pp. 601–616, Apr. 2004.

[12] K. Ohishi, K. Ohnishi, M. Hotta, and K. Taniguchi, "Linear Adaptive Position Control System of Brushless DC Servo Motor," in *Proc.19th Annual IEEE Power Electronics Specialists Conference*, April 1988, pp. 191–198.

[13] P. Barak and H. Sachs, "On the Optimal Ride Control of a Dynamic Model for an Automotive Vehicle System," in *Proc. 9th IAVSD Symposium*, June 1985, pp. 15–29.

[14] K. M. Malek and J. K. Hedrick, "Decoupled Active Suspension Design For Improved Automotive Ride Quality/Handling Performance," in *Proc. 9th IAVSD Symposium*, June 1985, pp. 383–398.

[15] J. A. Levitt and N. G. Zorka, "The Influence of Tire Damping In Quarter Car Active Suspension Models," *Journal of Dynamic Measurement, Systems, and Control*, vol. 113, no. 1, pp. 134–137, March 1991.

[16] G. D.Buckner, K. T. Schuetze, and J. H. Beno, "Intelligent Feedback Linearization for Active Vehicle Suspension Control," *Journal of Dynamic Systems, Measurement, and Control*, vol. 123, pp. 727–733, Dec. 2001.

[17] S. Oshaku, T.Nakayama, I. Kamimura, and Y. Motozono, "Nonlinear H_∞ Control for Semi-Active Suspension," *JSAE REVIEW*, vol. 20, no. 4, pp. 447–452, Oct. 1999.

[18] M. Gobbi, F. Levi, and G. Mastinu, "Multi-Objective Robust Design of the Suspension System of Road Vehicles," *Vehicle System Dynamics*, vol. 41, pp. 537–546, 2004.

[19] M. Sunwoo, K.C. Cheok, "Investigation of Adaptive Control Approaches for Vehicle Active Suspension Systems," in *Proc. American Control Conference*, 1991, pp. 1542–1547.

[20] B. C. Murphy, "Design and Construction of a Precision Tubular Linear Motor and Controller," M.S. Thesis, Mech. Eng., Texas A&M University, College Station, 2003.

[21] F. P. Incropera, D. P. DeWitt, T. L. Bergman, and A. S. Levine, *Fundamentals of Mass and Heat Transfer*, 7th ed. Hoboken, NJ: Wiley & Sons, Inc., 2007.

[22] W.-J. Kim, "High-Precision Planar Magnetic Levitation," Ph.D. Dissertation, Elec. Eng. and Comp. Sci., MIT, Cambridge, 1997.

[23] G. F. Franklin, J. D. Powell, and A. Emami-Naeini, *Feedback Control of Dynamic Systems*, 4th ed. Upper Saddle River, NJ: Prentice-Hall, 2002.

APPENDIX I

SIMULINK SIMULATION BLOCK DIAGRAM

The block diagram presented is the overall view of one built for simulation. It contains all subsections, labeled as to their function.

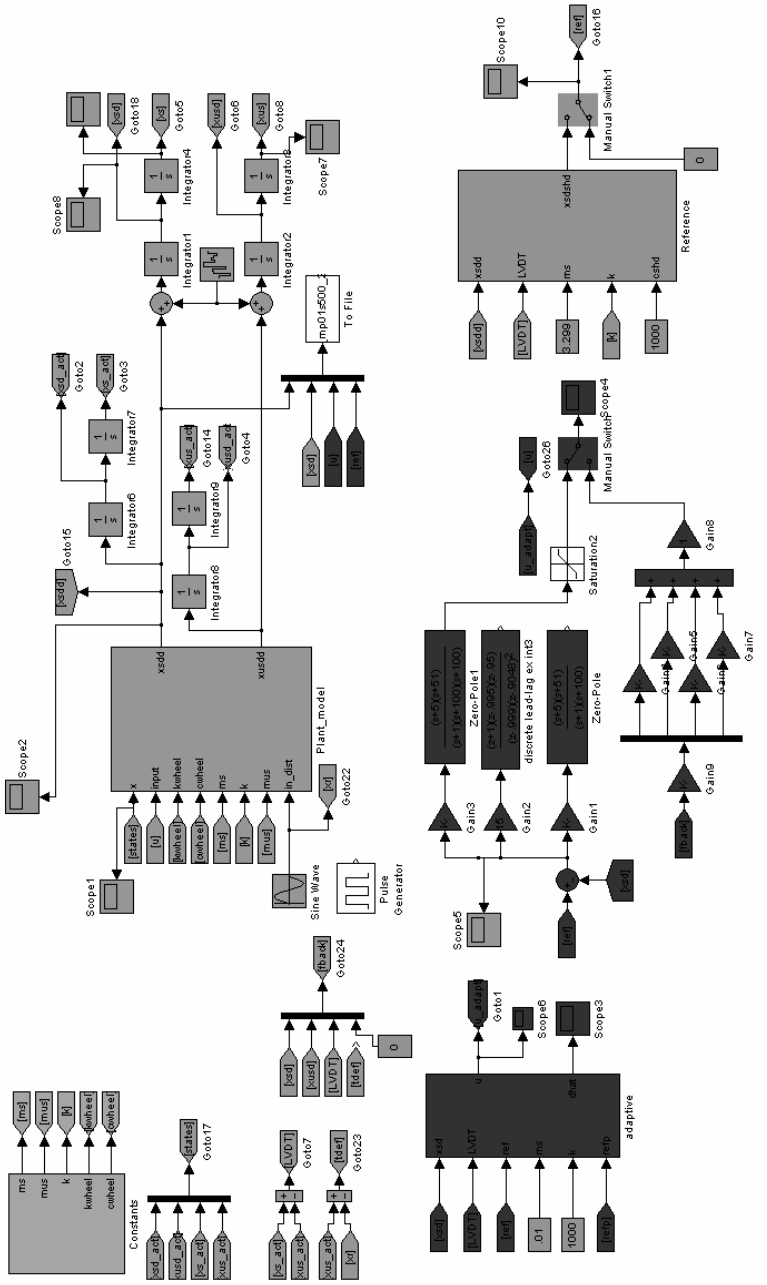

Appendix I.A Contents of ‘Plant_model’ Block, Revealing Simulated Test Rig Diagram

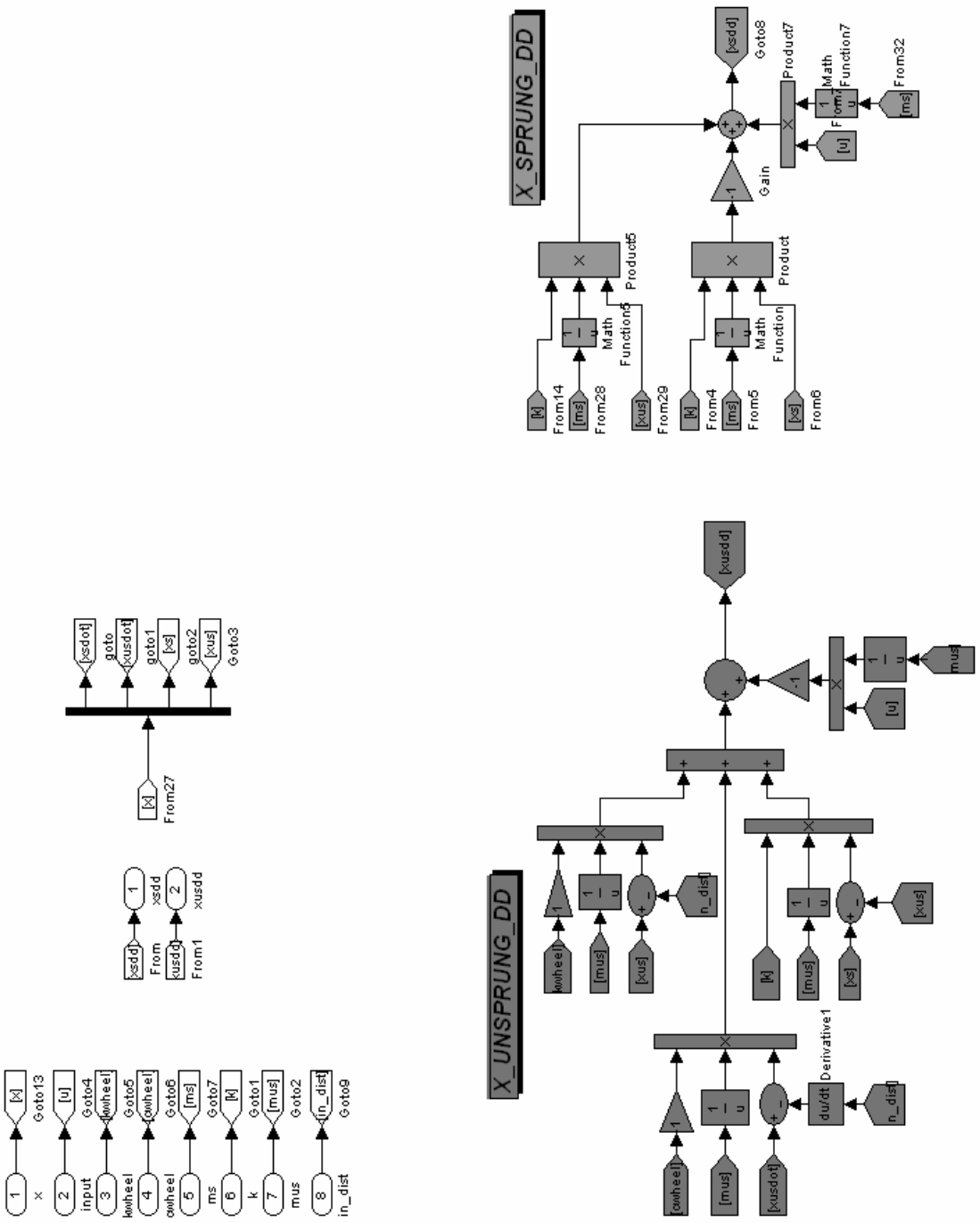

Appendix I.B Close View of Controller Blocks Used In Simulation

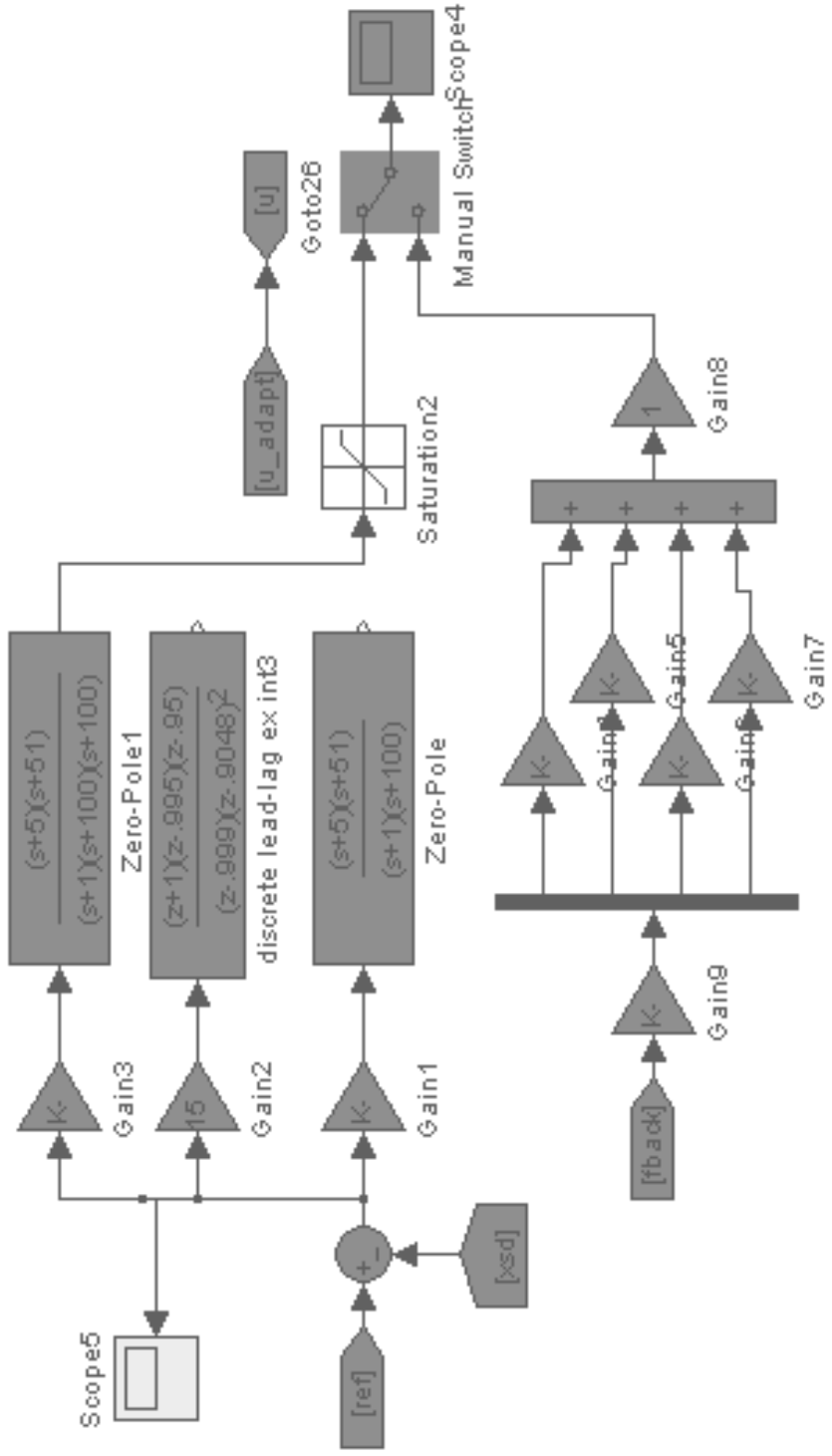

Appendix I.C Contents of ‘Reference’ Block, Revealing Block Diagram for Inertial-frame Damping Reference Generation

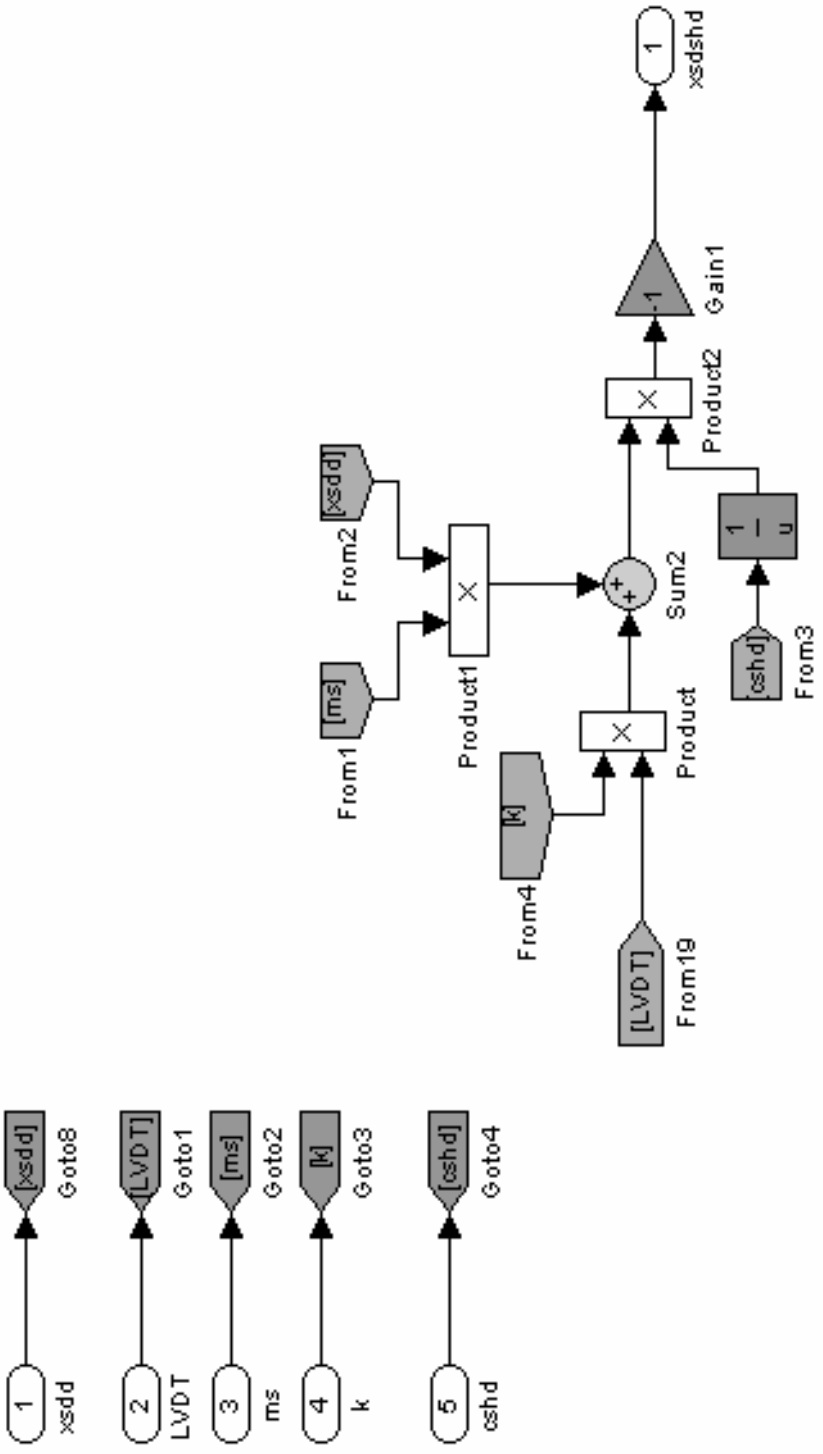

APPENDIX II

SIMULINK BLOCK DIAGRAM FOR DSPACE KERNEL

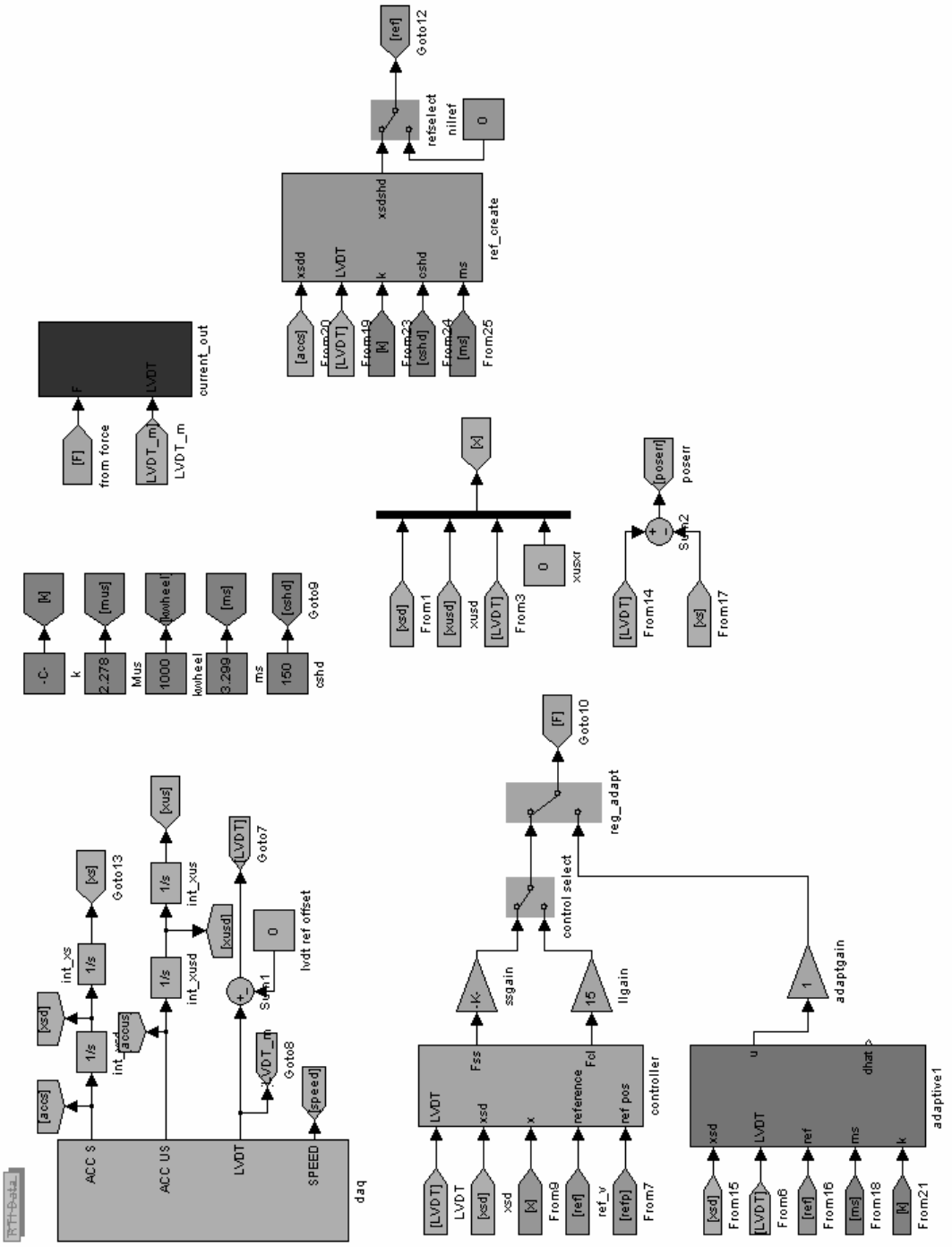

Appendix II.A Contents of ‘daq’ Block, Revealing Block Diagram for Sensor Input and Filtering

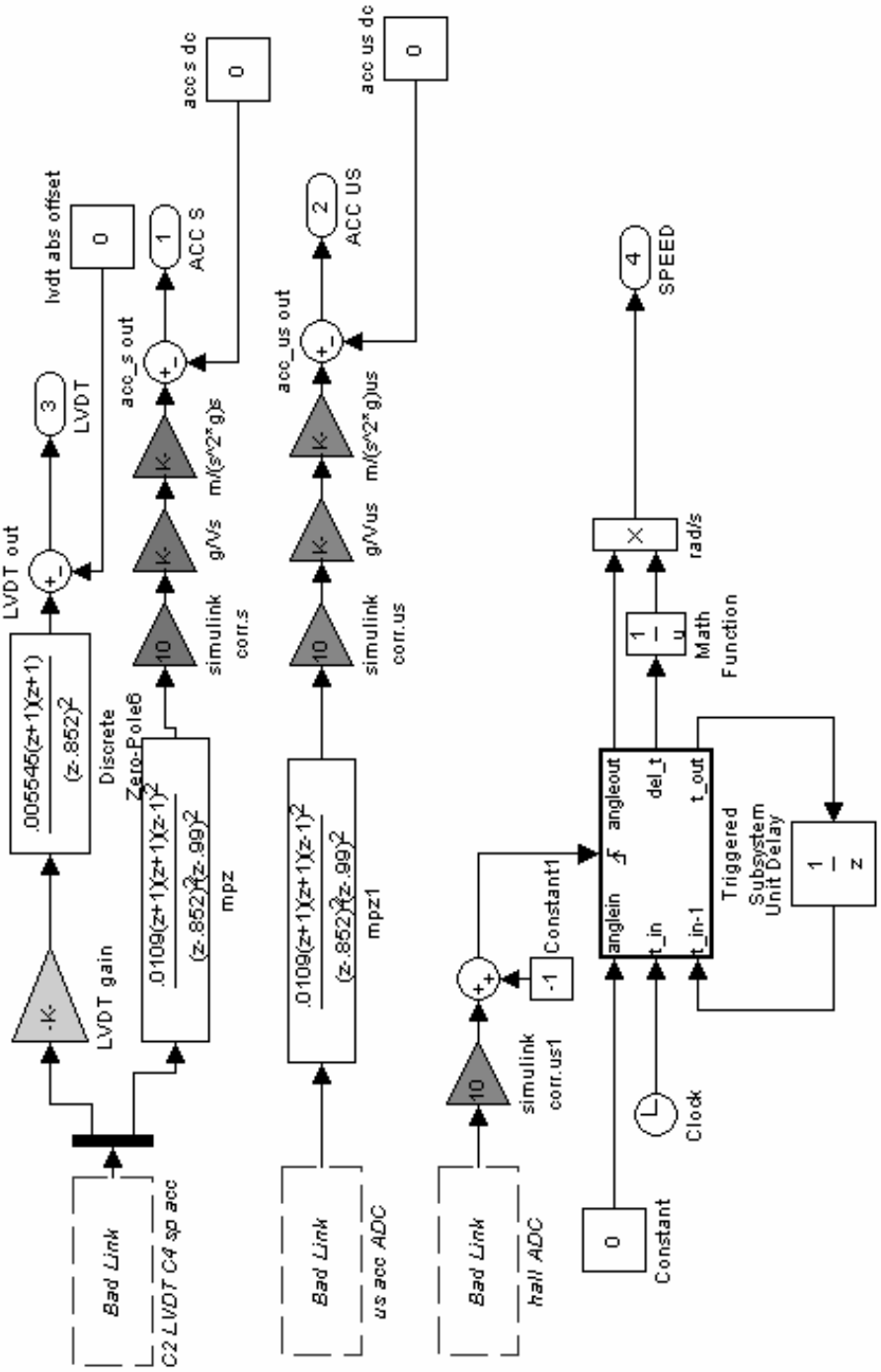

Appendix II.B Contents of ‘controller’ Block, Revealing Block Diagram for Classical and State-Space Controllers

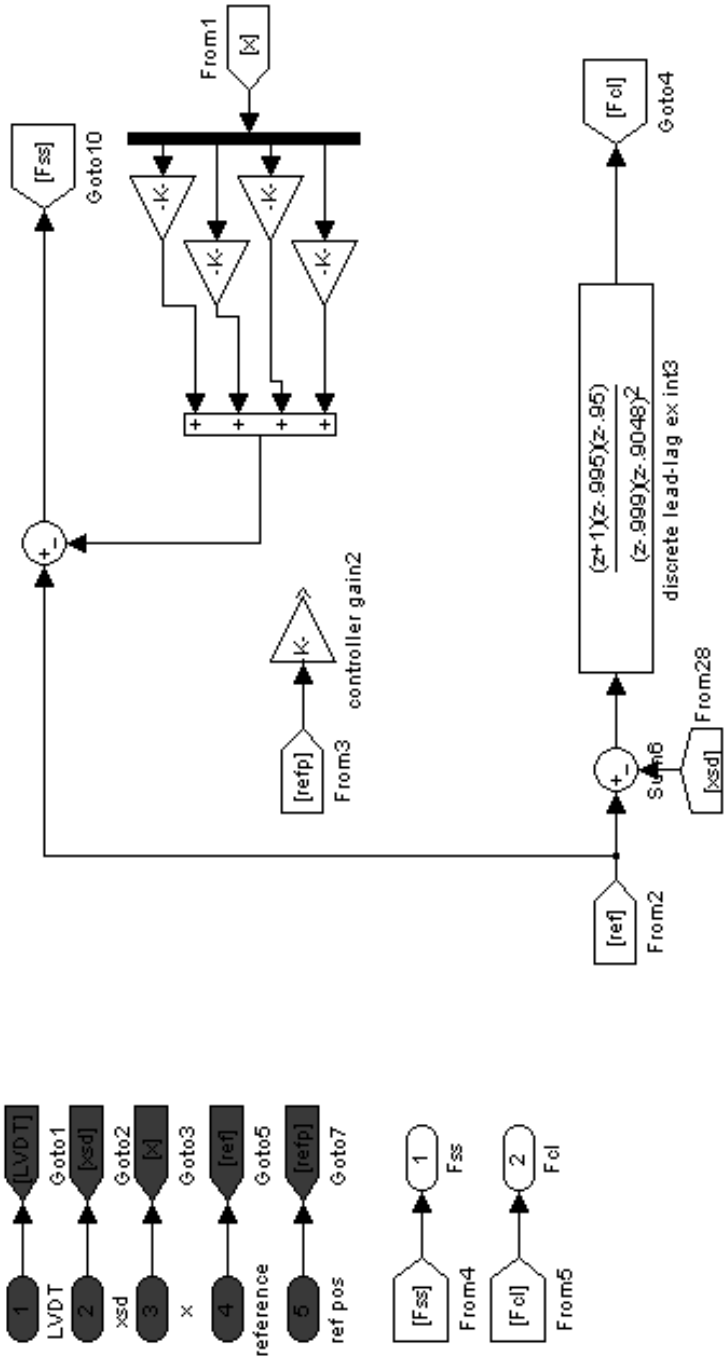

Appendix II.C Contents of ‘ref_create’ Block, Revealing Block Diagram Inertial-frame Damping Reference Generation

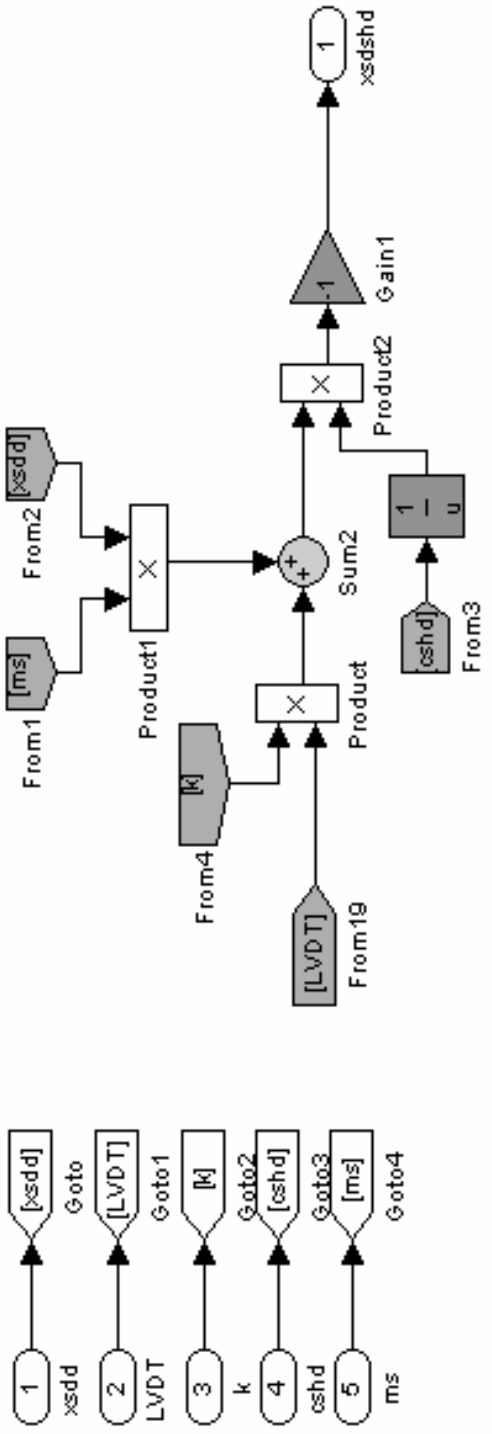

Appendix II.D Contents of ‘current_out’ Block, Revealing Block Diagram for Force-To-Current Conversion and 3-Phase Current Decomposition

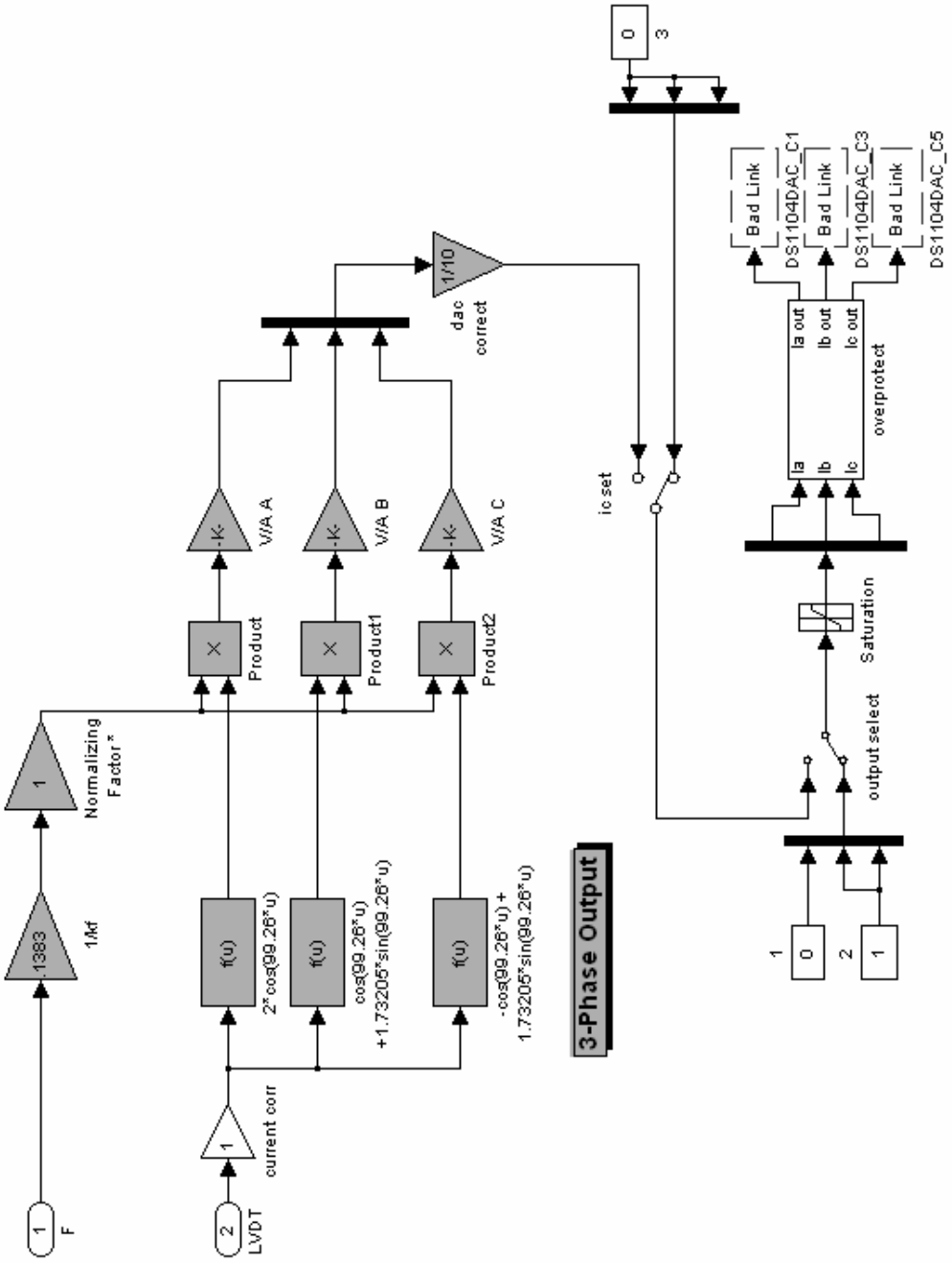

APPENDIX III

CONTROLDESK GUI FOR EXPERIMENTAL CONTROL OF DSPACE KERNEL

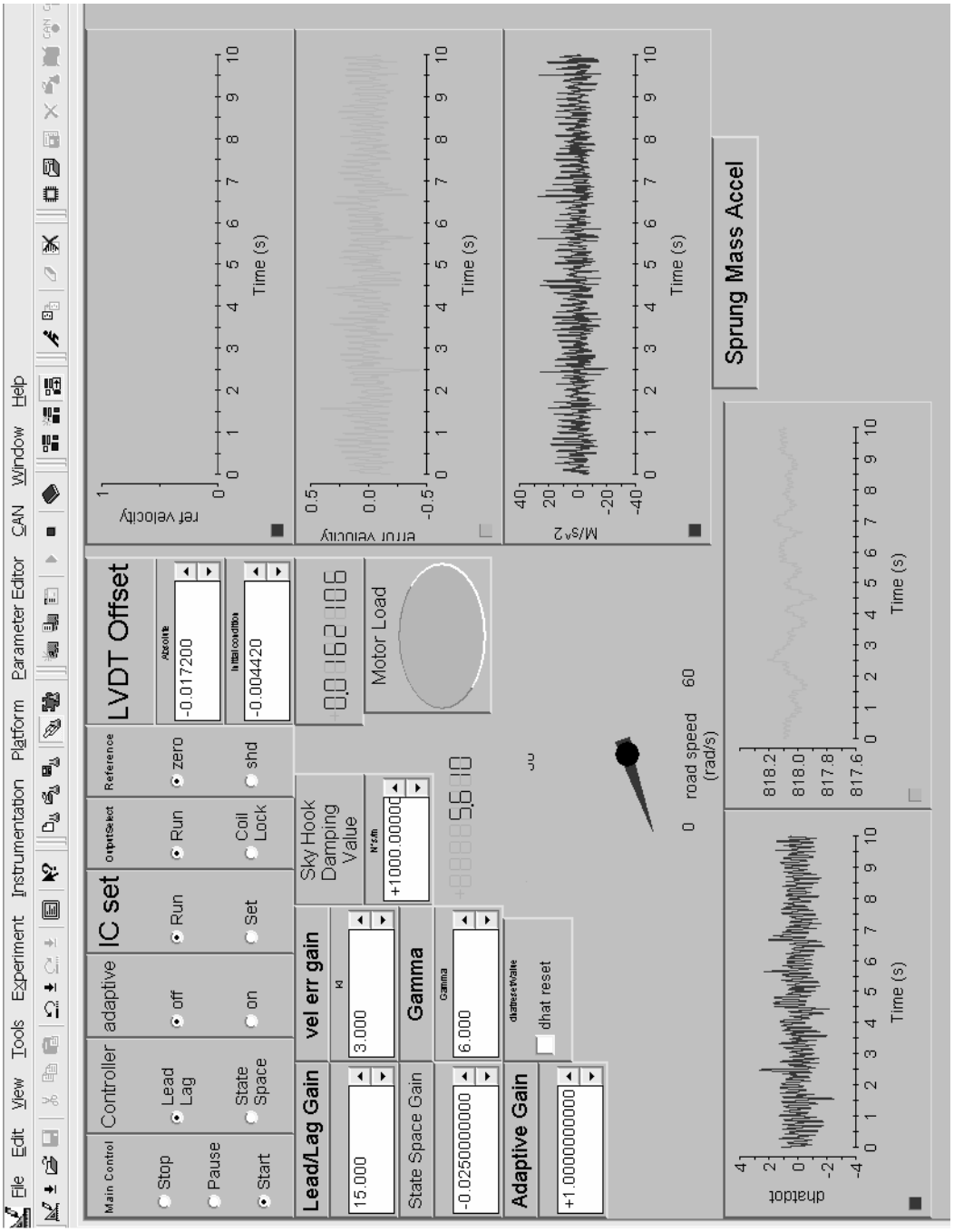

APPENDIX IV

DEVELOPMENT OF FOURIER COEFFICIENTS FOR EXPERIMENTAL ANALYSIS

Fourier transforms are quite useful in presenting time-based periodic signals as a spectrum of represented frequencies. One setback is that the magnitudes in the spectrum from a direct Fourier transform do not represent the same units as they did in the time domain. This appendix focuses on adjusting the Fourier transform output to coincide with the proper time-domain units of interest. All frequency-domain plots presented in Chapter VII were analyzed in the following manner.

Beginning, a periodic function can be represented as an infinite sum of sines and cosines via Fourier Series Expansion. The complex form of this is given in (A-1).

$$F(t) = \sum_{n=-\infty}^{\infty} A_n e^{jn\omega_f t} \tag{A-1}$$

The components of the expansion in (A-1) are the magnitude of the *n*th component coupled with the complex exponential periodic with frequency $n\omega_f$ (the *n*th multiple of the fundamental frequency). The equation for establishing the magnitude A_n is given in (A-2), where the continuous-time function $f(t)$ is defined over period τ.

$$A_n = \frac{1}{\tau}\int_0^{\tau} f(t) e^{-jn\omega_f t} dt \tag{A-2}$$

However useful this relationship is, the data collected is a discrete sampling of a continuous function and thus requires a discrete approximation. The analogue to (A-2) for analyzing sampled data is presented in (A-3)

$$A_k = \frac{1}{M}\sum_{m=0}^{M-1} f_m e^{-2\pi\frac{jm}{M}k} \tag{A-3}$$

The approximation generates A_k, the discrete time equivalent to A_n, through the discretized function f_m of length M. This equation is identical to the FFT equation divided by the sample length.

The next step is to convert the complex Fourier series into its equivalent real-valued series of (A-4).

$$F(t) = \frac{\alpha_0}{2} + \sum_{k=1}^{\frac{M}{2}} B_k \cos(\omega_k t) + C_k \sin(\omega_n t) \tag{A-4}$$

The relationships between complex and real-valued Fourier coefficients are given in (A-5) and (A-6), where the asterisk denotes the complex-conjugate.

$$A_k = B_k + jC_k \tag{A-5}$$

$$A_{-k} = A_k^* \tag{A-6}$$

Using the above relationships and some trigonometric manipulation, the complex Fourier series can now be represented in a real-valued equivalent as a function of magnitude and phase angle, shown in (A-7).

$$F(t) = A_0 + \sum_{k=1}^{\frac{M}{2}} \left|2B_k + 2C_k\right| \cos(\omega_k t - \phi) \tag{A-7}$$

The magnitudes derived from (A-7) are those supporting the discussion of results in Chapter VII.

Appendix IV.A Matlab® Code for Generating Fourier Coefficient Plots

```
clc;
clear;

insheet = xlsread('acc_resp.xls');                    %Gathers data
sample = 1/.001;
insheet(1,2)
[r,c] = size(insheet)

length = 8196;

for i = 1:c
    for j = 1:length
        arr_acc(j,i) = insheet(j+4,i);
        arr_freq(j,i) = insheet(1,i);
    end
end

for i = 1:c
    Y_acc_s(:,i) = fft(arr_acc(:,i),length)/length; %Constructs FFT
arrays
end
for i = 1:c
    Ymag_s(1,i) = abs(Y_acc_s(1,i));
    for j = 2:length
    Ymag_s(j,i) = 2*abs(Y_acc_s(j,i));
    %dB_s(j,i) = 20*log(Ymag_s(j,i));
    end
end



freq = sample/length*(1:1:(length/2))*2*pi;          %Generates
Frequency
[rf,cf] = size(freq)                                  %array

%logfreq = log(freq);
arr_freq_plot = arr_freq(1:105,:);
dB_plot = Ymag_s(1:105,:);%+arr_freq_plot;

freq_plot = freq(:,1:105);

%Plots of FFT analysis for signals

figure(1)
plot3(freq_plot(1,:),arr_freq_plot(:,1),dB_plot(:,1),'linewidth',1.5)
hold
for i =2:c
plot3(freq_plot(1,:),arr_freq_plot(:,i),dB_plot(:,i),'linewidth',1.5)
end
```

```
grid on

xlim([0 80]);
xlabel('Frequency Response (rad/s)')
ylabel('Disturbance Velocity (rad/s)')
zlabel('Magnitude (m/s^2)')
zlim([0 4.5])
hold off


%Plots for time-based representation of signals
time = (0:.001:8);
astart = 1001;
afin = 3000;
ast = 1
aft = 2000
figure(2)
subplot(2,1,1)
plot(time(ast:aft),arr_acc(astart:afin,2))
hold
xlabel('Time (s)')
ylabel('Sprung Mass Acceleration (m/s^2)')
title('15 rad/s Disturbance Response')
grid on
xlim([0 2])
hold off
subplot(2,1,2)
plot(time(ast:aft),arr_acc(astart:afin,4))
hold
xlabel('Time (s)')
ylabel('Sprung Mass Acceleration (m/s^2)')
title('25 rad/s Disturbance Response')
grid on
xlim([0 2])
hold off
```

VITA

Justin Aaron Allen was born in 1981 in Houston, TX. There he lived with his mother, Debbie Bain Allen, and his father, David Lee Allen, until he was ten. Moving to Boerne, TX as the result of his father's career transfer, he lived until another relocation was prompted after graduating from Boerne High School in May of 1999. His desires to further his education landed him at Texas A&M University, where he began coursework in Mechanical Engineering. Upon graduation with a Bachelor of Science in December 2003, he immediately enrolled in the same institution in pursuit of his Master's degree. Currently he is employed with General Electric under the title of Controls Application Development Engineer. He can be reached at the following address:

Justin Allen
GE Energy
300 Garlington Rd
Greenville, SC 29615